Summer November 2014

STUDIES ON THE WRINKLING OF THIN POLYMER FILMS FLOATING ON LIQUID

Kamil B. Toga
University of Massachusetts - Amherst

Recommended Citation

Toga, Kamil B., "STUDIES ON THE WRINKLING OF THIN POLYMER FILMS FLOATING ON LIQUID" (2014). *Doctoral Dissertations*. 201.
https://doi.org/10.7275/4hc2-6h95 https://scholarworks.umass.edu/dissertations_2/201

STUDIES ON THE WRINKLING OF THIN POLYMER FILMS FLOATING ON LIQUID

A Dissertation Presented

by

KAMİL BUĞRA TOGA

Submitted to the Graduate School of the
University of Massachusetts Amherst in partial fulfillment
of the requirements for the degree of

DOCTOR OF PHILOSOPHY

September 2014

Polymer Science and Engineering

STUDIES ON THE WRINKLING OF THIN POLYMER FILMS FLOATING ON LIQUID

A Dissertation Presented

by

KAMİL BUĞRA TOGA

Approved as to style and content by:

____
Thomas P. Russell, Chair

____
Alfred J. Crosby, Member

____
Narayanan Menon, Member

____
David Hoagland, Department Head
Polymer Science and Engineering

To my grandmothers Nermin Burma and Hüsniye Toga,
who shared their limitless love without any expectations.

ACKNOWLEDGMENTS

First, my sincerest thanks go to Professor Thomas P. Russell, who I have been lucky enough to work with for six years. I thank Tom for being patient and supportive throughout my time. He was pushy when needed. It has been a privilege to grow as a researcher with guidance and teachings of an exceptional scientist like Tom. I admire his inspirational appetite for research, unlimited energy at work and limitless support for his students.

I must also extend my thanks to Professor Narayanan Menon, who has played a crucial role in the completion of my PhD. I truly appreciate the time and effort he has spent on me in the course of my scientific education. As I worked on beautiful problems, Menon and his group sincerely shared their opinion and experiences that improved the quality of my research. I truly owe a big Thank you to Menon for considering me no different than his own students.

I also owe a big thanks to Professor Alfred Crosby. Al has been one of the reasons for me to choose this department, not only due to his inspirational research, but also due to his academic career presenting a path model for engineering students pursuing a degree in materials science. Al Crosby’s patience and understanding as a committee member is as much appreciated as his technical help and valuable feedback on my thesis.

I have had the privilege of collaborating with many qualified people during my time here, like Prof. Benny Davidovitch, Dr. Robert Schroll, Prof. Enrique Cerda, the ESPCI soft-matter team that includes Prof. Bico and Prof. Roman; and it is through involvement with them all that I accomplish this work. Thanks are also for the PSE faculty who taught me in the class, and to the technical staff members who kept our instruments running.

I also owe a big thank to the friendly staff we have here in the PSE department. Linda Strzegowski and Sandi Harris Graves arranged my meetings with Tom while always sharing warm smiles and pleasant conversations in the main office. Laurie Banas has made my life easy with all the purchases and reimbursements. The front office staff has worked with me through arriving at PSE, and the completion of my PhD; Lisa Groth (*a.k.a.* the person who is capable of answering all the questions!), Maria Farrington, Greg Dabkowski and Vivien Venskowski, I truly appreciate all you did for me.

I want to personally thank Alix, Mimi (Berengere), Jenn, Andy, Eric, Sam, Nick, Scott, Ruosty, Nonye, David, Sarah, Badel, Toni, Andreas, Stephen, Rory, Keith, (with respect to the chronological order that I met you) and to many other roommates and friends for being there when I needed you to be. Of course, I would be ashamed to forget fellow Turks, who have shared the Amherst experience with me: Semra, Özgül, Sinan, Burcu, İlke, Aslı, Melih, Berra and many others; Herşey için çok sağolun!

Finally I must thank my family and friends in Türkiye who I owe for helping me to become the person I am today. Last but certainly not least I owe my fiancée, Pırıl my sincere gratitude. She has been loving, patient, supportive, and understanding of my PhD mania; and without her, my life would not be as meaningful.

ABSTRACT

STUDIES ON THE WRINKLING OF THIN POLYMER FILMS FLOATING ON LIQUID

SEPTEMBER 2014

KAMİL BUĞRA TOGA, B.S., KOÇ UNIVERSITY

M.S., UNIVERSITY OF MASSACHUSETTS AMHERST

Ph.D., UNIVERSITY OF MASSACHUSETTS AMHERST

Directed by: Professor Thomas P. Russell

This dissertation aims to broaden our understanding on wrinkling instabilities occurring on floating polymeric sheets, and tries to establish innovative methods that exploit these patterns in studies on material behavior and interfacial phenomena. We will address three major topics in this thesis including, *i)* characterization of the conditions required to buckle an annular disc, *ii)* characterization of wrinkles occurring around a droplet/bubble placed on a membrane that is kept taut at the liquid-air interface, and *iii)* using wrinkling patterns as a probe to understand the interfacial behavior and dynamics of ultrathin films.

The first project in this thesis is about a thin floating elastic disc wrinkled by a droplet cast at the center. First, we obtain a three dimensional map of the deformed surface using confocal fluorescent microscopy. Then, we study the identical films in an inverted geometry where an air bubble is in contact with the film from its underside. In this configuration, a high-resolution optical profilometer facilitated the topographical analysis, which provided the detailed elasto-capillary measures of the problem. Finally, we study the patterns as a function of boundary conditions and material properties, where physical properties of the sheet, such as molecular confinement and physical aging, also change the size and wavelength of the pattern.

The wrinkle patterns are also characterized in response to the change in surface tension of the bath liquid with the aid of a Langmuir Trough. This experimental set-up also facilitates the pattern formation on annular elastic discs, when variable peripheral forces create contraction

within the film. Here, planar capillary forces dictate the controlled boundary conditions and probe a regime of deformation where the wrinkle length and the wavelength are empirically related. We should emphasize that the wrinkling of an annulus does not merely mimic the original droplet experiment, also leading to several remarkable discoveries. First, we observe that, in the studied thickness regime (<300nm) wrinkles occur earlier (easier) on thicker films and grow larger. We also realize that the scaled properties of wrinkles (*e.g.* the scaled extent and wavelength of wrinkles) observed for a range of thicknesses can be superimposed on another by displacing the data towards the hypothetical threshold required to wrinkle the zero-thickness sheet. We observe another thickness invariant phenomenon when the conditions of fold formation are found similar for films of identical annular aspect ratios.

Finally, we study the time-dependent change in wrinkles forming on viscoelastic membranes. The dynamic behaviors of wrinkles are related to the rheological characteristics of polymer molecules of linear architecture confined into thicknesses comparable to their melt radius of gyration. In this study, we have found that the normalized size of wrinkles could be a measure of the stress and strain exerted by a droplet. We also have demonstrated that confinement significantly influences the dynamics of PS films. We close this chapter demonstrating that the wrinkling dynamics is related to the kinematics of the film under the droplet, and generally compares to the stress relaxation experiments performed on bulk samples.

TABLE OF CONTENTS

Page

LIST OF TABLES

Table **Page**

LIST OF FIGURES

Figure **Page**

LIST OF SCHEMES

CHAPTER 1

INTRODUCTION

Elastic instabilities have been recognized and studied for ages. In 1757, Swiss mathematician Leonhard Euler derived a formula that gives the maximum axial load a member can carry before buckling. To our knowledge, this is the first formal study on the topic. Yet, the failure of a slender object due to buckling has been a general concern for mankind throughout the history. For example, we can ascertain design considerations in the monuments of the ancient world that aimed to prevent consequences of compression and buckling. Anatolians, Persians, Greeks and Romans (and probably many other civilizations of the antique) have contributed to the design of numerous types of columns that are still used in stone masonry today.

Figure 1. 1: A railway line buckled by the shifting ground in Christchurch, New Zealand (photograph is available online at: www.telegraph.co.uk). Another example of a buckling failure is when railway lines elongate due to thermal expansion and experience compression.

Buckling has become a more critical design concern after classical ages. The invention of blast furnace boosted the mass manufacturing of steel, which has remained as the most widely used structural metal around the globe. The strength of steel has allowed for the design of giant structures like skyscrapers, cross-continental railroads and large vehicles that consist of slender components like beams, columns, sheets and plates. The compromise between the strength, weight and material cost has been the main determinant in design; while, theory of buckling determined the reliability limits of the structures, especially when the components with reduced dimensionality are prone to bending.

A new incentive on buckling research has been fuelled by the growth of film applications. For more than forty years, semiconductor companies have used top-down and bottom-up approaches to reduce the sizes of transistors and integrated circuits in microelectronic devices. Progressive developments in film processing have led to the miniaturization of the devices and created new test beds to observe buckling. Especially during the last decade, buckling has stimulated interest among researchers offering prospects in robust self-organization of small objects via wrinkling[1], folding[2] and crumpling[3, 4]. From then onwards, the research on buckling has not been limited to the manipulation of macroscopic nature, focusing on mesoscopic applications that extend from surface engineering[5-8] to biology[9, 10].

In this thesis, we discuss pattern formation induced by buckling instabilities. We float polymer films of tens of nanometers on a liquid bath and deform the structures by capillary forces. This experimental setting enables us to address questions about a broad range of topics including two-dimensional buckling, mechanics of thin films, polymer physics and interfacial phenomena. Our research is genuinely focused on understanding the behavior of polymer films on the surface of liquids, thus the work presented here, by its nature, is related to applications that extend from packaging to industrial coatings.

1.1 Physics of wrinkling

Two-dimensional structures like thin films often form wrinkles when buckled. Wrinkles as elastic instabilities tend to recur on a surface with a characteristic wavelength and amplitude. Studies [9, 10] have shown that even a small entity like a living cell can wrinkle a soft film at the point of contact where adhesion to the cell wall traces the material. Such delicacy typically calls for mechanical support from an underlying foundation in applications. In a laminate system, when conditions of buckling are met, film deflection is inevitably coupled by the deformation of the foundation. As a result, the equilibrium wavelength and amplitude of the buckled features are a compromise between bending of the film and the flat state preferred by the underlying layer. This is a typical mechanism of wrinkling observed in nature[11], for example, in wrinkling of skin or on the surface of drying fruits. There are numerous other wrinkling mechanisms. In some circumstances, wrinkling is constrained with inextensibility. In other cases, wrinkles do not compose a pure bending state and stretching deformations dominate the instability pattern. In this section, we describe fundamentals of wrinkle formation and a variety of mechanisms that play a role in wrinkle formation.

Instabilities are characterized by the symmetry breaking of some uniform state into patterned structures[12]. To place wrinkling phenomena in a general context, we review the fundamentals of pattern formation driven by instabilities[12]. When a system is taken away from equilibrium, instability patterns are observed beyond a critical threshold. These patterns comprise spatially varying waves that result from competing interactions. A characteristic wavelength of the pattern is decided by a compromise among dominant energy functions and constitutive equations. As an illustration, the formation of waves on large bodies of water can be described; such that, when a mass of water is pulled against gravity, the wavelength is selected by a compromise between gravitational and inertial terms of energy. Just like the waves on an ocean, wrinkles occur on a continuous medium as a result of competing forces acting on a system.

Wrinkling is understood and modeled as an instability-driven pattern formation. In a pioneering wrinkling study[11], a rectangular polyethylene ribbon is uniaxially stretched from a planar state by parallel fixtures. Beyond a critical strain, a wavy pattern parallel to the tensile forces is induced as shown in Fig. 1.2.

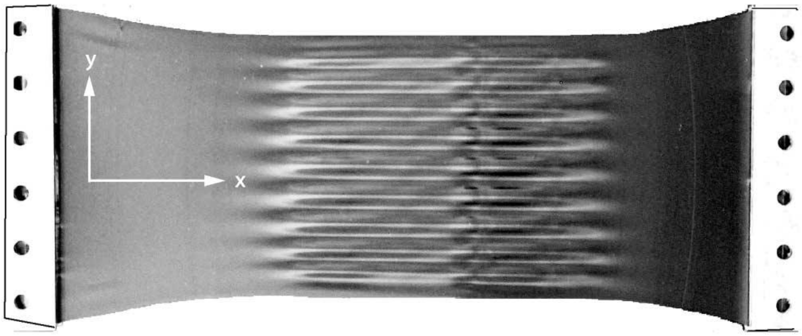

Figure 1. 2: Wrinkles on a polyethylene sheet[11] (length ~25 cm, width *W*~10 cm, and thickness *t*~0.01 cm) under a uniaxial tensile strain of 0.10

The uniaxially stretched ribbon has become a test-bed of a general theory of wrinkling where stretching competed with bending to assign a wavelength, λ and amplitude, ζ to the formed undulations.

$$\lambda \sim \left({}^{B}\!/_{T}\right)^{1/4} \qquad \zeta \sim \lambda\left({}^{\Delta W}\!/_{W}\right)^{1/2} \tag{1.1}$$

The equation (1.1), which is derived from energy arguments and Föppl-von Kármán (FvK) equations, describes the scaling of wrinkling wavelength with the trade-off between the bending modulus of the sheet, B, and the amount of stretching, T, applied on the material. The amplitude of the wrinkles is predicted to scale linearly with λ, where $\Delta W/W$ is the imposed compressive strain on the ribbon.

The theory developed for a freestanding stretched film can be generalized to films wrinkled on elastic foundations. The analogy comes from the similarity between the expression for the stretching energy $U_S \sim \int_A T_x(\partial_x\zeta)^2 \mathrm{d}A$ and the energy associated with the deformation of an elastic foundation $U_F \sim \int_A K\zeta^2 \mathrm{d}A$ (where K is foundation stiffness and A is the area supported). In both scenarios, the balance between the competing energy terms leads to the selection of an intermediate wavelength desired by the pattern.

$$\lambda \sim \left({}^{B}\!/_{K}\right)^{1/4} \tag{1.2}$$

The same approach has also been applied to a floating polystyrene (PS) sheet that is uniaxially compressed by metal blades as presented in Fig. 1.3. In this new setting, the bending energy of the sheet favors long wavelengths (large deflection) whereas the gravitational energy of the liquid bath favors small amplitudes (refined wavelengths). Thus, the wavelength is selected by a compromise between the bending and the gravitational energy ($U_g \sim \rho g\zeta^2$) of the system:

$$\lambda \sim \left({}^{B}/_{\rho g} \right)^{1/4} \tag{1.3}$$

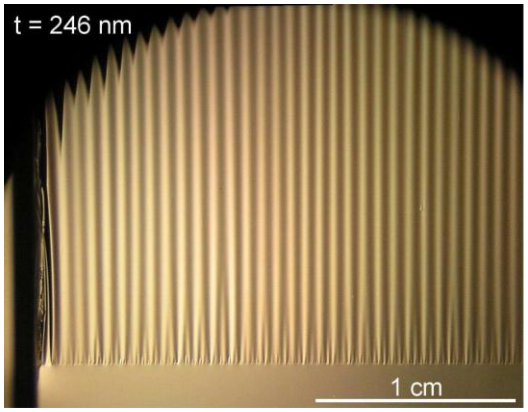

Figure 1. 3: A wrinkled PS sheet[13] floating on the surface of water (density ρ), compressed between two razor blades.

In addition to the formalisms established on understanding the selection of a wavelength by the deformed materials, we can underline two more significant features associated with the elastic instabilities occurring on a 2D structure:

i) Wrinkles occur orthogonal to compression fields: Illustratively, buckling on the polyethylene ribbon was induced by a strong Poisson's effect, where, the imposed contraction can be clearly observed in Fig. 1.2. Similarly, on the PS raft (Fig. 1.3), the uniaxial compression generates parallel waves.

ii) Deformation along wrinkles is bound to the geometrical constraint of inextensibility; which suggests that the lateral contraction is completely converted into the out of plane deformation by bending. A straightforward evaluation of this assumption is possible via a topographical analysis, which has remained as a rather elaborate experimental effort[5].

The inextensibility arguments so far have proved to be a useful criterion to understand the pattern formation by a film deforming under a uniform stress field. For example, the wavenumber of the gravity wrinkles generated on the floating PS sheets were measured in agreement with the inextensibility arguments. The topography of a hard skin coated on a soft substrate[14] can also be tuned according to the same predictions. In this way, elastic instabilities can be exploited as effective tools to decorate and functionalize a broad variety of materials in interesting engineering applications[15]. On the other hand, the properties of wrinkles generated under complex loading conditions are not fully justified by this theory. Likewise, patterns formed under spatially varying stress fields[16, 17] have initiated different puzzles on wrinkling. Among open discussions regarding elastic instabilities, we will focus on wrinkles induced by a tension gradient[18].

1.2 Wrinkles formed in a tension field

As the literature on elastic instabilities has expanded, alternative wrinkling mechanisms have been discovered, such that solvent treatment[19, 20], thermal expansion[21] and irradiation[22] of the laminate structures have generated decorative surfaces. Despite achieving well-controlled and rich morphology of patterns, the conditions leading to buckling have not been precisely quantified in these experiments. Therefore, elastic instabilities induced by indirect stimulants have lacked the simplicity and exactitude to study the fundamentals of buckling and its relation to material properties. To address this issue, we have designed experiments where wrinkles are induced by static mechanical loads, particularly by well-defined capillary forces.

Exploiting the advantages of controllable boundary conditions, we investigate buckling patterns generated on thin polymeric sheets. We also study these patterns from materials point of view by playing with the physical properties of the polymer films.

Mechanically induced wrinkles can be grouped in two categories according to the alignment of the applied load with respect to the formed undulations. Compression induced wrinkles arise in a one dimensional stress field, parallel to applied compression (Fig. 1.3); while, so-called, tension wrinkles (Fig. 1.2) arise orthogonal to the applied forces. Overall, every wrinkle aligns itself perpendicular to compressive stress, and represents the principle stress lines generated. An analogous behavior is observed on a crack tip [23-25], which propagates orthogonal to the tensile stresses built in an isotropic medium. However, in contrast to fracture patterns, wrinkle lines can mark the stress fields in delicate structures without changing or failing the materials. This feature puts wrinkles into a list of useful nondestructive techniques to investigate the mechanics of materials.

An axisymmetric tension gradient provides conditions where wrinkles merely extend within a characteristic finite region. In practice, this is achieved when a circular pre-stretched sheet is loaded by a force at the center. This has so far been an archetypal model to study the information-rich tension wrinkles. Vermorel *et.al.* studied the kinetics of wrinkle formation on a circular rubber patch[26] using a steel ball to apply a force at the center. Chopin *et.al.* reported on wrinkling of plastic foils[27] at the delamination front, where the sheet is adhered onto a smooth glass surface. Holmes and Crosby studied wrinkle-to-fold-transition on floating PS sheets[28] poked at their center. Vella *et.al.* studied the change of topography in the close vicinity of an indented skin[29] pre-stretched by variable hydrostatic pressure. On the whole, none of these studies have closely resembled the 2D schematic depicted in Fig. 1.4 by means of the experiment we propose in this thesis.

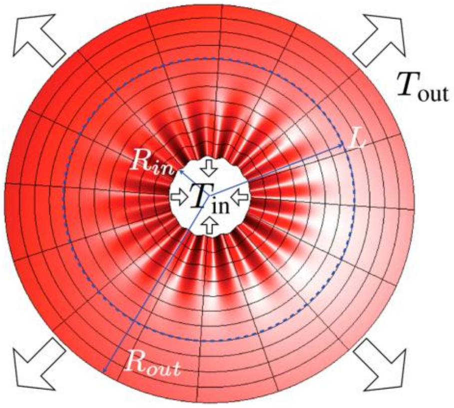

Figure 1. 4: [30] The classical Lamé configuration where a mismatch between the inner and outer stresses produces a compressive region for $r < (L + R_{in})$. T and R denote the applied line tension and radial extent respectively for the inner and the outer boundaries presented.

Research proposed here is based on the static and dynamic behavior of wrinkles generated by a centric load on a floating polymeric disc. For example, the pictures shown in Fig. 1.5 are taken from PS discs[16] exposed to a tension gradient between the capillary forces generated by a water droplet at the center and the surface tension of the subphase acting at the edge of the sheet. From the 2D images, length L and number N of wrinkles can be easily measured as a function of the material properties. Huang *et.al.*[16] successfully characterized the wavelength of these features using inextensibility arguments described earlier in this chapter. The analysis was used as a means to characterize the thickness and the modulus of the membranes studied. The extent of the wrinkled region was just recently understood by additional experiments[31] and calculations[32]. The practical simplicity of the drop on a sheet experiment offers promising prospects in metrology, and new outlooks in interfacial phenomena. Moreover, the statics of the problem contributes to the general understanding on the conditions required to induce buckling in 2D structures. In the following section, we discuss on how the extent of the wrinkled region can mark the stress distribution on a thin disc exposed to a tension gradient.

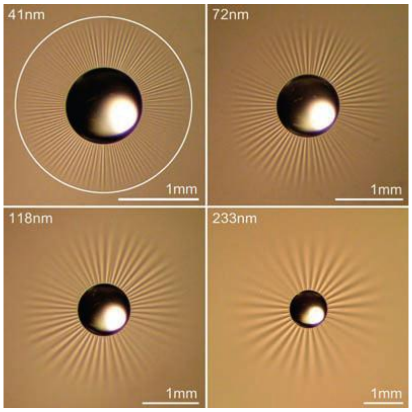

Figure 1. 5: [16] Floating PS discs are wrinkled by water drops of volume ~ 0.2 µL. As the film is made thicker, N decreases and L increases.

1.3 Wrinkle formation and extent

The drop-on-a-sheet experiment has moved along a mature discussion on the mechanical state of the annulus presented in Fig. 1.4. The static equilibrium of the flat structure was first solved by Lamé[33] and thereafter implemented to several wrinkling studies in literature. Géminard *et.al.* studied the wrinkling of annular Latex membranes[34] by manipulating the loading at the boundaries, where amplitude of wrinkles increased with the square root of the force applied at the center ($\zeta \sim T_i^{\ 1/2}$). Cerda studied the same geometry to understand the mechanics of scars[35] suggesting that the size of the draping region around a circular spot inversely scales with the square root of the natural tension in the skin ($L \sim T_o^{-1/2}$). In both studies, the sizes of the wrinkles demonstrate square-root dependences on the magnitude of the loads exerted at the boundaries. These observations have suggested that the extent of wrinkles should match with the radial extent, R_c of the compressive zone generated at the center of the annulus, which, according to Lamé, must also scale with the square root of the boundary forces. The details of Lamé solution can be found in Chapter 4. Here, we merely provide the formula representation:

$$R_c = R_i \sqrt{\frac{T_i}{T_o} - 1} \tag{1.4}$$

Now we can introduce a relevant dimensionless parameter τ, known as load-confinement[30]. This parameter describes the mismatch between the line tensions exerted at the inner and the outer boundaries of the annulus, and provides a measure of the compression in the geometry (see Eq. 1.4).

$$\tau \equiv \frac{T_i}{T_o} \tag{1.5}$$

As τ gets larger than 2, Eq. (1.4) gets a finite value and defines compressive stress in the azimuthal direction. Hence, $\tau = 2$ can be marked as the threshold required to create compression. This trivial analysis has been the basis of post-buckling approach suggesting that the wrinkled extent, R_{wr}, should match with the representation in Eq. (1.4). Nonetheless, it has been demonstrated that this approach is not always valid[17].

The discussion in regards to the conditions wherein a thin object buckles under compression dates back to 18th century when Swiss mathematician Leonhard Euler studied the 1D buckling of columns. According to the energetics of Euler solution[36], if a structure gets slimmer and compliant, the cost of bending ($U_B{\sim}t^3$) becomes smaller in comparison to the cost of stretching ($U_S{\sim}t$). Therefore, sufficiently thin films define an elastic regime in which a broad range of loads buckle the structure prior to the material failure. Hereafter, we call this extreme state as near (buckling) threshold (NT) regime. Briefly, NT wrinkles justify the post buckling approach.

The buckling threshold of a film was further investigated by Davidovitch *et.al.*, who developed a comprehensive model of wrinkling[30] using the annular geometry presented in Fig. 1.4. The theory has proposed a new regime, where wrinkles alter the asymptotic state of the sheet via collapsing the compressive stresses responsible for the formation of wrinkles. Since the stress distribution is altered in this far from threshold (FT) regime, the wrinkle pattern changes. The new extent of wrinkles can be calculated from the minimization of the elastic energy derived from stretching.

$$R_{FFT} = \frac{R_i}{2}\frac{T_i}{T_o} \tag{1.6}$$

In order to distinguish the regimes where NT or FT wrinkles occur, two dimensionless parameters were defined. τ is already described above as a parameter that defines the extent of compressive zone on the model. Bendability, ϵ^{-1}, on the other hand, describes the relative compliance of a film with respect to the magnitude of the applied tension.

$$\epsilon^{-1} \equiv \frac{R_i^2 T_o}{B} \tag{1.7}$$

Together with load-confinement, bendability describes a theoretical phase diagram (Fig. 1.6) that suggests a recipe to generate distinct wrinkling patterns. In this graph, the threshold confinement for buckling has also been shown with a black solid line which decays as a function of increasing bendability (decreasing thickness).

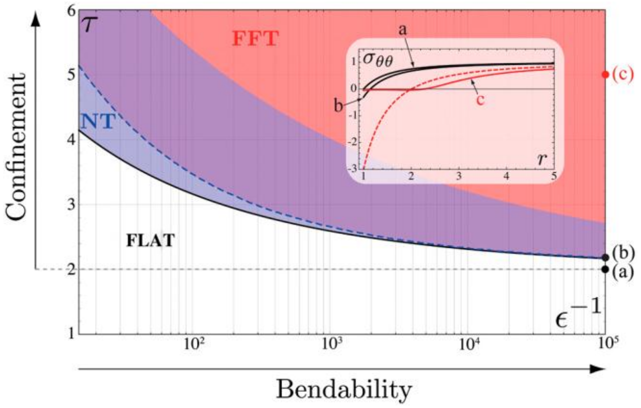

Figure 1. 6: Proposed phase diagram[30] of wrinkling in the Lamé geometry. Radial wrinkles emerge for ϵ, $\tau > \tau_c(\epsilon)$, where the threshold curve $\tau_c(\epsilon)$ computed marked with a black solid line. The NT analysis is valid below the blue dashed line. After a cross-over region (purple), the sheet is under FT conditions (red).

In our experiments, we will test the arguments based on the formation and extent of wrinkles in axisymmetric geometries. We will address and answer some of the questions discussed in the introduction. We will finish this thesis providing new puzzles on wrinkling of thin films.

1.4 Thesis organization

In the next chapter, I start describing the protocol of coating a smooth polymer film on a flat substrate. Then, I explain how a circular disc is etched and floated on water. The chapter follows on a detailed discussion about the practical methods of generating axisymmetric wrinkles on floating polymeric discs. The chapter finishes with a discussion on the characterization techniques used in measuring the thickness and topography of the specimens.

In Chapter 3, I discuss wrinkling of a floating circular film induced by a water droplet or air bubble brought into contact with the film. I carry on the discussion initiated by Hunag *et.al.*[16] via presenting the three-dimensional details of the problem. The experimental results are compared with a new FT theory[32] developed for the drop-on-a-sheet experiment. We also present the details around the contact line using image processing and topographical techniques. Finally, the inception of wrinkles is presented using the results generated with an ultrafast camera.

In Chapter 4, I present the results on wrinkling of an annulus. The discussion starts with image analysis and data reduction, and continues with how the extent and wavelength of wrinkles are measured as a function of capillary forces effective at the boundaries of the annulus. The chapter continues with a discussion on the relevant theoretical models and how these models can be modified for an annulus that comprises a large hole in the middle. At the end of the chapter, I report on a secondary instability observed as fold formation in high-compression regime.

In Chapter 5, I investigate the time-dependent response of wrinkles around a droplet sitting on a viscoelastic film. I compare the pattern dynamics with bulk relaxation and the change in the height of the bulge formed under the droplet. I also study the wrinkle patterns on aged films and films made out of large-molecular-weight polymers.

In Chapter 6, I present the conclusion of this dissertation.

CHAPTER 2

EXPERIMENTAL TECHNIQUES

This chapter describes the details of sample preparation, measurement techniques and apparatus used in this research.

2.1 Spin-Coating

Film coating practices extend from very simple methods, like solvent-casting of wall-paints, to more sophisticated techniques like Langmuir-Blodgett deposition of monolayers onto glass surfaces. Widely preferred methods like powder and spray coating can facilitate application of thick layers of polymers onto a broad variety of objects regardless of the surface properties of the coated material and the coated piece. In contrast, spin-coating[37, 38] is a preferred method for the application of a uniform thin film on a flat surface, where an excess amount of polymer solution is placed on a substrate and the substrate is rotated at a high angular velocity. In this work, sub-micron-thick polymeric coatings are prepared on smooth substrates by a commercially available spin-coater from Specialty Coating Systems Inc. (Model: SCS G3P-8).

One should keep several aspects of spin-coating technique in mind before using spin-coated films in an experiment. Despite offering a practical convenience in preparation of smooth layers with controllable thicknesses, spin-coated films are far removed from equilibrium and may show anomalous thickness changes upon heating [39] and unexpected dewetting properties[40]. Several studies have shown that spin coated surfaces possess a significant amount of residual stress[41], due to the rapid evaporation of the solvent and due to radial orientation of the polymer chains[42-44]. As a consequence, for example, spin-coated block copolymer films require additional treatment to attain a self-assembled morphology[45] dictated by the equilibrium conditions.

In the experiments used in this thesis work, freshly spin-coated glassy films of linear atactic polystyrene (PS) with narrow molecular weight distributions, are wrinkled. The molecular weights of the polymers are well above critical entanglement molecular weight ($M_c \sim 34$ kg/mol[46]) of the linear coil. Prior to the application of the polymer, substrates are cleaned on the spin-coater by rotating an excess amount of acetone at 2000 rpm. Then, an excess amount of polymer solution is placed on a clean microscope slide or silicon wafer, which is rotated at a speed between 1000 and 3000 rpm. As the solvent evaporates, the resultant thickness of the coating is dictated by the concentration of the solution and the rotation speed. The thickness and the quality of the film are also dependent on the vapor pressure of the solvent. In general, we use solutions of PS with number average molecular weight $M_n = 91$ kg/mol, and weight average molecular weight $M_w = 95$ kg/mol (Polymer Source Inc., product ID: P3615-S) dissolved in toluene (Anhydrous 99.8%, Fisher Scientific) with weight concentrations varying between 0.8% to 4.0%. No filtration is applied. We use Premium brand frosted (3 in x 1 in) microscope slides (Fisher Scientific, Catalog number 12-544-1) and bare silicon wafers from International Wafer Service for preparing spin-coated films. Once the substrate is coated, no further processing or annealing is applied. In order to avoid any significant aging effect, the films are used in measurements within the same hour of preparation. (Aging effects will be discussed in Chapter 5.)

2.2 Floating polymeric films

The majority of experiments on thin-film buckling have studied sheets supported on elastic foundations. Handling thin films with a substrate, while industrially preferable, has some disadvantages. The influence of a semi-infinite substrate on the resultant pattern creates conceptual complications. The adhesion between laminate layers may generate non-uniform pinning and domains of localized shear. The out-of-plane deformation of the underlying material is usually over-assumed. A thin film floating on a liquid surface offers an alternative means of studying the related phenomena where the boundary conditions and properties of the liquid are homogenous and can be controlled. A floating elastic disc represents a system under pure in-plane tension. The magnitude of the force applied by the liquid at the perimeter of the film is known and can be controlled. Moreover, the static response of the underlying liquid is simpler than any other soft substance. Consequently, the overall homogeneity provides an ideal geometry in which the wrinkling of thin films can be studied.

Floating an etched disc of polymer on water surface relies on a simple protocol. Circles are drawn on the spin-coated films while the polymer is still adhered to the glass slides. Depending on the dimension of the etched circle we use two different cutting tools and methods. To produce a cut with a diameter larger than ~5 mm, the shape of the specimen is scribed on the substrate with a carbide-tip pencil guided along a template. To cut smaller circles, an aluminum die with a cylindrical bore is placed on to the film surface. A small carbide rod with a sharpened edge on the tip is inserted tightly into the die until the burr delicately touches the film. Rotating the round piece produces a clean circular cut on the surface. The slide is then slowly submerged in a dish of water, where the liquid phase gradually penetrates into the polymer-glass interface slowly removing the cut portion of film from the substrate. Next, if needed, we can transfer the film to another experimental set-up or liquid upon retrieving it with a smooth piece of glass slide or ceramic surface. This method has proven to be successful in transferring films as thin as 30 nm on to a shallow trough filled with water.

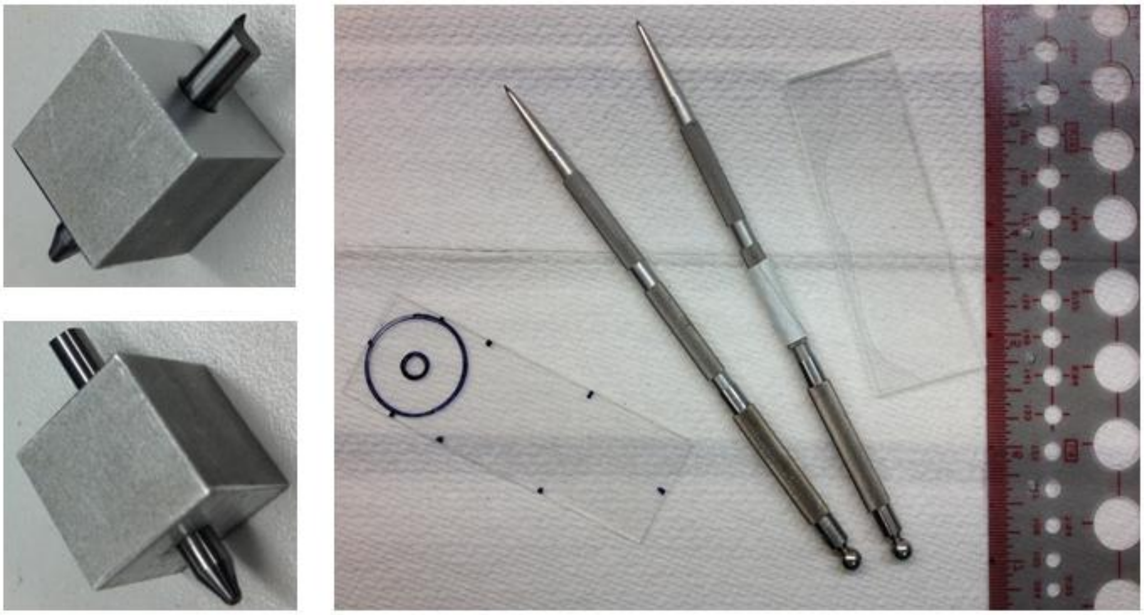

Figure 2. 1: Cutting tools. Left: A carbide bit with a sharp corner inserted in an aluminum die with a cylindrical bore. The diameter of the bit in exhibition is 1.5 mm. Right: A glass slide (1 x 3 in^2) marked with concentric circles is on the left hand side of the larger image. A drawing pattern (at the right hand side of the figure) purchased from a stationery store can be used for drawing concentric circles on the glass. At the center, there are two sharp-tip carbide pencils from Tool Specialty Co. (Fisher catalog number: 13378) generally used for dicing Silicon wafers. In this study, we scribe the films with carbide utensils.

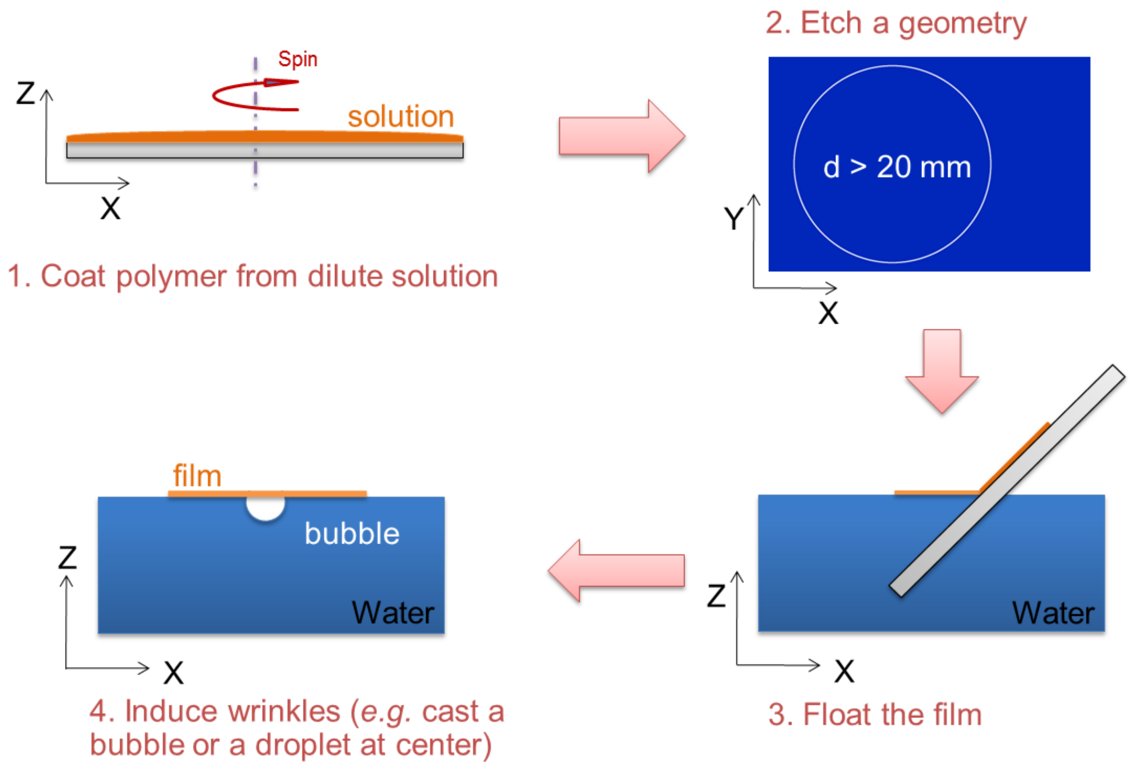

Scheme 2. 2: A schematic of steps taken in preparation and wrinkling of freely floating polymer sheets in Russell and Menon research groups.

The aluminum die is used for preparing annular films. Generating a floating annulus requires a two-step-cutting of concentric circles. Initially, the drawing pattern is placed on the coated surface. Then, the aluminum die is placed symmetrically on top of the flat plastic pattern. In this position, the hard metal does not touch and damage the polymeric coating. The small inner circle is cut first and the die is removed. Second, the outer circle is scribed by the wafer-cutter completing the procedure. In the final step, tailored films are floated onto water and the inner disc is gently removed by tweezers.

The die-cutter has proven to be a reliable tool to float small PS discs[17] with smooth edges. Nevertheless, we have checked the quality of the described procedure by applying an alternative approach on the production, where films are patterned by the carbide pencils both at the inner and the outer perimeter of the concentric circles. Overall, the patterns look similar and the final results have not differed (See Chapter 4). Circularity of the cuts remained almost perfect; Centers of the circles deviated from each other by a relative offset of ~8-24 μm per 1 mm film radius; and the smoothness of the cut has exhibited similar qualities to the eye under microscope magnification.

2.3 Measurement of thickness

Thickness has a crucial role in determining the physical properties of a film[47-49]. As a film gets thinner and constrained to a thickness comparable to characteristic molecular length scales, unusual material behavior can be observed. For instance, glass transition temperature of a polymeric sheet decreases as the material is confined into a thickness comparable to its radius of gyration[50-53]. In addition to the role of confinement, mechanical properties can be directly affected by thickness, such that, the bending modulus of a sheet, *B*, has a strong dependence on thickness[54],

$$B = \frac{Et^3}{12(1-\upsilon^2)} \tag{2.1}$$

where E is the Young's modulus and υ is the Poisson's ratio of the material. According to the equation (2.1), one order of magnitude reduction in the film thickness results in three orders of magnitude decrease in flexural stiffness. Consequently, accurate measurement of thickness is a vital concern in wrinkling studies.

We measured thickness of films adhered to substrates using several optical and topographical techniques, such as interferometry, x-ray reflectivity (XRR), optical profilometry (OP) and atomic force microscopy (AFM). Among these techniques XRR and AFM are absolute measures of film thickness, whereas interferometry and OP rely on reflectance analysis and mathematical modeling of the reflected light, and more importantly, these optical methods assume that the film is isotropic.

XRR and AFM are slow methods requiring instrumental calibration, extensive alignment of the sample and long scan intervals. OP and interferometry are rapid methods, requiring minimal practical effort while capable of retrieving a single scan in several seconds.

The amount of area scanned per a single run also differs for each technique. Interferometer measures reflectance from a ~1 mm wide spot of a light beam. The field of view scanned by the OP (Zygo NewView™ 7300) with a 10x objective is limited to a 1.0 x 1.5 mm^2 rectangular window. A single AFM (Veeco Metrology Group, Dimension 3100) scan is limited to a 200 μm x 200 μm square. Height of the XRR beam projected at the angle of incidence is about 22 mm and width of the beam coming out of a $1/32^o$ divergence slit is 9 mm.

Topographical techniques like AFM and OP can be used to measure the thickness by scratching the sample and measuring the step height. A typical sample preparation protocol (such as the one shown in Fig. 2.2) leaves behind a questionably smooth polymeric layer suitable for a step-height thickness measurement. The corresponding micrographs are presented in Fig. 2.3.

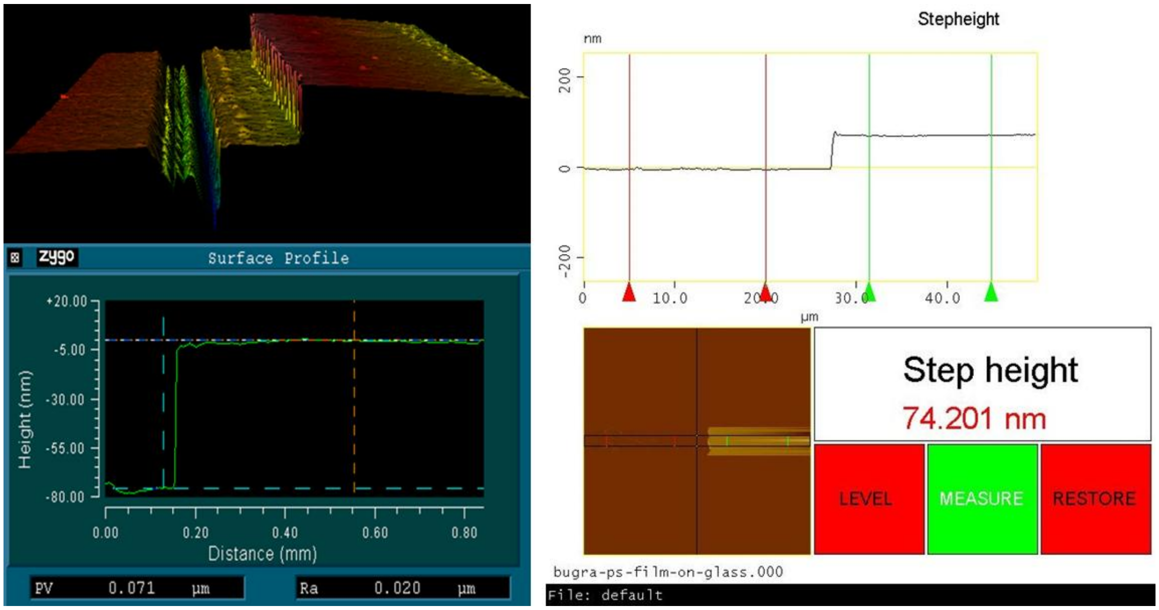

PV 0.071 µm

Ra 0.020 µm

Step height 74.201 nm

bugra-ps-film-on-glass.000

File: default

Figure 2. 3: Step-height measurements performed by OP (left hand side) and AFM (right hand side) on a ~75 nm thick PS film coated on a glass slide. Local thickness values are generated from distinct profile analyses executed by device software. One gets a rough estimate of thickness at the edge of a scribed film, where plastic deformation and creases may affect the retrieved results.

Due to reliability, repeatability and practical convenience, routine thickness measurements in this study are performed with an interferometer (Filmetrics, F20-UV Thin Film Analyzer). In this set-up, a broad spectrum (200-1100 nm) of radiation is generated by a Hammatsu Inc. light source, transferred through a fiber-optic cable, and reflected perpendicularly from the flat sample surface. The intensity of the light reflected from the interfaces depends on the wavelength of the incident beam, refractive indices of the materials and the film thickness. Reflectance can be either in-phase (added to each other) or out-of-phase (subtracted from each other) or some value in between. To determine the thickness, the measured signal is compared with the spectrum computed from the known optical constants and an estimated value of film thickness. The final result is retrieved by minimizing the difference between the measured and the computed spectrum. The goodness of the fit is also reported by the software. In Fig. 2.4, we show a typical report window generated by the software. Please note that Fig. 2.3 and Fig. 2.4 are generated from specimens fabricated with the same protocol.

In order to get reliable data via interferometry, the substrate beneath the film needs to demonstrate specular reflectivity. For that reason, films should stand on reference materials with well-defined optical properties, such as crystalline silicon. We bring smooth PS films into contact with bare silicon surface in two ways. In the first method, we catch the readily floating specimens with a diced and cleaned Si wafer. After drying the film under $N_{2(g)}$, the thickness is measured with interferometer. In the second method, a film is directly applied on a bare Si substrate, using the same preparation conditions as on the glass substrate. The thickness of the floating specimen is estimated from the measurement performed on Si. This is acceptable as long as the thickness of a spin-coated glassy polymer remain constant due to relaxation on water. If the change in planar dimensions of a floating film is smaller than the resolution of an optical microscope, this assumption holds. In a typical glassy polymer coating, the magnitudes of the fabrication-related residual stress is on the order of 10^7 Pa (σ_0~10 MPa[41-44, 55]), while the in-plane stiffness is much larger than the relaxing forces (E~3 GPa >> σ_0).

Table 2. 1: Thickness of PS films (in nanometers) determined by interferometer. Each data is measured at a different spot on the surface. Standard deviation of the data is a combined measure of the instrumental error and the roughness of the sample.

#1	#2	#3	#4	#5	#6	#7	#8	#9	#10	#11	#12	AVG	S.DEV.
76.2	76.5	76.4	76.0	77.2	76.4	74.9	74.7	74.0	74.5	74.6	74.4	**75.5**	**1.0**

As a result of small strains (~10^{-3}), relaxation upon floating creates negligible change in coated thickness. In fact, we do not observe any change in size of the floating films under optical microscope.

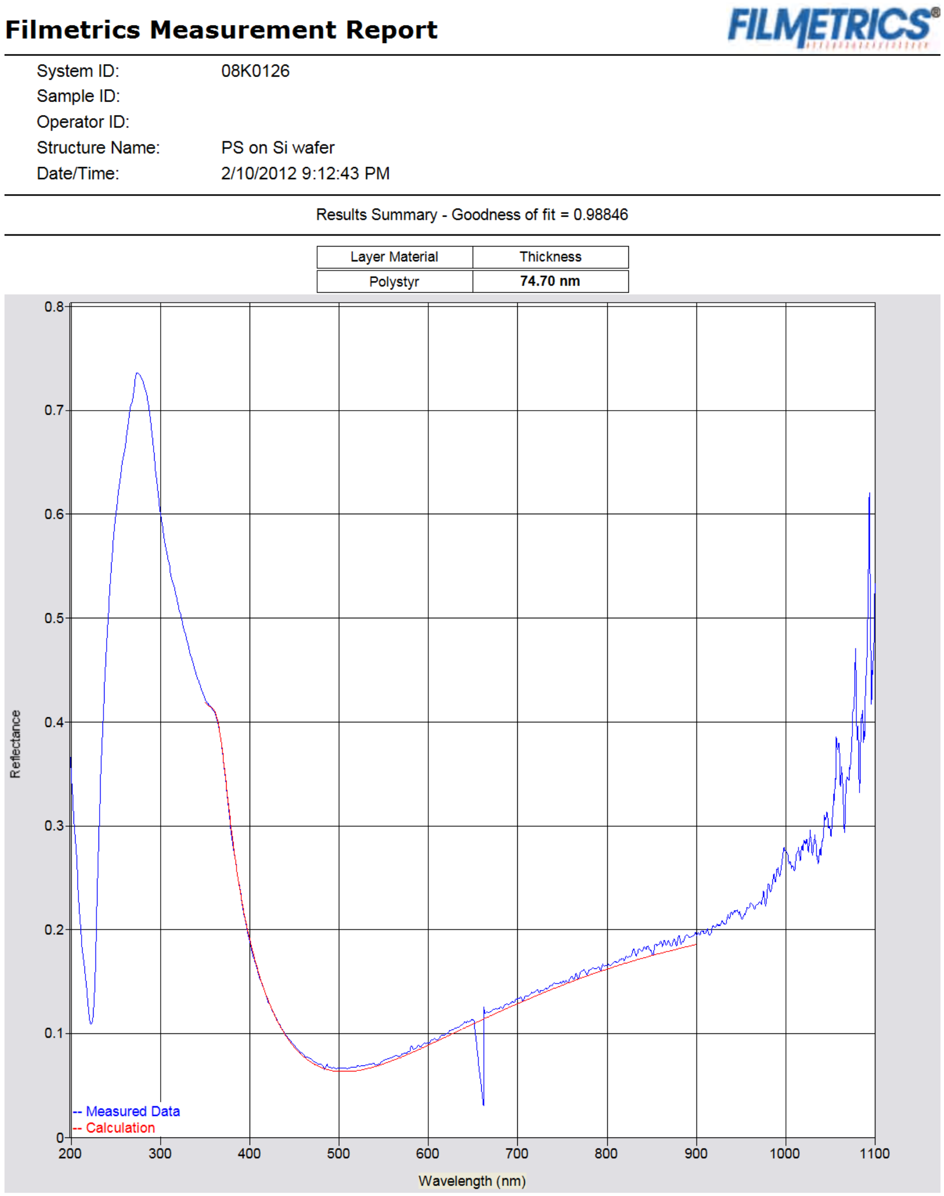

Filmetrics Measurement Report

System ID: 08K0126
Sample ID:
Operator ID:
Structure Name: PS on Si wafer
Date/Time: 2/10/2012 9:12:43 PM

Results Summary - Goodness of fit = 0.98846

Layer Material	Thickness
Polystyr	**74.70 nm**

Figure 2. 4: Reflectance from a 75.5 nm thick PS film coated on a bare Si chip. The blue line is the measured spectrum and the red line is the best fit computed from an estimated thickness value and generic material properties.

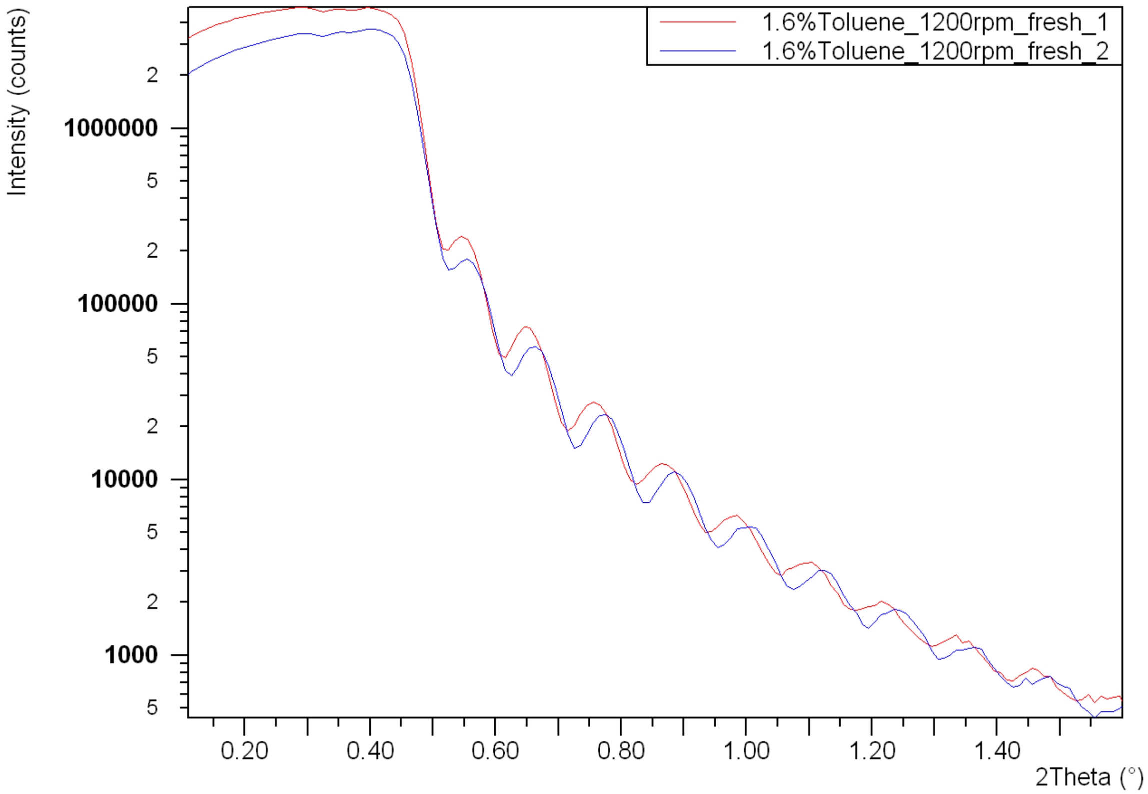

Figure 2. 5: XRR curves for two different PS films coated on glass slides using identical recipes. The thicknesses are determined as 75.9 and 76.2 nm, which is in agreement with the values measured by interferometry *i.e.* <*t*> = 75.5 ± 1.0 nm, from the Table 2.1.

We have validated the interferometry results by performing XRR analyses on identical samples. XRR can be used on any flat substrates and coatings, as long as there is contrast between the electron densities of the film and the substrate. One very attractive feature of XRR is that the refractive index for x-rays is only slightly (one part in 10^4) less than unity. Consequently, the measurements are not sensitive to any orientation in the sample, unlike optical techniques where slight variation in the refractive index due to orientation can measure errors. In a PANalytical X'Pert X-Ray diffractometer set-up, coated glass slides are placed horizontally at the center of a goniometer. Above the critical angle, the incident x-ray beam (wavelength $\lambda_x \sim 0.154$ nm) is reflected from the film surface and polymer-glass interface causing constructive and destructive interferences of the reflected x-rays. This gives rise to Kiessig fringes[56] when plotted against the grazing incident angle of the beam. The period of the fringes is inversely related to the film thickness, $t = 2\pi/\Delta q$, where q is the scattering vector. The scattering vector is defined by $q = (4\pi/\lambda_x)\sin\varphi$ where 2φ is the scattering angle. The thickness values measured with XRR (Fig. 2.5) agree with interferometry analysis performed on the same batch of samples (Table 2.1).

2.4 Wrinkle generation

Before discussing the details of imaging and pattern characterization, we summarize how wrinkles are generated on circular floating sheets. Formation of wrinkles in an axisymmetric tension field has been accomplished by two practical approaches:

1) Droplet on a floating sheet: Tension gradient within the film is created by the out-of-plane forces exerted by a water droplet (or an air bubble) at the center, and the in-plane liquid tension keeping the film taut at the perimeter.

The droplets (and bubbles) are delivered onto the surface using a 10μL-capacity blunt-tip-micro-syringe (Hamilton, Catalog Number: 80383). A drop of controlled volume (0.1-2.0 μL) is released from the syringe, and softly brought in contact with the film. Occasionally, another pendant drop with a measured volume (0.3-0.5 μL) is ejected from the syringe and then added on top of the one already sitting on the film. However, in general, a new droplet is deposited in order to study the effect of the droplet size on the wrinkle pattern.

2) Wrinkling of an annular floating sheet: Tension gradient is created by planar line tension exerted at the boundaries by differentiable surface energy of water. The details of this technique will be discussed in the following section.

2.4.1 Langmuir Trough

Annular floating discs are wrinkled by depressing the liquid tension outside the film while keeping the inner boundary unaffected. To decrease the liquid tension in a controlled manner, a Langmuir trough (Kibron Inc. MicroTroughXS) is used to control the areal density of an insoluble surfactant monolayer. The trough, as shown in Fig. **2.6**, has an uncompressed rectangular area of 5.9x18.8 mm^2 which is bounded by a Teflon casing and barriers. Prior to each run, components of the trough (base, casing and two barriers) are washed with ethanol, and then with de-ionized water. After mounting the cleaned and dried set-up on a long-working-distance microscope, the trough base (a rectangular piece of glass bounded by stripes of Teflon) is filled with acidic water (~10^{-4} M HCl solutions). The depth of water is kept lower than approximately 1 cm. The annular films can be transferred onto the trough by catching and carrying them with the surface of a clean glass slide. In order to ensure the purity of water, the bath is cleaned for one last time by vacuuming liquid from the surface and simultaneously replenishing acidic water with a squeeze-bottle.

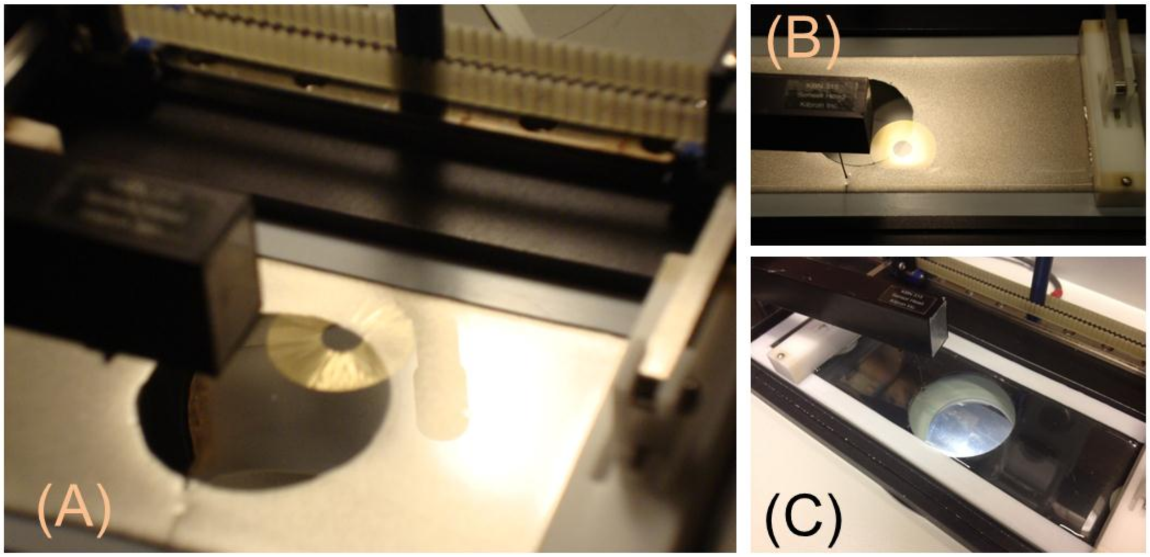

Figure 2. 6: (A) and (B) A PS film wrinkled on a Kibron brand Langmuir trough. The outer diameter of the annular disc is ~2.3 cm. (C) For imaging purposes, a transparent trough base was built using a rectangular piece of glass, Teflon film (to define the boundaries) and adhesive Epoxy resin.

The surface tension is changed by the use of surfactants. The surfactant molecules are located at the surface of water with the polar heads located at the water and the alkyl tails located at the air. By varying the surface area with the movable barriers, the surface coverage can be adjusted. The pressure of the surface active molecules is given by $\Pi = \gamma_{lv,0} - \gamma_{lv}$ where γ_{lv} is the surface tension of the covered surface, and $\gamma_{lv,0}$ is the surface tension of the pure bath substance. The measurement of Π as a function of the areal density of surfactant probes the physical properties and the state of the molecule at the interface. For instance, the compression isotherm of an ordinary molecule demonstrates three characteristic density states which differ in their properties [57]. At low areal density regime, the molecules are randomly dispersed on the surface, like gas molecules. As the surface is compressed, the molecules maintain another disordered state where small changes in the area lead to large changes in the pressure. Further reduction of the area causes the molecules to pack densely on the surface and form a crystalline-like monolayer. Perfluorododecanoic acid surfactant exhibits a typical compression isotherm as demonstrated in Fig. 2.7.

Quantitative measurements on the surface pressure were made using a Wilhelmy plate. In this apparatus, the surface tension exerts a force on a metal rod that is partially immersed in the liquid. The force is generally measured by connecting the rod by a fine wire to an analytical balance, and the displacement translates into a weight or a force. In our studies, a small diameter (0.51 mm) platinum rod is used for this purpose. The downward force exerted onto the metal results from the product of the liquid tension and the contact perimeter. The resolution of the measurements is 0.1 mN/m. Before each run, the instrument is calibrated with clean water reference, where $\gamma_{lv,0}$ = 72.8 mN/m. The rate of compression is automated by a controller and implemented by a servo motor. The rate can be programmed between 1 and 200 mm/min. In the experiments, slow compression rates (4-16 mm/min) are implemented to assure quasistatic response of the surfactant. The micrographs are taken upon maintaining a stable desired value of surface tension.

2.4.2 The surfactant

Solutions (3.4 to 6.2 mg/mL) of perfluorododecanoic acid (Oakwood Products Inc. CAS:307-55-1) in chloroform-methanol (4:1 volume ratio) co-solvent were prepared. Droplets of the solution are placed on the surface of the water in the Langmuir trough. The chloroform and methanol evaporate, leaving the surfactant that subsequently spread across the water surface. The spreading is controlled when each drop (~1-2 μL) is allowed to evaporate before the next is poured to a distant spot on the surface. Perfluorododecanoic acid is made of a 12-Carbon fluorinated tail attached to a carboxylic polar head. Polar head provides an affinity to the water surface while fluorinated chain located at the air surface maintains extreme hydrophobicity. During the barrier compression, perfluorododecanoic acid molecules do not migrate or diffuse inside the annulus. This has been tested and verified by measuring the surface tension locally at the center of the annulus. Due to the weak dispersion forces of the fluorinated tail, the monolayer is capable of depressing the surface tension of water to γ_{lv} ~ 9 mN/m before collapsing the form of crystalline monolayer.

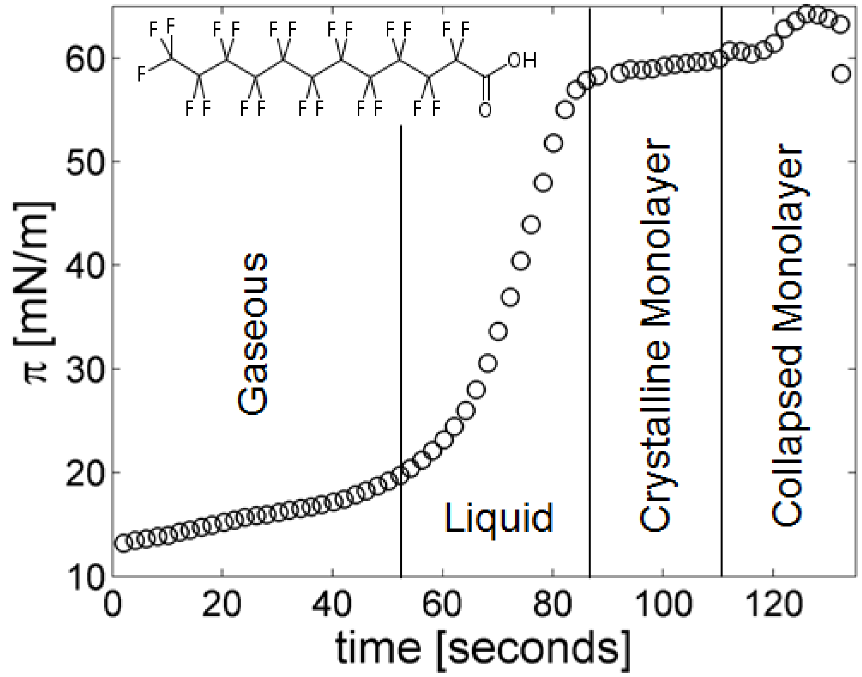

Figure 2. 7: Monomolecular characterization of 9 μL perfluorododecanoic acid dispersed from a 6.2 mg/mL solution on acidic water (pH~3.5). The experiment is performed at 20.5^{o}C with a monotonic compression rate of 80 mm/min. The monolayer can significantly decrease the liquid tension before forming micelles in the subphase.

2.5 Imaging

The wrinkling patterns are observed in transmission using an Olympus Model SZ 40 stereo microscope. This model provides a long working distance and low magnification (less than 4X) which allows the observation of millimetric-sized wrinkle patterns generated on a large area. A microscope base illuminates the samples from beneath, thus the floating film refracts the incident light. The angle of incidence is adjusted by a rotatable mirror, which adjusts and enhances the contrast of undulations. The images are acquired with an Olympus Camedia C-770 Zoom digital camera that is mounted onto one of the eyepieces as shown in Fig. 2.8. Providing low magnification, the microscope does not need a stage micrometer for calibration; instead, a transparent ruler floated on the bath surface sufficiently facilitates as a fine scale. We measured the maximum resolution of the set-up as ~3 μm/pixel.

The wrinkle length, L, is determined both manually by finding the tip of the wrinkle in an image, as well as by an algorithm in which we measure the standard deviation in intensity in concentric circles around the droplet and find the radius at which this quantity drops to the level of the background noise. The wrinkle number N is determined by a manual count, as well as by taking the intensity in a thin annulus centered at r~0.5L, and determining the dominant Fourier component in this profile. This protocol will be further discussed in detail in section 3.7.

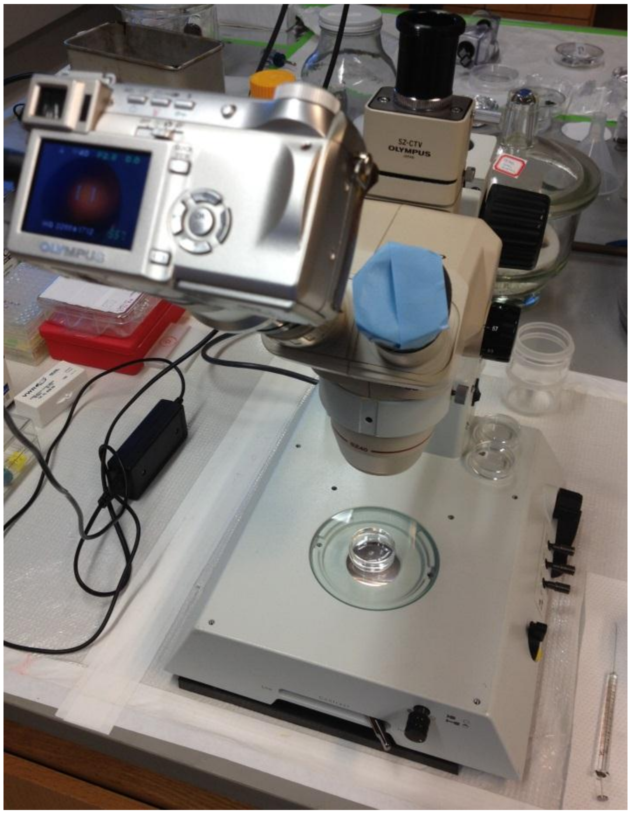

Figure 2. 8: The stereo microscope – digital camera system used for 2D observation of the patterns.

A Leica DCSSP2 fluorescent laser scanning confocal microscope was used to obtain 3D images. For these studies, the PS films were fluorescently labeled with a water-insoluble dye, Nile Red (TCI America, CAS:7385-67-3). Nile Red was dissolved in Toluene with a concentration of ~10 mg/20 mL. Approximately 500 μL of this solution was added into 10−20 mL vials of material that contain 1−3 weight % PS/Toluene solutions. Commercially available acupuncture needles were anchored around the perimeter of the film to trap the fluorescent film and minimize motional blurring during the scan. The field of view of the FCM objective was 1.5 mm x 1.5 mm, and the in-plane lateral resolution was 0.1 mm. Vertical scan steps were made with a resolution of 0.6 μm.

A Zygo Interferometric microscope (Zygo NewView™ 7300) is used to obtain optical profilometry images of the bubble surface. For the greater stability needed here, we used a bath of glycerol rather than water. The field of view is 1.0 mm x 1.5 mm with a 0.1 mm in-plane resolution, and a vertical resolution of 1 nm. The vertical scan was done over a range of 40 mm. Each vertical slice takes 2 seconds to acquire. The volume of the bubble was constant during the scan.

The technique is based on white-light interferometry that is facilitated for high-precision surface structure analysis[58, 59]. The object is scanned by a detector in a direction perpendicular to the object surface. Interferograms are generated for each point that can be resolved with the white light in the field of view. The intensity data is transformed into the spatial frequency domain, and the surface height for each point is obtained with an analysis of the complex phase. Finally, three-dimensional image is constructed from the height data as a function of the planar coordinates

CHAPTER 3

A DROPLET WRINKLING A FLOATING SHEET

In this chapter, we study the wrinkling of circular PS sheets floating on water and glycerol. Wrinkling is induced by water droplets and air bubbles brought in contact with the films at the center.

3.1 Summary

The radial wrinkle pattern generated by a liquid drop on a floating elastic sheet has stimulated a number of advances in the understanding of wrinkle patterns in ultrathin sheets. A puzzle associated with the spatial extent of this simple, highly symmetric pattern has only recently been resolved, but several other basic aspects of the pattern remain unexplained. In this chapter, we report a detailed experimental characterization of the wrinkle pattern generated on elastic PS sheets floating on a fluid, due to the capillary stresses of drops placed on the sheets. The previous study[16] on this simple, symmetric, well characterized setting showed that the traditional post-buckling approach is inadequate to characterize the wrinkle patterns. This stimulated a number of conceptual advances[30, 60] in the understanding of elastic instabilities on ultrathin sheets. Our new experimental observations pose some fresh puzzles and enable a quantitative, calibration-free use of this setup for the metrology of ultrathin films.

The experiment has been first reported by Huang *et.al.* who studied the extent and wavenumber of the pattern via 2-dimensional images[16]. In this thesis, we report a full 3-

dimensional topographical characterization of this problem, and of its counterpart, a bubble beneath a sheet. In addition to measurements of the wrinkle amplitude, these studies reveal the elastic deformation and the resulting wrinkle pattern beneath the drop. We also show that the rather flat boundary condition at the contact line of the drop is achieved by a cascade of wrinkles on both sides of the boundary. We also report studies by high-speed video imaging of the propagation of the wrinkle pattern, with the unexpected result that the wavenumber is established early in the development of the pattern, before it has reached its full spatial extent.

3.2 Background

Placing a droplet of water on an elastic film floating on water generates a wrinkle pattern of finite extent as shown in the image in Fig. 3.1. The film is stretched radially at its outer edge by the air–water surface tension. As the sketch in Fig. 3.1 shows, the droplet applies a Laplace pressure normal to the sheet, and a line tension at the contact line of the drop. If the resultant in-plane radial tension at the contact line is sufficiently larger than the outside tension, then the film is pulled radially toward the contact line and the resultant build-up of material can induce buckling in the azimuthal direction.

This radially symmetric wrinkle pattern can be characterized by the length, L, and number, N, of the wrinkles formed. Huang *et al.*[16] studied the dependence of N and L as a function of the film thickness, t, and the droplet size, a. The number of wrinkles, was successfully described by scaling arguments adapted from Ref: [11] as $N \sim (\gamma_{lv} a^2/\mathrm{B})^{1/4}$, where the bending modulus, $B = Et^3/12(1-\upsilon^2)$, is determined by the thickness t, the Young's modulus E, and the Poisson ratio υ, and γ_{lv} is the air–water surface tension.

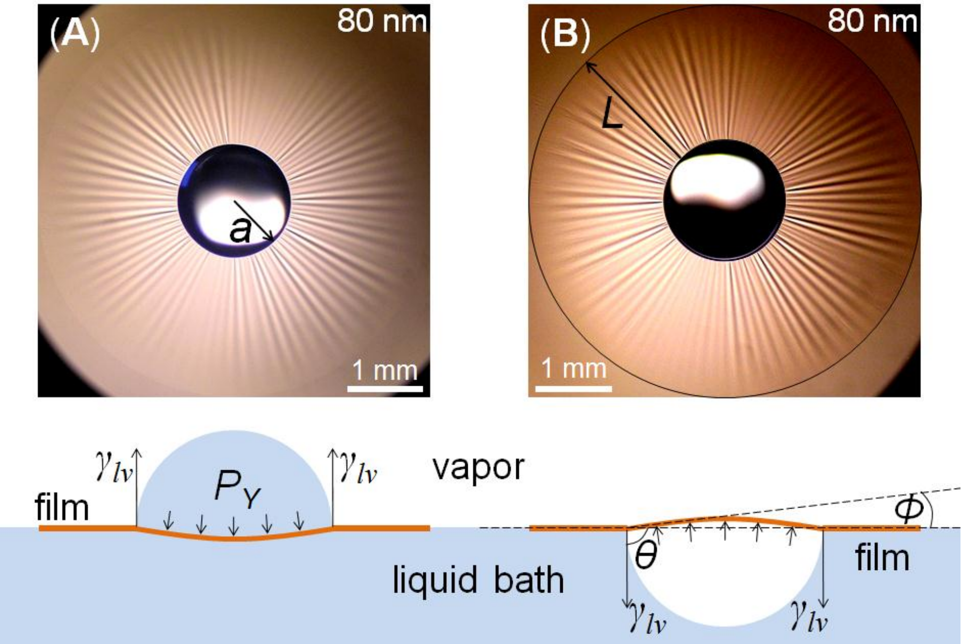

Figure 3. 1: Optical micrographs of (A) a droplet (of radius a = 0.74 mm) and (B) a bubble (a = 0.79 mm) wrinkling a floating sheet of polystyrene (thickness t = 80 nm). The schematic diagrams show the capillary forces at the contact line, and the Laplace pressure P_Y acting on the sheet. We also label the contact angle θ, and the angle ϕ above or below the horizontal due to the deformation of the sheet under the drop or bubble. The diameter of the sheet is 23 mm, much greater than the field of view.

To understand the length of wrinkles, Huang *et al.* employed an analysis for an annulus placed under differential tension. This calculation, attributed to Lamé[33] proceeds by computing the radial and azimuthal stresses σ_{rr} and $\sigma_{\theta\theta}$ in the unbuckled state of the film with the boundary conditions specified by the radial film, respectively. When

$T_i/T_o > 2$, the azimuthal stress becomes compressive within some radius, which is then identified as the extent of the wrinkled zone. The length of the wrinkles is then $L \sim a\, f(\tau)$ when the ratio of the tensions exceeds the threshold value. However, the experiments indicate that the wrinkle length is dependent not only on the radius a, but also the thickness of the sheet, consistent with a scaling of the form $L \sim a\, t^{1/2}$. To recover dimensional consistency, the scaling $L \sim a\, (Et/\gamma_{lv})^{1/2}$ was used and achieved a satisfactory empirical description of the data.

Taken together, these equations for N and L lead to a simple metrology that yields the Young's modulus, E, and the thickness t in terms of the measured quantities. To provide a more solid footing for the scaling for L, Vella *et al.*[60] performed a full postbuckling calculation for the Lamé geometry, including a microscopic calculation for the radial stress at the contact line based on a balance of the stresses in the sheet with the liquid–vapor surface tension at the contact line. This calculation did produce thickness-dependence to L, but which has a different functional form than experimentally observed, and under-predicts the observed length of wrinkles. The failure of this analysis for the size L of the buckled region indicated a fundamental weakness in our understanding of the buckling of ultrathin films.

A fundamentally different issue was raised by Davidovitch *et al.*[30] in their study of an annular region under differential tension. They suggest that for thin enough sheets, the traditional post-buckling, near-threshold (NT) approach is questionable. They introduce a new dimensionless number called the “bendability”, which, in contrast to the purely geometric aspect ratio t/X (where X is the relevant in-plane dimension) also incorporates the mechanical properties of the sheet. When the bendability $\epsilon^{-1} = X^2\gamma_{lv}/B$ is large enough, they point out that the stress state of a sheet even slightly beyond the buckling threshold is profoundly affected by the presence of wrinkles and is not properly described by considering perturbations to the unbuckled state. Rather, they propose that the correct treatment of the wrinkled state involves a perturbation about the so-called membrane limit of a sheet with zero bending-resistance. This calculation framework builds upon the intuitive basis of tension-field theory[61]. Bending rigidity is introduced as a correction to this basic far-from-threshold (FT) picture. The FT framework has also been tested experimentally in a different geometry[17].

Recently, a full FT analysis of the drop-on-sheet geometry has shown reasonable agreement with the measured length, *L*, as a function of the experimental control parameters[32]. However, there is much richness that remains to be explored and understood in this very simple experimental setting. As an obvious matter, the next-order calculation for a small but finite bending modulus that yields the number of wrinkles, *N*, has yet to be done. There is also currently no calculation for the wrinkle profile in this geometry, though a numerical solution[62] has been computed for the annulus geometry which predicts a sharply defined wrinkle tip in the zero-thickness limit, with an additional boundary layer for finite thickness. In order to fully experimentally characterize the wrinkled phase, we present in this article 3-dimensional characterizations of the elastic deformation both outside the contact line and under the drop, both of which were missing in the original experiments of Huang *et.al*. In particular, we present a detailed characterization of the boundary conditions for the wrinkle at the contact line. We find that the flat boundary condition at the contact line of the drop is achieved by a cascade of wrinkle refinement on both sides of the boundary. Finally, the inception and evolution of the wrinkle pattern are studied in the early times following the application of the capillary stresses to the sheet.

3.3 Experimental details

As shown in Fig. 3.1A a wrinkle pattern is generated by first floating a thin polystyrene (PS) sheet on the surface of a fluid, and then placing a drop in the center of the film with a blunt-tip micropipette. The diameter of the sheet is always bigger than the size *L* of the wrinkle pattern, so that the wrinkle pattern is unaffected by edge effects. The drop radii range from a 0.1 to 1 mm. In this range of drop radii, no plastic deformation of the sheet is observed. In Fig. 3.1B we demonstrate an alternative way of creating a wrinkle pattern governed by a balance of the same physical forces. Here, we release an air bubble within the fluid bath under the sheet. The bubble attaches to the sheet and shortly thereafter attains the equilibrium shape shown in the sketch in Fig. 3.1B. We are able to observe the effect of varying bubble radius due to diffusion of the gas through the PS sheet, forced by Laplace pressure. This process is very slow, so that mechanical equilibrium may be assumed at all times. The bubble-under-sheet protocol may be a useful tool in situations where it is not easy to deliver a drop to the top surface, for instance, if the sheet is sandwiched at the interface between two fluids or if the upper fluid is inaccessible. For the purposes of this study, the advantage of the bubble-under-sheet geometry is that it exposes the region in the interior of the contact line to direct visual inspection and bright-field microscopy.

Large-aspect-ratio sheets were prepared from dilute solutions of linear PS (Polymer Source, Atactic, M_n 91k, M_w 95k) in toluene spin coated onto clean microscope slides. In experiments with a gas bubble, we sometimes used higher molecular weight linear PS (Polymer Source, Atactic, M_n 520k, M_w 876k) to suppress gas permeability The thickness of the PS sheets were varied between 30 and 300 nm. Circles of diameter 23 mm were scribed on the PS film. These were floated onto the surface of a pool of deionized water by inserting the scribed edges of the film into the water. The aspect ratio or von Kármán number of the sheet is extremely high, ranging from $a/t = 10^3$ to 10^5. The bendability of the sheet under the applied tension is also extremely large, with ϵ^{-1} ranging from 2 x 10^2 to 3 x 10^6. For the experiments reported here, the fluid in the drop is deionized water. The fluid in the bath is either glycerol or water.

3.4 Wrinkle length and wavenumber in two geometries

We begin by discussing the equivalence between the drop-on-sheet and bubble-under-sheet geometries more quantitatively. As can be seen in Fig. 3.1, in both geometries, the radial tension applied to the free edge of the sheet is γ_{lv}. The sheet also experiences an out-of-plane force at the contact line, again due to the surface tension γ_{lv}. Both bubble and drop apply a uniform Laplace pressure on the sheet. In the case where the fluid is water and sheet is PS, a contact angle of 88–90° is measured[16], with no observable contact angle hysteresis so that the drop or bubble is a hemisphere. In either case, the Laplace pressure is $P_Y = 2\,\gamma_{lv}/a$. However, in our experiments, the drop is small enough that the weight of the drop is much smaller than the capillary force, $P_Y a^2 >> \rho g a^3$. We can thus expect identical external stresses on the sheet.

In Fig. 3.2 we show data for the length, L, and number, N, of the wrinkles obtained in these two geometries. At each value of film thickness, t, data are taken at several values of drop and bubble radius a. As in Ref. [16] we find that L is linearly proportional to a, so we plot the scaled length of the wrinkles, L/a, against the thickness, t, of the sheet. As shown in Fig. 3.2A the data are experimentally indistinguishable in these two geometries. The data for both are consistent with the previous finding of $L/a \sim (Y/\gamma_{lv})^{1/2}$ where the stretching modulus $Y = Et$. The square-root dependence on thickness is indicated by the fit-line. For a given thickness, we find the number of wrinkles, N is proportional to $a^{1/2}$ and therefore in Fig 3.2B we show $N/(a)^{1/2}$ versus thickness t. This choice of ordinate allows us to collapse several values of a in a single data point. The number of wrinkles, N, is also found to be similar in the two geometries. The solid line is fit to a $t^{3/4}$ dependence on thickness, once again consistent with our previous finding that $\mathrm{N} \sim (\gamma_{lv} a^2/B)^{1/4} \sim a^{1/2}\, t^{-3/4}$.

We recall that in the original work[16], Huang *et.al.* followed a scaling argument that produced a correct description of these data for the wrinkle number, while the wrinkle length was a puzzle. The situation has now been reversed, in that a new FT calculation has been shown to be consistent with these data for the size of the wrinkle pattern[32], whereas theory has yet to converge with experiment on the wavenumber of the wrinkle pattern. In what follows, we outline observations that we trust will stimulate a resolution of this new puzzle.

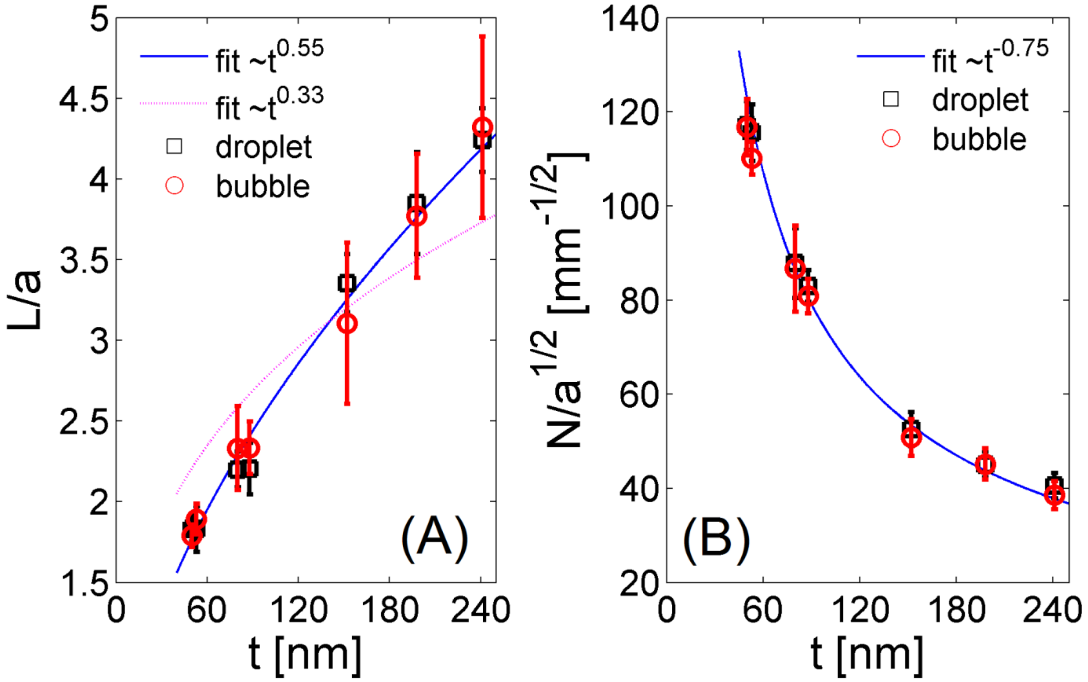

Figure 3. 2: (A) The length L and (B) the number N of wrinkles are scaled by the radius a of the contact line, and plotted against film thickness t. Error bars correspond to the standard deviation of data collected for several values of a. In (A), the blue solid line ($L/a = 0.205\, t^{0.55}$) is a best fit to a power law (as in Ref. [16]), while the dotted line shows the functional form $R_{wr}/a \sim t^{1/3}$ (as in Ref. [32]), where $R_{wr} = L + a$. The number of wrinkles scales with the square root of a and as $B^{-1/4}$ ($N/a^{1/2} = 2310\, t^{-3/4}$).

3.5 Geometry inside the contact line

At its free edge, the sheet is tugged at with a radial line tension γ_o. However, the radial tension σ_{rr} at the contact line is a more complex issue. As sketched in Fig. 3.3B, the sheet deforms into a spherical cap under the drop or bubble. The sheet is then subject to out-of-plane forces near the contact line whose magnitudes are known, but whose directions are affected by the elastic deformation of the sheet. In this section, we determine experimentally the 3D geometry of the sheet near the contact line in order to fully specify the external forces acting on the sheet.

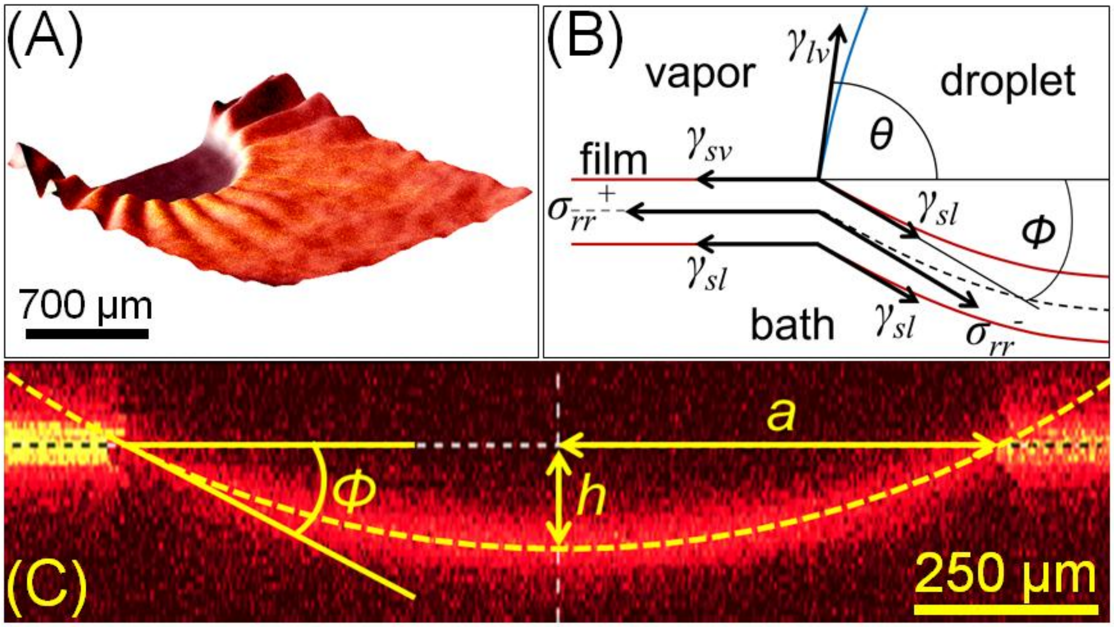

Figure 3. 3: Confocal microscopy was used to characterize the topography of sheets deformed by droplets. (A) A perspective image is shown for a film (t = 209 nm) wrinkled by a droplet with a = 0.5 mm. The scale bar shows the in-plane scale; the out-of-plane axis is exaggerated. (B) Force balance at the contact line. (C) A vertical plane through a diameter demonstrates the bulge under a droplet (a = 0.56 mm, t = 33 nm). The vertical axis is exaggerated and not to scale. The horizontal dashed line represents the bath level. The vertical dashed line goes through the center, where the bulge height, h, is 36.6 mm.

We emphasize that the geometry of the drop near the contact line cannot be inferred from the usual Young–Laplace formula for force balance between the horizontal components of γ_{lv}, γ_{sv}, and γ_{ls} since this approach is predicated on the idea that any resultant vertical force component is balanced by the underlying solid substrate. However, the sheet deforms in response to the vertical component of the force, altering the geometry. This deviation from the Young-Laplace contact angle θ_Y also occurs in a different regime where the substrate is low-modulus and can stretch in response to capillary forces[63-66]. A correct description of the contact angle requires a self-consistent calculation of the radial stress inside and outside the contact line, as well as the capillary forces.

To measure the shape of the sheet under the drop, we labeled the sheet with fluorescent dye and imaged it with confocal microscopy. In Fig. 3.3A, we show the reconstructed image of the deformed sheet. The bulge under the drop is evident. In Fig. 3.3C, we show a single vertical slice through a diameter of the drop. The height of the bulge, h, and the angle ϕ below the horizontal at the contact were measured for a number of sheets of different thickness, and for drops of different radii. Similar measurements of the 3D topography of the bubble geometry were also made (see Chapter 5). Since the bulge was at the upper exposed surface in this case, we were able to study the geometry by white-light interferometry, which is a faster and more precise technique. In Fig. 3.4A we show data for the height of the bulge, h, as a function of drop radius, a, for four different thicknesses. The dependence on a is linear, leading us to show in Fig. 3.4B, h/a against thickness. We show in Fig. 3.4B the angle below the horizontal, ϕ, as a function of thickness. The angle ϕ was not observed to depend upon the drop radius. These two dimensionless descriptors of the bulge-shape both scale with thickness as $t^{-0.38}$. This trend is similar to the predicted behavior[32], $\phi \sim t^{-1/3}$.While we were not able to independently measure the angle θ shown in Fig. 3.3B, our data for the angle ϕ agrees with calculations, as shown in Ref. [32]. They further find that the deviation of the actual contact angle $\theta + \phi$ from the Young–Laplace angle, θ_Y, is given by 2ϕ. With this understanding, it is also possible to compute θ from these data, thus leading to a full determination of all the forces labeled in Fig. 3.3B. The theoretical analysis of the radial force balance that determines the connection between geometry and stress is detailed in Ref. [32]. In the following section, we will briefly discuss the outcomes of this theoretical analysis.

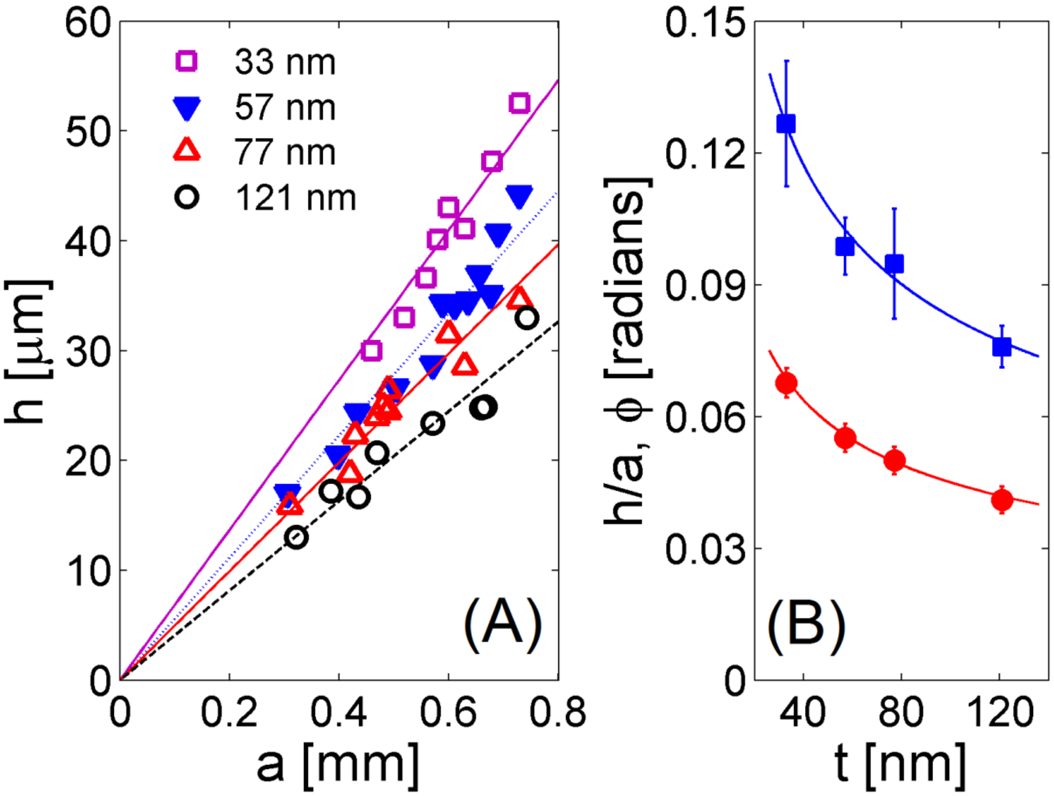

Figure 3. 4: (A) The height *h* of the bulge under the droplet scales linearly with the radius of the contact line, *a*. The bulge height is large in thinner films. (B) Bulge height *h* and the angle ϕ at the contact line decrease with film thickness. The solid lines show best-fit power laws with an exponent 0.38.

3.6 Modeling the problem in FT regime

In this section, we would like to overview the theoretical arguments developed on the drop-on-a-sheet experiment. The framework of ideas presented here were established by a long list of scientists whose names can be found in reference [32]. Theoretical calculations were mostly done by Dr. Robert Schroll and Prof. Benny Davidovitch. The information in the external literature is paraphrased here in order to support some empirical scaling arguments discussed in this thesis.

Schroll *et.al.* in Ref: [32] hypothesized a high bendability regime $\widetilde{\gamma}, \epsilon \ll 1$, ($\widetilde{\gamma} = \gamma_{lv}/Y$) where our films are subject to negligible amount of compression before and after buckling. As a consequence, the elastic stresses in the sheets were determined merely by stretching and exhibited insignificant dependence on the bending modulus. As Fig. 3.3 suggests, the two sides of the contact line are connected through boundary conditions based on continuity of the radial displacements $u(r)$, *i.e.* $u_r^+ = u_r^-$ and the radial force balance:

$$\sigma_{rr}^- \cos\phi + \gamma_{lv} \cos\theta = \sigma_{rr}^+ \tag{3.1}$$

where σ_{rr}^-, u_r^- and σ_{rr}^+, u_r^+ are respectively the radial stresses and displacements at the inner and the outer sides of the contact line, evaluated at $r = a$.

In their solution, Schroll *et.al.* studied the configurations of the films in the inner and the outer regions separately, where both regions resembles previously solved problems. The inner region, modeled as an elastic disc subject to Young-Laplace pressure and a radial tension at its perimeter, mimics the sheet-on-drop problem[17]. The outer region, modeled as an elastic annulus under differential tension, imitates the Lamé problem[30]. The FvK equations generated solutions for the stress field, whose profiles are presented in Fig. 3.5.

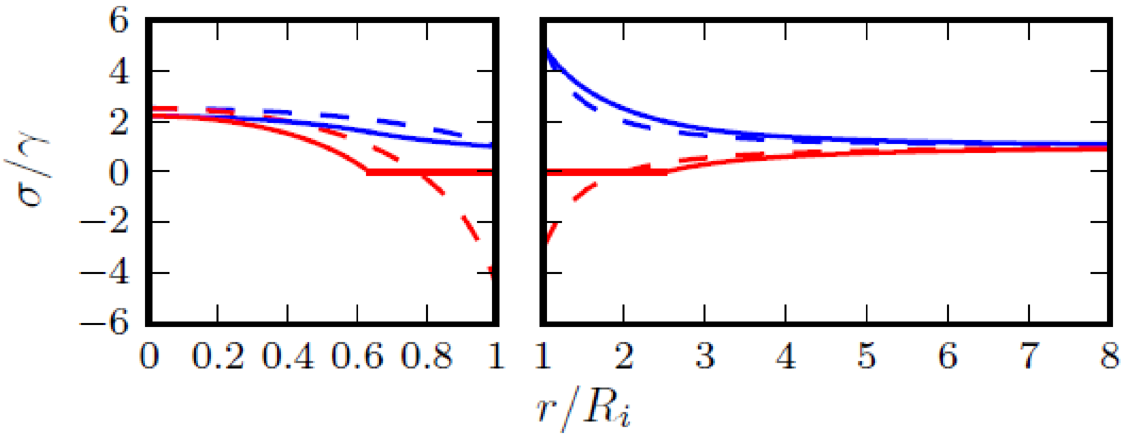

Figure 3. 5: [32] The stresses σ_{rr} (blue), $\sigma_{\theta\theta}$ (red) beneath the drop (left) and outside the contact line (right) for representative post-threshold values of the confinements: $\alpha = 100$, $\tau = 5$. Solid curves are the compression-free (FT) limit. Dashed curves are the axisymmetric (NT) limit. (The graph is copied from Ref: [32])

Two scaling results were found for the studied mechanical regime. When the stretching modulus was greater than the surface tension, Schroll *et.al.* expected the sheet to approach its initial state with $\theta \rightarrow \theta_Y$ and $\phi \rightarrow 0$. Moreover, the radial force balance representation in Eq. (3.1) was further simplified to the following equality, $\sigma_{rr}^{+} \approx \sigma_{rr}^{-}$. The continuity of u_r then provided the relation, $\alpha \sim \log(\tau)$, (where α is the measure of axial contraction under the droplet) allowing Schroll *et.al.* to generate the key scaling argument after assuming $\alpha \sim$ constant:

$$\sigma_{rr}^{-} \propto \sigma_{rr}^{+} \sim \gamma_{lv}^{2/3} Y^{1/3} \tag{3.7}$$

Eq. (3.7) shows that the stress near the center is not altered by the outer tension, merely depending on the mechanics of the sheet beneath the droplet. The scaling law for the extent of wrinkles was also found in the FT regime, $R_{FT} \sim \gamma_{lv}^{2/3} Y^{1/3}/\gamma_o \sim t^{1/3}$. The root-cubical exponent differed from the empirical one proposed in the original reference[16]. Another outcome of Eq. (3.7), which was generated from the vertical force balance at the contact line, was the scaling of the bulge angle, $\phi \sim \widetilde{\gamma}^{-1/3}$. This relationship is measured approximately in Fig. 3.4 of this thesis.

In Fig. 3.6, Schroll *et.al.* compared the theoretical findings with the experimental observations. The wrinkle length detection from experimental images will be described in the following section. Please note that this computational method is merely used in Fig. 3.6 and Fig. 3.11 while the rest of the measurements presented in this thesis are performed by inspection (a more subjective, but more accurate method to extract L from images that will be discussed in the next section).

Fig. 3.6A and 3.6B demonstrated a similar trend between data and prediction. In Fig. 3.6D, Schroll *et.al.* compared the predicted profile of the blister under the droplet to the experimental data that was previously presented in Fig. 3.3C. The curved shape was similar, but the amplitude was overestimated. This numerical deviation is also related to the discrepancy observed in Fig. 3.6C. Overall, this theory has contributed to the literature as an important reference to understand the elasto-capillary effect of a liquid droplet resting on a compliant structure. In Chapter 5, we will also benefit from the scaling laws derived in this reference, as we try to understand the relationship between the bulge height and the extent of wrinkles. Now, we would like to skip to the next section where we will evaluate different approaches on the wrinkle length measurement.

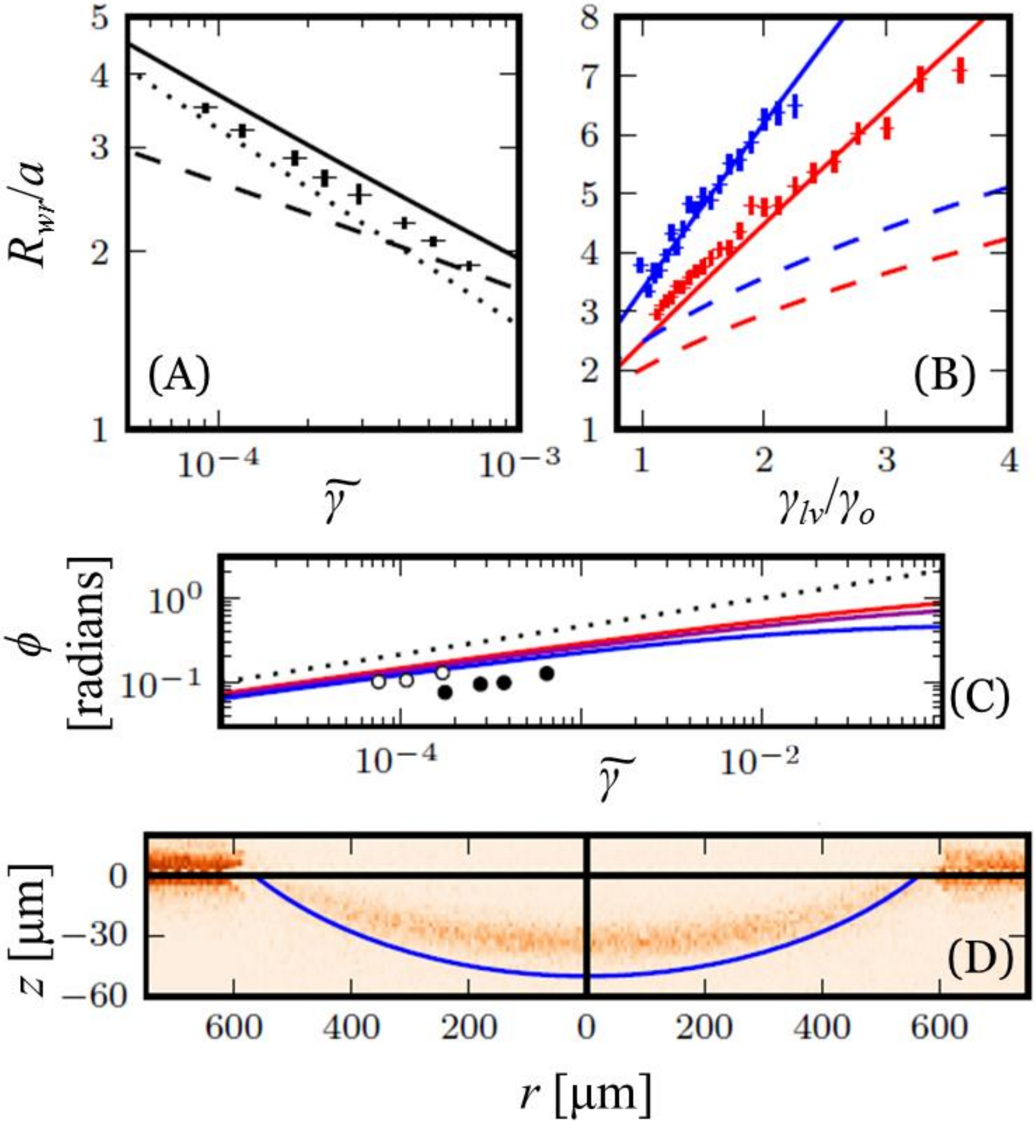

Figure 3. 6: Comparison between observed and predicted parameters (Copied from Ref: [32]). At the top, predictions shown for the FT (solid lines) and NT (dashed lines) theories, and the wrinkle radius (normalized by *a*) plotted against (A) variable $\widetilde{\gamma}$ (data obtained by keeping γ_{lv} and γ_o fixed, and varying *t* from 31 to 233 nm[16]). The dotted line has a slope −1/3. (B) 50 nm (red) and 152 nm (blue), and γ_o is varied using a concentration of surfactant (perfluorododecanoic acid) in the aqueous bath. Vertical error bars result from taking the standard deviation of several wrinkles. The measurement of

the wrinkle length is done by software. (C) A log-log plot of the angle ϕ. Dashed line (guide to the eye) has a slope 1/3. Data points: solid circles are taken from confocal fluorescence microscopy measurement of the sheet's profile under the drop. Both bath and drop are water. The open circles are from a different, but comparable configuration (where bath is glycerol.) (D) The measured profile beneath the drop, obtained by confocal microscopy[31], and the predicted profile (blue curve).

3.7 Analysis of the two-dimensional images

In all graphs presented in this thesis, we determine the wrinkle lengths from bright-field images of the top view of the droplets (Fig. 3.1). We precisely quantify the value of wrinkle length by the inspection method. Since the reliability check of the theoretical results in Ref: [32] depended on a quantitative comparison, we applied a numerical analysis to characterize the length of wrinkles. In the supplemental extras of the original manuscript, Schroll *et.al.* emphasize that '*the numerical value of the measured wrinkle length depends on the choice of parameters used in the analysis'*. Initially, we would like to discuss on the details of this automated technique:

The image is initially converted to a high-contrast 8-bit grayscale image using Image J. The diameter and the center of the droplets are also detected with the same software (with a 99.9% precision). With a Matlab routine, we compute the azimuthal profiles of the intensity $I_r(\vartheta)$ along circles of radius r centered on the droplet. The radial intensity profiles comprise low-frequency variations due to illumination, as wells as higher frequency undulations corresponding to wrinkles. In order to subtract the background noise, we perform a high pass filter to the profiles. We calculate the standard deviation $\delta\,(r)$ in signal and attain a numerical value that can be defined as the optical amplitude of wrinkles at position r. The range r of analysis is varied from 1.1a out to a maximum radius that is unwrinkled. Fig. 3.7 shows δ graphed against r/a for several wrinkle patterns formed on 94 nm membranes.

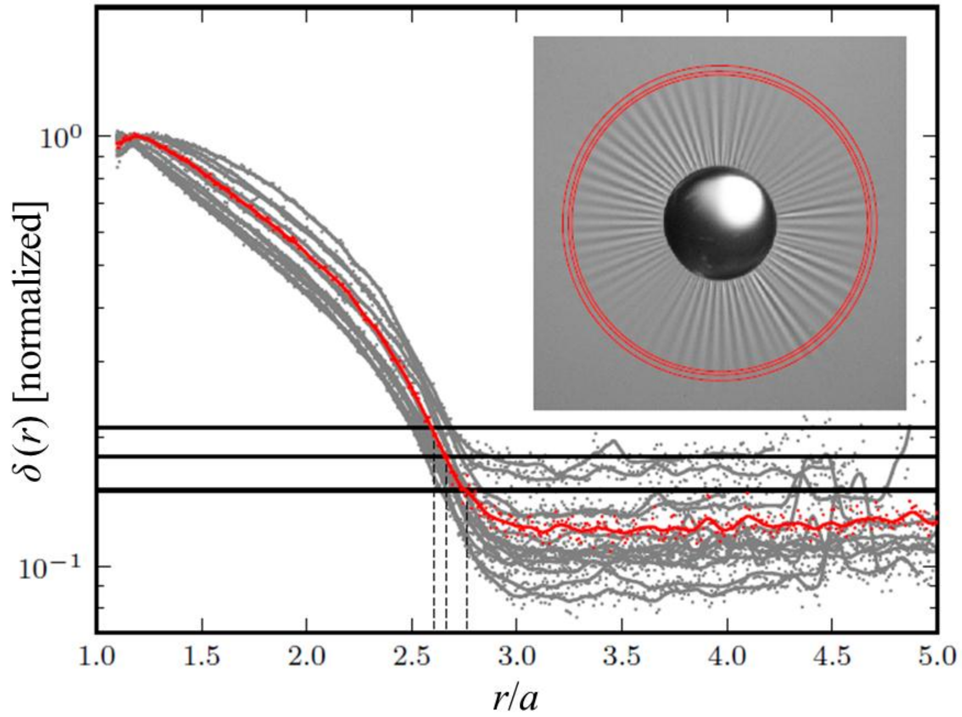

Figure 3. 7: (Copied from Ref: [32]) The standard deviation $\delta\,(r)$ of the azimuthal intensity profile for 14 images of wrinkle patterns of 94 nm-thick sheets. The dots show the raw data; the solid lines show the smoothed data used for the analysis. The three horizontal lines mark the 15%, 18%, and 21% thresholds. The red curve corresponds to the image in the inset, on which are marked the lengths identified by these three thresholds.

To quantify the wrinkle length, we either find the radius r at which $\delta\,(r)$ drops below a threshold fraction of its maximum value (as performed in Ref. [32]); or alternatively, we can detect the radius r at which several consecutive $\delta\,(r)$ values remains above the average noise-level . The noise level in each image varies by position due to the fact that the angle of incident light varies with the position of the floating film within the field of observation. Schroll *et.al.* tested three choices of threshold (15%, 18%, 21% in Fig. 3.7) chosen so that the noise level was rather accurately approximated. For all the data in Ref. [32], 18% threshold was used, which has led to slightly shorter estimates than the actual value of wrinkle length measured by the optical profilometer.

The standard deviation of the azimuthal intensity $\delta\,(r)$ generally demonstrates three characteristic region outside the contact line. The region closest to contact line is characterized with a rapid change in the optical amplitude of wrinkles. After reaching a peak point, $\delta\,(r)$ gradually decays to a plateau related to the background noise level. The overall decay in optical amplitude is determined by two factors. First, the number of wrinkles remains constant along the expanded circles centered around the droplets. Hence, the wavelength of wrinkles increases linearly with the radial distance from the center ($N = \lambda/2\pi r$). As the pitch length of each wrinkle increases, we may expect a general decay in the contrast of the light refracted by the ultrathin sheet floating on water. The actual amplitude of wrinkles also decays as a function of r (Fig. 3.8) which drives the decay in the optical amplitude even faster.

A rapid rise of the optical amplitude is observed only in the close vicinity of the droplet, where $\delta\,(r)$ traces the actual wrinkle profile (measured by OP). A close agreement in two parameters appears until the actual amplitude of wrinkles reaches its peak value. We will exploit this similarity in the following section when the details of the contact line are studied. Now, we would like to pay attention to the other end of this profile, where the automated method relies on the length detection. We find that, despite offering an utterly objective approach, the noise in background makes it difficult to detect the actual length measurable by the profilometer. In contrast, an ordinary inspection performed by ImageJ agrees quite well with the true values with a ~99% precision. As a result, we rely on measurements performed with ImageJ by inspection. Manual method provides the closest agreement with the topographical analysis especially when the tip of wrinkles appearing on the upper left hand corner is considered for the measurement.

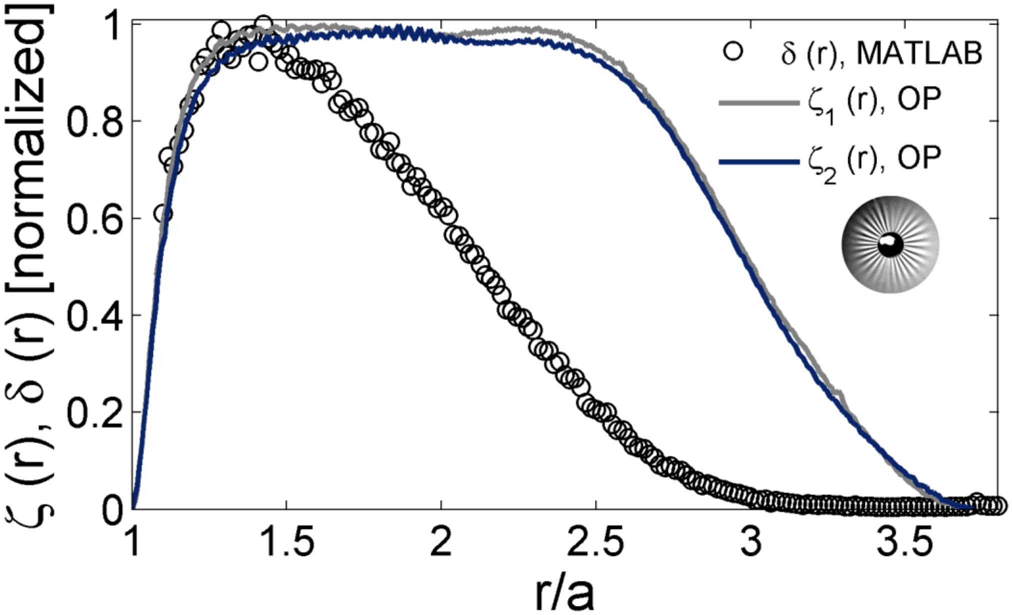

Figure 3. 8: Normalized amplitude of wrinkles, $\zeta(r)$, (solid lines) compared with the normalized standard deviation profile of the azimuthal intensity, $\delta(r)$. The data are from a 111 nm thick PS film floating on glycerol bath and wrinkled by a 0.6 mm wide bubble. Inset is cropped from a bright field image of the actual wrinkled region.

3.8 The contact line

In drop-on-a-sheet experiment, there is an additional complexity at the contact line due to the presence of the wrinkles. As is clear from all the images shown in this dissertation, the wrinkles extend all the way to the contact line. Had the contact line been a free boundary, as in the annular Lamé geometry, then the wrinkle amplitude would have been greatest at the inner boundary. In the geometry we consider here, the contact line is not a free boundary and it is natural to ask whether and how the wrinkles terminate at the contact line. In Fig. 3.9A, we show a bright-field micrograph of the pattern near the contact line of a bubble. This image reveals two remarkable features:

1) There are wrinkles inside the contact line as well.

2) The wrinkles both inside and outside the contact line undergo a cascade to higher wavenumber close to the contact line.

The first of these features may be seen to occur in a drop as well, as shown in the confocal fluorescence micrograph in Fig. 3.9B, and the second of these features is shown in a bright-field close-up of the wrinkle near the drop (Fig. 3.9C).

The existence of wrinkles within the drop is not surprising: as studied in Ref. [17], a flat sheet constrained to live on a curved drop will experience compression at its edges, leading to wrinkles invading the sheet from the free edge. An experimental study of this geometry provided the first detailed validation of a FT analysis for the scaling laws for the length of the wrinkles as a function of the stretching modulus, size of sheet, applied tension and imposed curvature. However, the major difference between those wrinkles and the wrinkles in Fig. 3.9 is that the tips of both the inside and outside wrinkles terminate at the same contact line, which is not a free boundary. This requirement on both inside and outside wrinkle patterns leads to the cascade that is shown in Fig. 3.9.

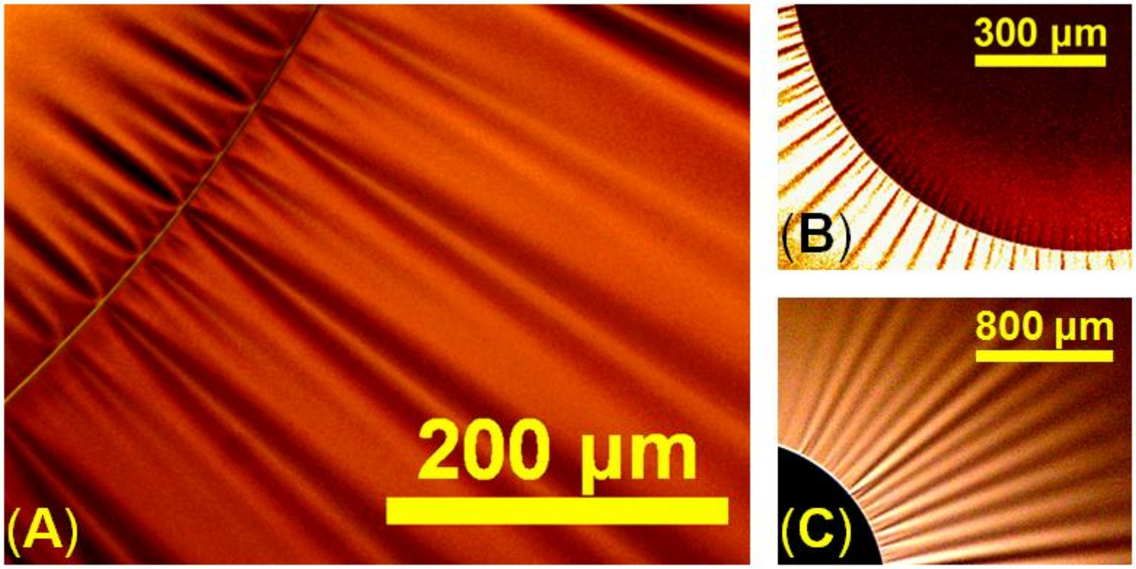

Figure 3. 9: Wavelength refinement near the contact line. (A) An optical micrograph of the sheet near a contact line of a bubble ($a = 0.95$ mm) under a PS film ($M_w = 876k$; $t = 80$ nm). (B) A confocal image of the contact line drop ($a = 0.70$ mm) under a PS film ($M_w = 91k$; $t = 33$ nm). (C) A bright-field image of the contact line drop ($a = 0.82$ mm) under a PS film ($M_w = 91k$; $t = 93$ nm).

To minimize wrinkle amplitude at the contact line, the wavenumber has to increase in order to preserve length in the azimuthal direction. A similar cascade phenomenon can be observed either when the edge is clamped flat (as happens at the top of a curtain[67]), or when there is an energetic cost at the edge of a pattern[13]. When there is tension in the wrinkle direction, such a wrinkle cascade typically proceeds smoothly, by the addition of new fourier modes[68]. It is also evident that the inside and outside wrinkle patterns are in registry with each other.

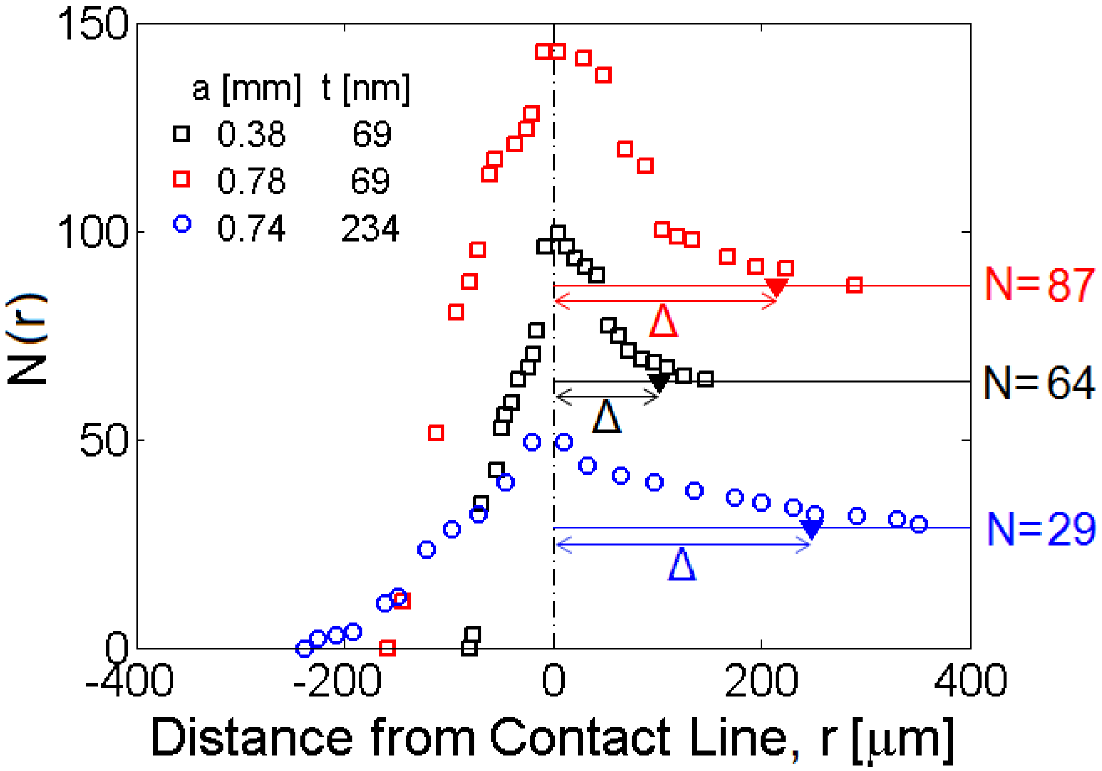

Figure 3. 10: The wrinkle wavenumber increases as the contact line is approached from either side. The data are taken in the bubble-under-sheet geometry with PS films (M_w = 520k). The size of the cascading region outside the drop is labeled Δ.

In Fig. 3.10 we show the refinement of the pattern by plotting the number of wrinkles as a function of distance from the contact line, for two thicknesses and for two drop radii. The wrinkle cascade has a different characteristic length inside and outside the contact line. Inside the bubble, the wrinkle pattern does not develop a bulk value, with the wavenumber cascading down rapidly to zero. The wrinkle pattern extends considerably further outside the contact line; over a lengthscale that we label Δ, the wrinkle number $N(r)$ reaches the steady value N of the wavenumber. This lengthscale is a scale shorter than the length of wrinkles L.

The data in Fig. 3.10 suggest that the bubble radius has a stronger influence on the size Δ of the cascading region than does the thickness. In order to better quantify the dependence on these variables, we measure Δ for varying bubble radii, and for sheets of varying thickness. We obtain Δ from the analysis of the intensity of the bright-field image of the wrinkle pattern. As described in the previous section, after filtering the image to remove low-frequency variations in intensity, we measure the standard deviation of intensity variation in the azimuthal direction, δ, as a function of the radial distance from the contact line, r. $\delta(r)$, has a peak at a value of r that marks the end of the cascading undulations; this measure is shown by the solid triangles in Fig. 3.10 to coincide with the location where $N(r)$ becomes independent of r.

The size of the cascade region was found to be proportional to the bubble radius. We therefore plot the scaled variable Δ/a in Fig. 3.11, against t, the thickness of the sheet. The solid line shows a power-law fit $\sim t^{1/6}$. With this weak dependence, the data are perhaps even compatible with the penetration length of the cascade (Δ/a) being independent of thickness ($\Delta \approx (\gamma_{lv}/\rho g)^{1/2}$ was previously observed in the raft experiment; or controversially, one may empirically suggest that Δ should scale with $(\sigma_{rr}^{+})^{1/2}$, where σ_{rr}^{+}, instead of γ_{lv}, is the tension effective on the smoothening frontier ($\sigma_{rr}^{+}, \sim t^{1/3}$).

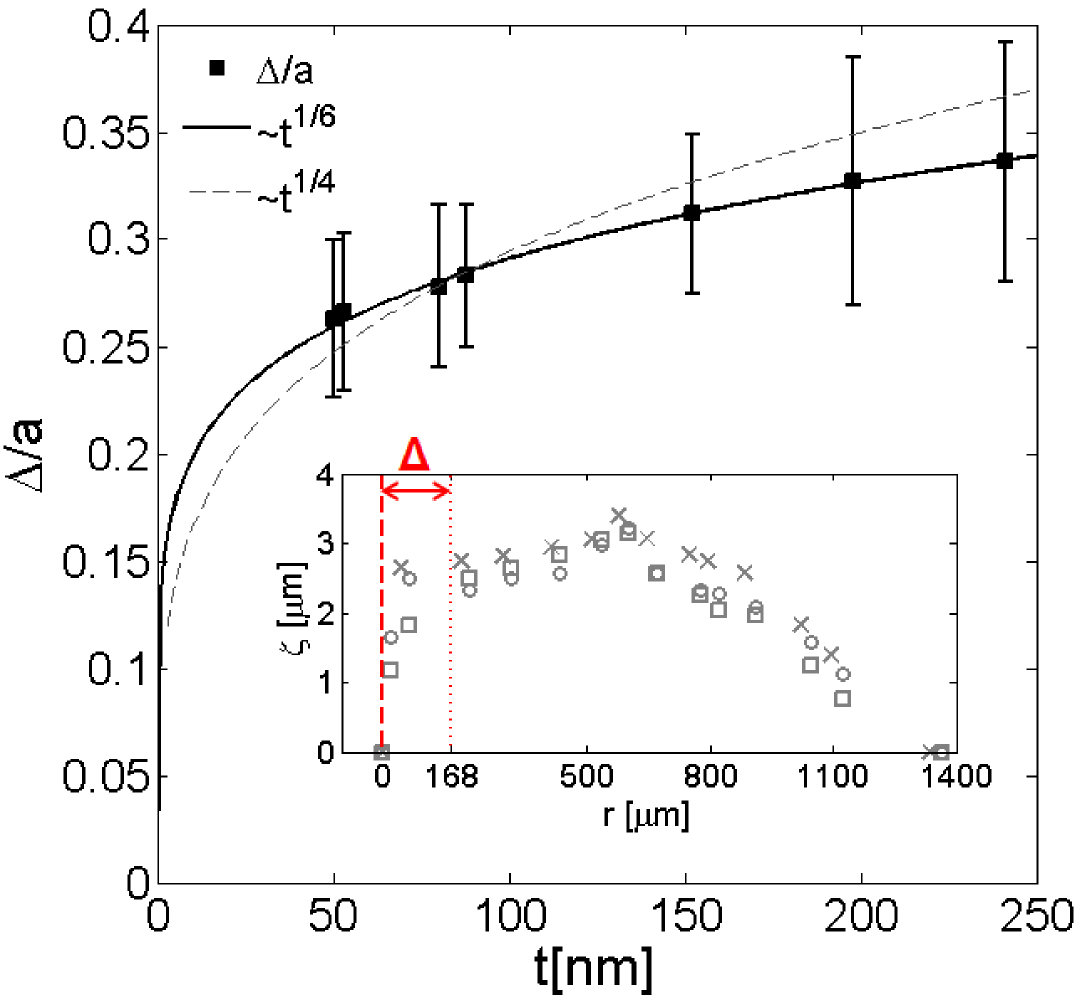

Figure 3. 11: The size of the cascading region Δ outside a droplet scales linearly with *a*. The dependence of Δ on *t* is weak with an empirical exponent, 1/6. Inset: radial height profile of three neighboring wrinkles formed by a droplet (*a* = 0.56 mm) on PS sheet (*t* = 77 nm).

3.9 Wrinkle profile

Within the precision of the confocal microscopy measurement, the contact line lies in a horizontal plane. A cut along an external wrinkle reveals a height profile $\zeta(r)$ that rises rapidly from the contact line in the cascade region *i.e.* for $r < \Delta$, as shown in the inset to Fig. 3.11. After a single-mode pattern emerges, the amplitude slowly dies away with increasing radius as shown in the image in Fig. 3.12A. The wrinkle has a definite terminus, showing that the length L is well-defined. The length L determined from bright-field images coincides with that determined from 3D imaging. In Fig. 3.12A, we show the wrinkle profile $\zeta(r)$ multiplied by wrinkle number N for three sheet thicknesses, each at two drop radii. Within the variability of the experiment, we obtain a collapse of the wrinkle profile when plotted against the radial coordinate normalized by the wrinkle length r/L. A comparison of this shape would be a test of any theoretical development that goes beyond a correct scaling of the variables. The wrinkle profile has been computed in Ref. [62] for the annulus geometry but not for a drop on a sheet.

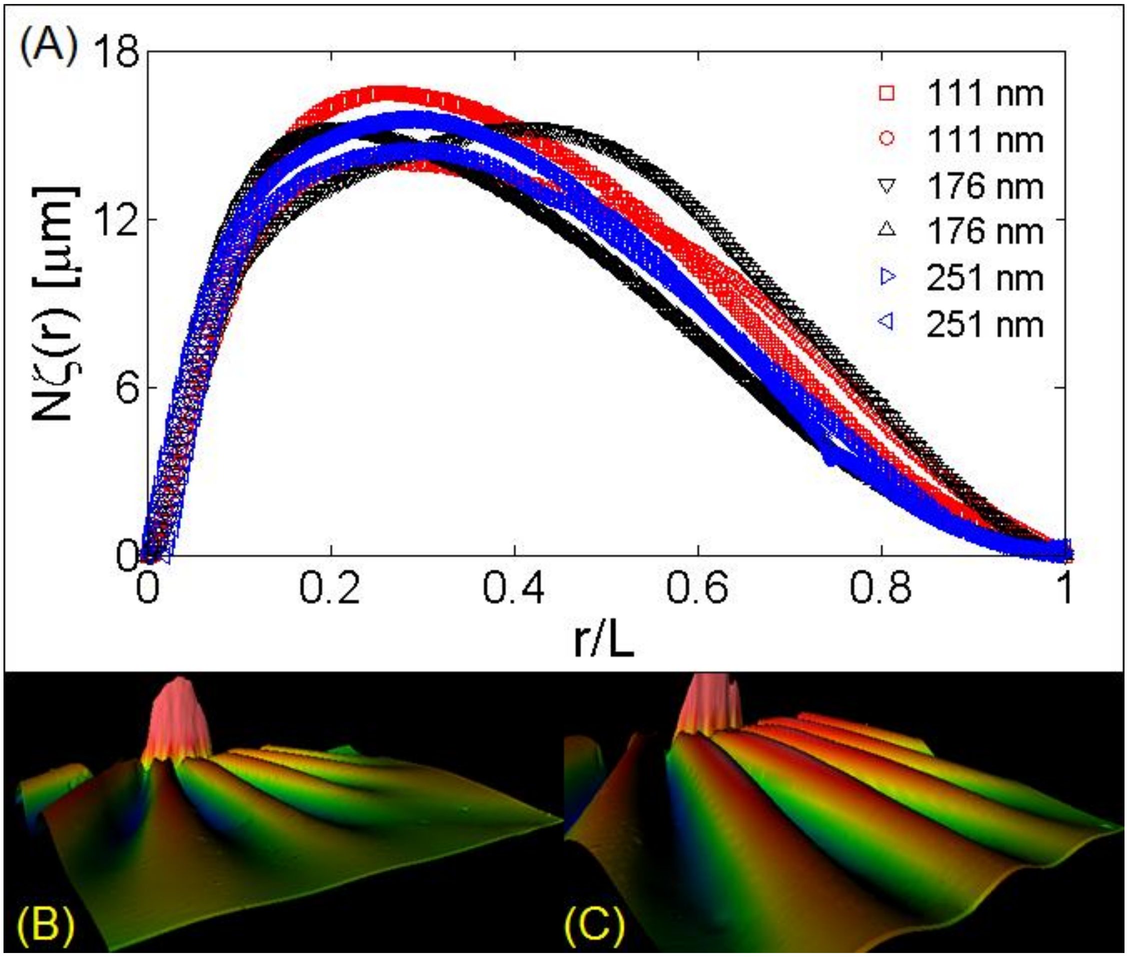

Figure 3. 12: (A) Profile of wrinkles along radial direction for PS (91k) sheets floating on a glycerol bath. The wrinkles are generated by bubbles and the data are obtained from 3D images acquired with an optical profilometer. (B) 176 nm thick PS (91k) film wrinkled by a = 0.29 mm bubble. (C) 176 nm thick PS (91k) film wrinkled by a = 0.34 mm bubble.

3.10 Development of the wrinkle pattern

In the previous sections, we have discussed the attributes of the wrinkle pattern at mechanical equilibrium. Here we discuss the time-dependent development of the wrinkles immediately following the application of the capillary forces, as followed by high-speed video imaging. For these measurements, we employ the bubble-under-sheet protocol. Following the release of the bubble in fluid, buoyancy drives it to the bottom surface of the sheet. After a latency period of a few milliseconds, the spherical bubble bursts and the contact line spreads, rapidly attaining its steady-state diameter.

The bursting of the bubble sets a sharp onset-time for the Laplace pressure and the line tension indicated in Fig. 3.3B. Thereafter, we see an elastic wave rippling outwards from the center at a high speed, and the wrinkle pattern developing in its wake on a slower time-scale than the wavefront. The time-dependence of the development of the length and number of the wrinkles is shown in Fig. 3.13.

The steady-state diameter of the contact line is achieved with the first two milliseconds. As can be seen, the asymptotic values of N and L are established within tens of milliseconds. The surprising aspect of these data is that the final wavenumber is established much earlier in the development of the pattern than is the final length of the wrinkles. This is rather surprising, since the basic idea of the FT theory that so successfully describes the spatial extent of the wrinkle pattern, is that the tension in the radial direction is the dominant energetic component in the pattern. To the first approximation (*i.e.* the leading order of approximation in an expansion in ϵ), the bending energy involved in forming the wrinkles is insignificant. Higher order terms in ϵ

determine the wavenumber. It is therefore counterintuitive that the wavenumber, which is determined by a subtler contribution to the energy, establishes itself before the length of the wrinkle and the overall tensional stress state are fully determined.

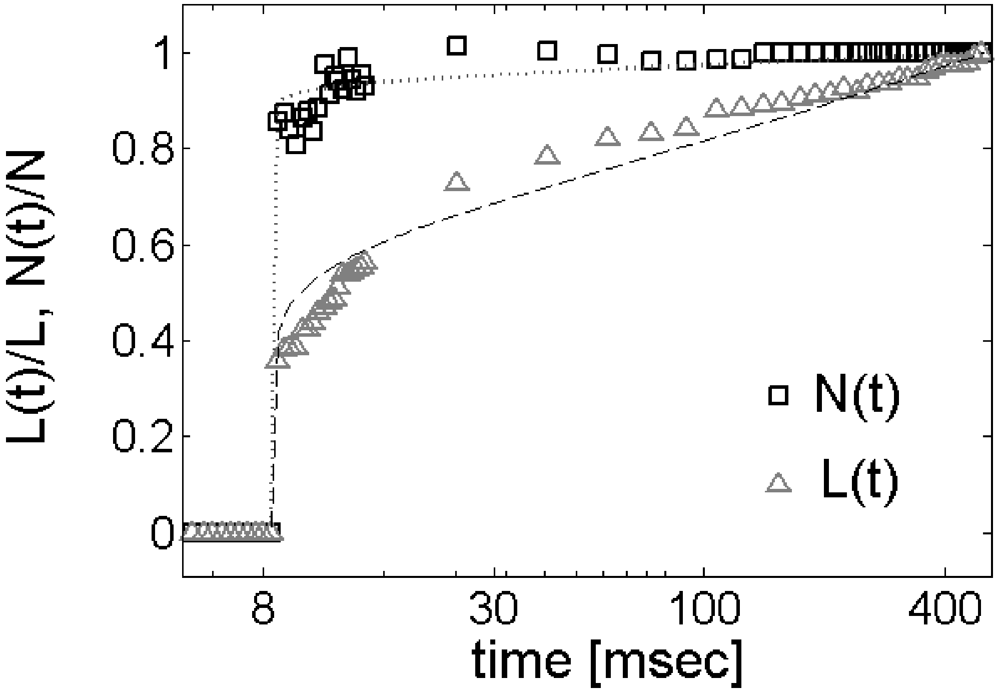

Figure 3. 13: Time dependence of the growth of the wrinkle pattern following the bursting of a bubble underneath a 62 nm PS sheet. *N* and *L* are obtained from bright-field images taken with a high-speed camera.

3.11 Conclusion

The experimental protocol of placing a drop on a floating sheet, or its new counterpart, the bubble under the sheet, have already led to important new developments in our understanding of the wrinkling instability in ultrathin sheets. The results we present here raise new questions. We have characterized the 3D wrinkle profile but still lack a description of it. We do not understand the effect of the wrinkle cascade on either side of contact line. The wrinkle pattern on the inside and the outside of the contact line appear to be in registry with each other. This indicates that azimuthal variations in stress are communicated across the contact line. At a more elementary level, FT theoretical predictions for the wave number are still lacking. In the FT scenario, many wavelengths are unstable to buckling. Which of these are selected will depend on these subtler issues of matching interior and exterior wrinkle patterns at the contact line. These questions will need to be addressed to achieve a quantitative understanding of the wrinkle pattern, which will enable the use of this experimental setting as a metrology for the mechanical properties of thin films, or as a probe of surface energies. However, some of our observations challenge even the qualitative understanding of the mechanics of the wrinkle pattern. Why is it that in the development of the wrinkle pattern, the wrinkle wavenumber is established well before the wrinkle length? We speculate that the underlying explanation for both these observations lies in the fact that the wrinkle tip is always close to the buckling threshold. Thus, it may be that the near-threshold energetic considerations determine the selection of wave number in the incipient pattern. The length of wrinkles could be subsequently determined by the stress field over the entire sheet, which may be relatively indifferent to the bending energy.

CHAPTER 4

WRINKLING OF AN ANNULUS

In this chapter, we study the wrinkling of annular PS sheets floating on water. Wrinkling is induced when the surface tension of water outside the annulus is decreased to a threshold value by gradually increasing the areal density of an insoluble surfactant dispersed around the film.

4.1 Background

Since the study on the stretched rectangular film[11] (Fig. 1.2), patterns forming in a tension field[61] have become an ideal platform to study buckling of elastic sheets. Symmetrically loaded slender discs have attracted considerable attention in this field. Formation of axisymmetric patterns can be classified into two categories with respect to the spatial complexity involved in circular geometries. In the first group, wrinkles occur on a freestanding or supported flat layer [16, 31, 34, 35]. The experiments carried out on a flat configuration have mostly aimed to test the Lamé theory regardless of the imperfections affecting the planar boundaries. In the second group[17, 26-29], the wrinkles occur on a surface that poses a finite curvature, like the patterns forming on a membrane resting at the top of a droplet[17]. In this recent study, King *et.al.* have demonstrated the experimental verification of an uncommon buckling regime, wherein highly bendable sheets possibly relax the compressive stress that forms the patterns. This trend is named as buckling occurring in the far-from-threshold (FT) regime.

The discussion on buckling of extremely bendable sheets in a tension field has moved along with the drop-on-a-sheet experiment[16, 31]. As studied in the previous chapter, the droplet experiment consists of a curved and a flat domain that are bound together with a wrinkled contact line. The dual behavior of the sheet under and out of the droplet creates some challenges when establishing a simple formalism based on the experimental observables. Nevertheless, the practical simplicity in generation and characterization of these highly symmetric patterns promises new discoveries in surface science and materials research. With such motivation, we would like to present a new experiment here that addresses some open questions in wrinkling. Specifically, we would like to discuss the distinguishable role of simple boundary conditions on wrinkle properties. The discrete effects of bending and stretching on the extent of wrinkles are also covered in this chapter.

Our new study is based on the axisymmetric wrinkling of ultrathin polymeric sheets on an artless flat setting. Using differential capillary forces, we control the line tension around a floating annular PS disc while supporting the delicate structure on the smooth surface of a stagnant liquid. Our set-up offers several advantages over preceding efforts[16, 31, 34, 35] that have aimed to impose a controllable tension gradient within a thin elastic membrane. We use a purely two-dimensional geometry relying on the flatness of a trough filled with water. The radial tension exerted at the inner boundary of the film is the surface tension of pure water. The outer boundary is exposed to a lesser force as an insoluble surfactant is gradually compressed around the floating disc. The formation of wrinkles[30], as described in the earlier chapters, relies on the induction of compressive tangential stress due to the rising mismatch between the magnitudes of peripheral forces.

We perform the experiments on a Langmuir trough in order to observe the inception and growth of the patterns in a controlled manner. This is a planar platform that allows us to play with the areal density of the surfactant molecules. The depression in the surface tension, known as the surfactant pressure, Π, is simultaneously recorded as images of the films are taken from the top. We examine the development of wrinkle patterns as a function of load-confinement, τ, and bendability, ϵ^{-1}, which can be introduced as the two dimensionless parameters governing the deformation. Bendability is the ratio of the applied load to the bending modulus of the sheet; while, load-confinement describes a dimensionless measure of compression that is induced in the gradient of the applied tension. Overall, this experiment allows us to isolate the influence of bendability on the extent of wrinkles, while studying the role of load-confinement on the wavelength of the patterns.

4.2 Experimental details

The details on the experimental set-up and sample preparation are described in Chapter 2. Here we present some specific details regarding the experimental protocol and the specimens. The experiments are actuated on Kibron Inc. MicroTroughXS that compresses an insoluble surfactant monolayer outside the annular discs (Fig 4.1). Perfluorododecanoic acid is used as a suitable molecular agent that can form a dispersed monolayer around submicron-thick polystyrene discs. The thicknesses of the sheets used vary between 53 and 276 nm, while the outer diameters are tailored by 15 or 23 mm wide circular patterns. An important geometric parameter can be described as the annular aspect ratio, which defines the ratio of the outer to the inner diameter ($b/a = R_i/R_o$). We symbolize R_i as a and R_o as b (see Fig. 1.4) in order to be consistent with the abbreviations used in the preceding literature [16, 30-32, 60]. The annular aspect ratios studied here are arbitrarily chosen as 3.47 and 5.43. We analyze two additional designs (b/a = 2.70, 10.23) when folding is studied at high compression.

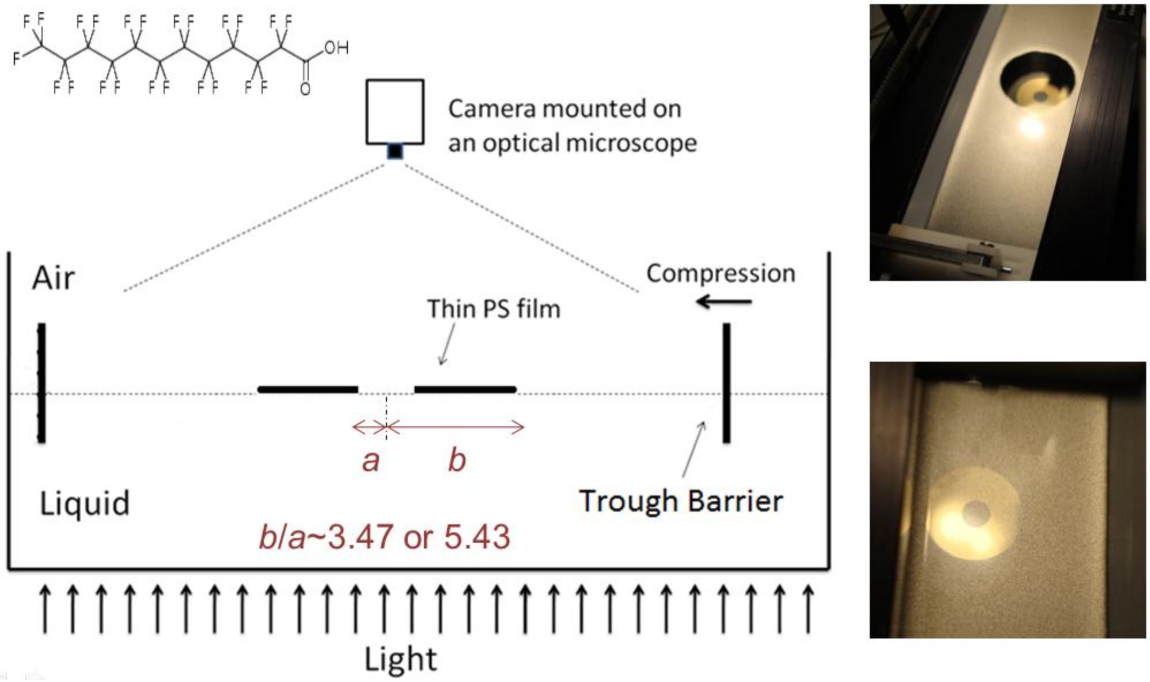

Figure 4. 1: With the aid of a Langmuir trough, we compress a surfactant monolayer (see the molecular structure at upper left corner) around the annulus to initiate wrinkles. As the pattern grows with compression, the extent and wavelength of wrinkles can be monitored as a function of the surfactant pressure, Π.

The surfactant pressure, Π, is varied between 6−10 mN/m and 44−63 mN/m during the compressions. The initial value of Π is arbitrarily set by the deposition, while the highest value of Π considered for analysis is determined by the state of wrinkles.

When any wrinkle in the system reaches the size of the sheet ($R_{wr} \sim b$) we cease analyzing the extent and wavelength of the growing pattern. Strain concentration and folding is observed only after all of the wrinkles reach the system-size and the compression proceeds. Unless the circular shape is dramatically distorted, the folds and wrinkles can be recovered by initializing the positions of the barriers. If a new compression protocol is applied on the relaxed (and cleaned) specimen, the new wrinkles do not necessarily initiate and grow at their original locations. During the routine protocol, the surfactant does not migrate or diffuse into the inner circle. This has been verified with several independent compression tests measuring the surface tension at the center of the circle. The imaging is accomplished using the same optical system facilitating the drop-on-a-sheet experiment reported in Ref. [31].

4.3 Data reduction

Extent, R_{wr}, and wavelength, λ, of wrinkles are significant observables that comprise information regarding the mechanical state of the film. Our set-up allows us to measure these parameters as a function of the compressed monolayer pressure, Π. In Fig. 4.2, we present a sequence of images taken from a 151 nm thick PS film wrinkled under axisymmetric capillary tension. The images are first converted to 8-bit gray scale and conditioned with ImageJ to increase the contrast. In each image, the coordinates of the center of the inner hole, (x_c, y_c) and its diameter, $2a$, are measured in pixels with ~99.9% precision. The tip of each wrinkle is carefully marked by inspection and the wrinkle coordinates (x_{wr}, y_{wr}) are determined. The extent of each single wrinkle from the center of the annulus is calculated using Eq. (4.1).

$$R_{wr} = \sqrt{(x_{wr} - x_c)^2 + (y_{wr} - y_c)^2} \tag{4.1}$$

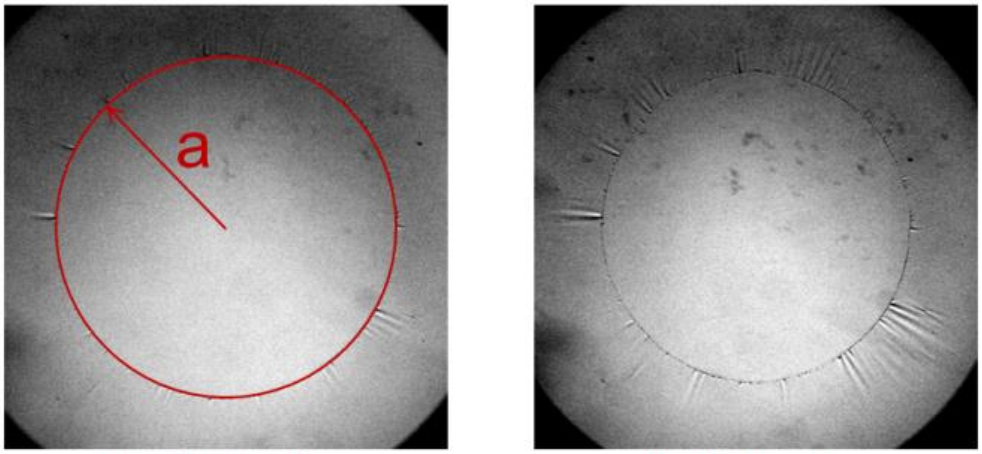

Π=32 dyne/cm Π=36 dyne/cm

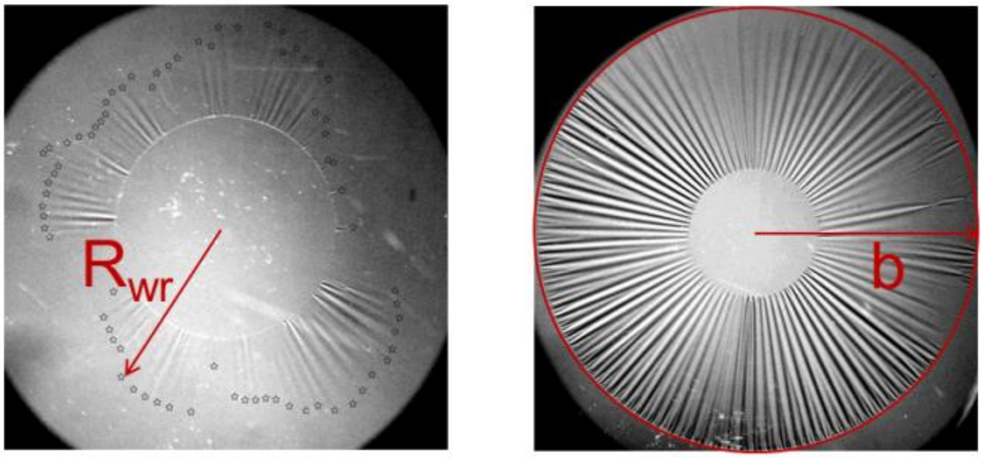

Π=42 dyne/cm Π=47 dyne/cm

Figure 4. 2: Representative steps in wrinkle initiation and growth. The geometric parameters of the problem are demonstrated on the micrographs. In the lower left image, we mark the tip of each wrinkle populating the pattern with a star-shaped marker.

We calculate the separation angle between neighboring wrinkles by referring to the coordinates at the tip of the wrinkles and the center. The average angle of separation between wrinkles, $2\pi/N$, can be calculated by dividing the sum of measured angles to the population of wrinkles.

4.4 Results and discussion

4.4.1 Extent of wrinkles

The most prominent feature of wrinkles occurring on an annulus is that they are not highly symmetric patterns like wrinkles induced by a droplet. The population of wrinkles initiated at the annulus is always less than the number of sites available for a perfectly symmetric pattern with identical wavelength of wrinkles. High symmetry is only attained as the wrinkles extend to the periphery and the gradual nucleation of new wrinkles is complete. For illustration, we exhibit a mature, symmetric pattern ($R_{wr} = b$ condition) at the lower right micrograph of Fig. 4.2.

In Fig. 4.3, we analyze the change in the distribution of the wrinkle extent for the 151 nm thick PS film. The histograms indicate that the average extents of wrinkles represent the characteristic trend within error. Since the distribution is broad, one might prefer plotting the average length (data points in Fig. 4.4) with the single standard deviation (error bars in Fig. 4.4) in the data. In all graphs, the growth of the pattern is kept being analyzed until the extent of any wrinkle reaches the size of the system.

Different sets of data show that wrinkles grow longer with decreasing peripheral surface tension. The overall trend qualitatively agrees with the preceding formalisms established for the length of wrinkles that should initiate and grow with the depression of the exterior tension. What we have found new is that the distribution of the wrinkle extent broadens with the growth of the pattern.

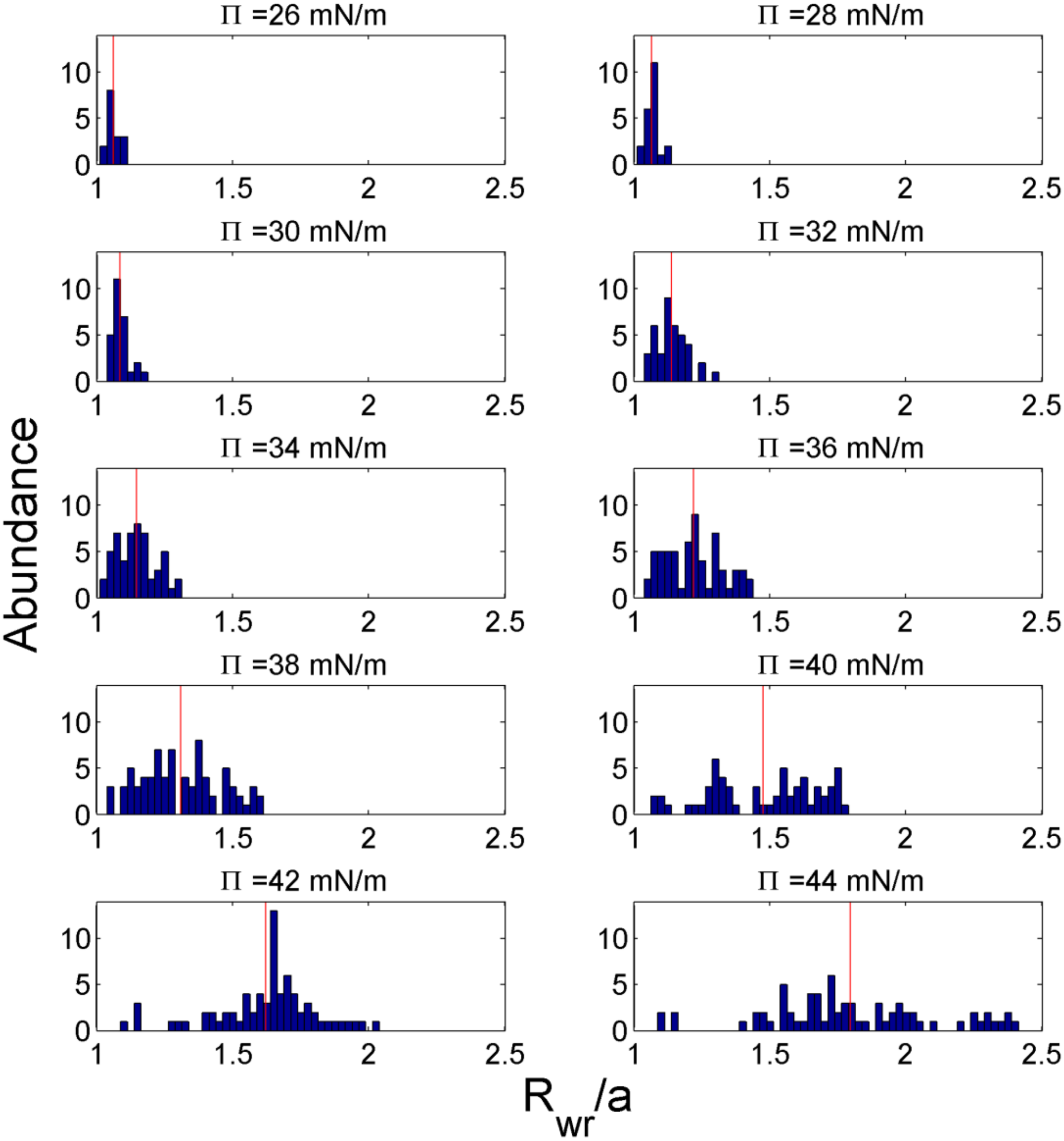

Figure 4. 3: Distribution of wrinkle extent on a 151 nm this PS sheet. The red lines presents the average value of the extent of wrinkle calculated from all wrinkles generated at the reported pressure.

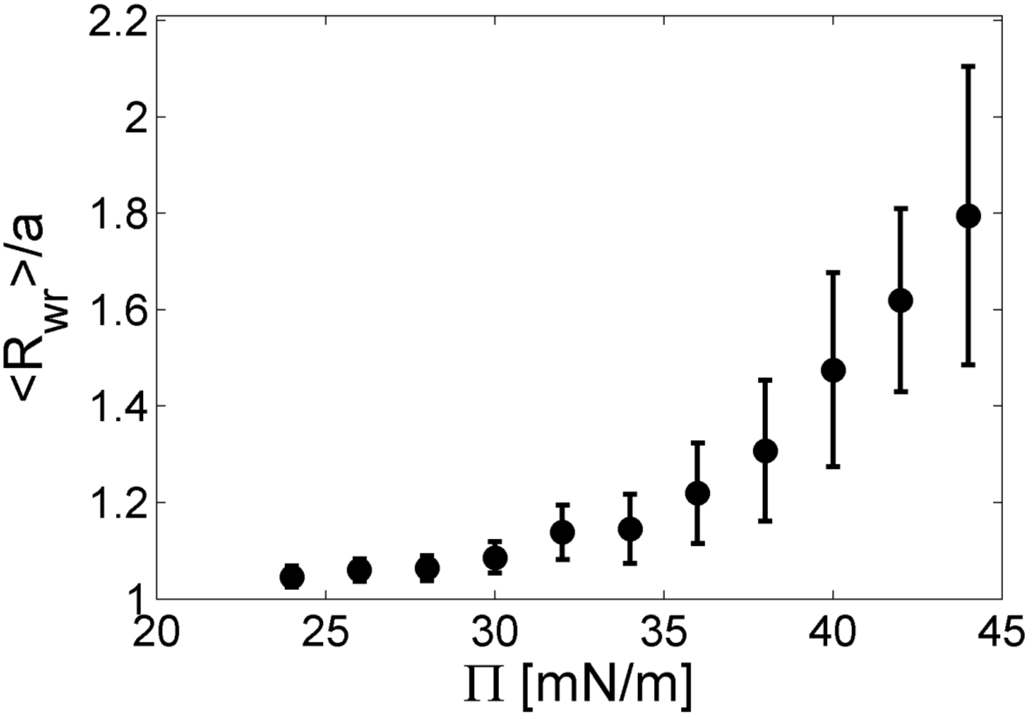

Figure 4. 4: The average extent of wrinkles plotted with error bars being the standard deviation. The data belongs to the 151 nm thick PS sheet (*a* = 3.175 mm, *b*/*a* = 3.47), which is also the subject for Fig. 4.2 and 4.3.

4.4.2 Modeling the annulus

In this section, we present the models developed to understand the stress distribution in the flat and the wrinkled state of the annulus.

4.4.2.1 Lamé solution

In the 19th century, Gabriel Lamé studied the static equilibrium of a thick-walled cylinder that is loaded by hydrostatic pressure. The unwrinkled state of the annulus can be solved using this historical derivation, as both problems are geometrically identical (Fig. 1.4). We will present a detailed solution here as an alternative to another solution found in Ref. [33]. First, let us consider an infinitesimal element (Fig. 4.5) located at some radius *r* and defined by an angular portion $d\theta$, and a radial increment dr. Due to the axial symmetry, the stress functions merely depend on *r* while the shear stress on the element is zero. Therefore, the radial force equilibrium can be simply written:

$$(\sigma_{rr} + d\sigma_{rr})(r + dr)d\theta = \sigma_{rr} r d\theta + \sigma_{\theta\theta} d\theta dr \tag{4.2}$$

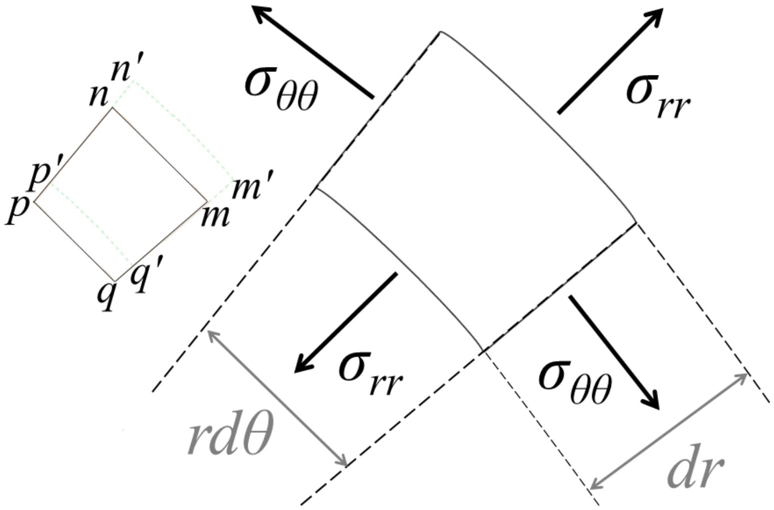

Figure 4. 5: An infinitesimal element in equilibrium under axially symmetric tension gradient is the basis for the model. The material is displaced only in the radial direction.

When second order terms are ignored, Eq. (4.2) can be rearranged into Eq. (4.3) in the absence of body forces.

$$\frac{\sigma_{rr}}{dr} + \frac{\sigma_{rr} + \sigma_{\theta\theta}}{r} = 0 \tag{4.3}$$

In order to determine a relationship between the stresses and the boundary forces, we consider the Hookean constitutive equations and the strain functions.

Initially, we identify that there is only radial displacement in the element. Therefore, the points marked with letters *p*, *q*, *m* and *n* in Fig. 4.5 displace to their new positions *p*\`, *q*\`, *n*\` and *m*\` respectively. As a result, the radial strain can be written as the ratio of the net displacement, du_r, to the original length, *dr*.

$$\varepsilon_{rr} = {du_r}/{dr} \tag{4.4}$$

In hoop direction, the line *pq* has a length $rd\theta$ and line *p*\`*q*\` has length $(r+u_r)d\theta$. With this knowledge in mind, the tangential strain can also be written:

$$\varepsilon_{\theta\theta} = \frac{(r+u_r)d\theta - rd\theta}{rd\theta} = \frac{u_r}{r} \tag{4.5}$$

Hooke's law defines the linear elastic relation between the stress and the strain functions, where *E* is the elastic modulus and *v* is the Poisson's ratio of the material:

$$\varepsilon_{rr} = (\sigma_{rr} - \upsilon\sigma_{\theta\theta})/E \tag{4.6a}$$

$$\varepsilon_{\theta\theta} = (\sigma_{\theta\theta} - \upsilon\sigma_{rr})/E \tag{4.6b}$$

Solving Eq. (4.6) for stresses, and substituting strain functions with respect to Eq. (4.4) and (4.5), we find the following equations:

$$\sigma_{rr} = \frac{E}{1-\upsilon^2}\left(\frac{du_r}{dr} + \upsilon\frac{u_r}{r}\right) \tag{4.7a}$$

$$\sigma_{\theta\theta} = \frac{E}{1-\upsilon^2}\left(\frac{u_r}{r} + \upsilon\frac{du_r}{dr}\right) \tag{4.7b}$$

Now, stress functions are represented by a single variable, u_r, *i.e.* the radial displacement. We can further solve Eq. (4.3) using Eq. (4.7a) and (4.7b), leading us to the following differential equation:

$$\frac{d^2u_r}{dr^2} + \frac{du_r}{rdr} + \frac{u_r}{r^2} = 0 \tag{4.8}$$

The Eq. (4.8) has a simple solution, $u_r = C_1 r + C_2/r$ which can be implemented into the stress functions at Eq. (4.7) and the following boundary conditions, $\sigma_{rr}\,(r = R_i) = T_i$ and $\sigma_{rr}\,(r = R_o) = T_o$. As a result, the following formulas on the stress distribution can be found:

$$\sigma_{rr} = (T_i - T_0)\left(\frac{R_i^2 R_o^2}{R_0^2 - R_i^2}\right)\frac{1}{r^2} + \frac{T_o R_o^2 - T_i R_i^2}{R_o^2 - R_i^2} \tag{4.9a}$$

$$\sigma_{\theta\theta} = -(T_i - T_0)\left(\frac{R_i^2 R_o^2}{R_0^2 - R_i^2}\right)\frac{1}{r^2} + \frac{T_o R_o^2 - T_i R_i^2}{R_o^2 - R_i^2} \tag{4.9b}$$

In this form, Lamé solution portrays the stress distribution in a disc that is symmetric around the central axis. The out-of-plane component of the stress is neglected due to the reduced dimensionality. This solution should apply to the unwrinkled state of the sheet floating on water.

We find that the radial stress remains positive everywhere for T_i, $T_o > 0$, while the hoop stress becomes compressive only if there is a large mismatch between the boundary forces, *i.e.* $T_i/T_o > 2$. According to the post-buckling approach, the compressive region formed in a sufficiently flat thin layer induces a wrinkled region (in, so-called, Near Threshold regime). As a result, wrinkles occurring at the center mark the region of the negative hoop stress; where, the radius of the wrinkled region attains the following form:

$$R_{NT} = R_i\sqrt{\frac{T_i - T_o}{T_o - T_i\dfrac{R_i^2}{R_o^2}}} \tag{4.10}$$

For a line tension exerted along a small centric hole ($R_i << R_o$), the equation (4.10) reduces to a more simple representation, (4.11).

$$R_{NT} = R_i\sqrt{\frac{T_i}{T_o} - 1} \tag{4.11}$$

4.4.2.2 FT solution

Now, we would like to describe the other buckling regime where thin films are wrinkled by forces much larger than the critical loads required to induce buckling. In this regime, compressive stress is presumed to vanish along wrinkles modifying the stress distribution on the sheet. According to Davidovitch *et.al.* [30], two characteristic regions exist in the film. In the wrinkled region ($R_i < r < R_{FT}$), the hoop stress is collapsed ($\sigma_{\theta\theta} \rightarrow 0$), therefore, the force balance in Eq. (4.3) acquires a new form:

$$\sigma_{rr} = T_i \frac{R_i}{r} \tag{4.12}$$

From equation (4.6), the corresponding strain functions can be trivially derived using Hooke's law and the Eq. (4.12),

$$\varepsilon_{rr} = \frac{T_i}{Y}\frac{R_i}{r} \tag{4.13a}$$

$$\varepsilon_{\theta\theta} = -\upsilon \frac{T_i}{Y}\frac{R_i}{r} \tag{4.13b}$$

The sheet surface is free of singularities; therefore, conditions of continuity hold when the stress functions are written. Outside the wrinkled region ($R_{FT} < r < R_o$), stress is distributed in agreement with the classical Lamé form, where $R_i \rightarrow R_{FT}$ and $T_i \rightarrow T_L = T_iR_i/R_{FT}$. In order to find the size of the wrinkled region, Davidovitch *et.al.* computed the elastic energy $U_E = 1/2\int A dA(\varepsilon_{rr}\, \sigma_{rr} + \varepsilon_{\theta\theta}\, \sigma_{\theta\theta})$ of the modified stress field over the whole area of the film[30]. Minimizing the mechanical energy U, ($U = U_E - W$; W: the input work $W \sim T_oR_o + T_iRi$), they calculated the radius of the wrinkled region (for $R_i << R_o$),

$$R_{FFT} = \frac{R_i}{2}\frac{T_i}{T_o} \tag{4.14}$$

Now, we would like to find an expression for the extent of FT wrinkles occurring on a membrane with a high annular aspect ratio, ($R_i/R_o \leq 1$). Solving the hoop stress (Eq. (4.9b)) at the tip of the wrinkles (at $r = R_{wr}$), we find the following polynomial relation,

$$T_{wr}(R_o^2 + R_{wr}^2) = 2T_oR_o^2 \tag{4.15}$$

where T_{wr} can be introduced as the magnitude of tension at the tip of the wrinkle and simply calculated as $T_{wr} = T_iR_i/R_{wr}$ using Eq. (4.12). The real root of the polynomial function $(T_iR_i)R_{wr}^2 - (2T_oR_o^2)R_{wr} + (T_iR_iR_o^2) = 0$ provides a representation for R_{FT} as $R_o/R_i \rightarrow 1$. Consequently, the extent of wrinkles in FT regime can be formulated, where the annotation R_{FT} is substituted for R_{wr}:

$$R_{FT} = R_i \frac{T_o}{T_i}\left(\frac{R_o}{R_i}\right)^2 \left[1 - \sqrt{1 - \left(\frac{T_iR_i}{T_oR_o}\right)^2}\right] \tag{4.16}$$

4.4.2.3 Wrinkling thresholds

After deriving the equations of the extent of wrinkles, we can work on some algebra that solves the threshold condition required to initiate wrinkling. From the definition of the critical load, one can assume that R_{wr}/R_i takes the value, 1 as load-confinement τ reaches its critical value at τ_c. Therefore, we can rearrange the equation (4.10) into the following form (as $\tau \rightarrow \tau_{c,NT}$; $R_{NT} \rightarrow R_i$):

$$\frac{R_{NT}}{R_i} = \sqrt{\frac{\tau_{c,NT} - 1}{1 - \tau_{c,NT}\left({}^{R_i}/_{R_o}\right)^2}} \equiv 1 \tag{4.17}$$

Following some algebraic steps, one can easily work with Eq. (4.17) to introduce a critical value for load-confinement:

$$\tau_{c,NT} = \frac{2}{1 + \left({R_i}/{R_o}\right)^2} \tag{4.18}$$

Eq. (4.18) shows that $\tau_{c,NT}$ converges to 2 as the annular aspect ratio b/a ($R_i=a$, $R_o=b$) goes to infinity, which is formally identical to the learning from Eq. (4.11).

We can apply the same derivation to Eq. (4.15) to calculate the critical load-confinement required to initiate wrinkles in the FT regime. We start with the following treatment, $\tau \rightarrow \tau_{c,FT}$; $R_{FT} \rightarrow R_i$:

$$\frac{R_{FT}}{R_i} = \frac{1}{\tau_{c,FT}}\left(\frac{R_o}{R_i}\right)^2\left[1 - \sqrt{1 - \tau_{c,FT}^2\left(\frac{R_i}{R_o}\right)^2}\right] \equiv 1 \tag{4.19}$$

When solved for $\tau_{c,FT}$, Eq. (4.19) intriguingly leads us to the same result derived for the NT buckling regime:

$$\tau_{c,FT} = \frac{2}{1 + \left({R_i}/{R_o}\right)^2} \tag{4.20}$$

Overall, we found that the buckling threshold of an annulus depends merely on the annular aspect-ratio when bendability is neglected. In both regimes, the critical τ required to induce wrinkling must be a numerical value between 1 and 2. One should also keep in mind that these solutions ignore the bendability of the sheets and do not represent the whole picture. As a result, neither Eq. (4.18) $\tau_{c,NT}$, nor Eq. (4.20) $\tau_{c,FT}$ depends on thickness. Similarly, Eq. (4.10) and (4.16) do not predict any thickness dependence for the extent of wrinkles, where the wrinkle length is merely dictated by the geometry and the boundary conditions.

4.4.3 Data analysis

In this section, we will compare the length data with the predictions discussed in the previous section. The data was taken from PS sheets of high bendability (ϵ^{-1}~10^5−10^6) and moderate annular aspect ratios (b/a~3.47, 5.43). Thicknesses of the samples ranged between 53 and 276 nm, probing a fairly broad regime of bendability while causing small out-of-plane deformations. Extreme thinness, thanks to maintaining small amplitude of wrinkles, prevents significant distressing of the pattern via subphase deformation. We can support this notion referring to the droplet experiment[31] where the amplitude of wrinkles occurring on identical films scales linearly with the wavelength of the pattern (see Fig. 3.12). We know that a free standing sample[11], unbound from the gravitational effects of a supporting layer, is also expected to exhibit a linear dependence.

The experimental values of the wrinkle length do not trivially agree with any available model, as they systematically vary with the film thickness. We postulate that, unlike the droplet experiments, the thickness dependence observed here is liberated from the loading conditions imposed onto the material. Therefore, the results are expected to reveal the anonymous role of the buckling threshold on the properties of the pattern. As shown in Fig. 4.6, wrinkles start to appear earlier and grow larger on the films with higher thicknesses. This behavior is rather puzzling as the general formalism on buckling fails to justify the unusual trend that thicker films are more easily wrinkled. Nevertheless, as the thickness gets even smaller, the discrepancies between the models and the observations disappear. The close agreement verifies the applicability of the FT theory on the films of extreme bendability, where the bending energy, indeed, has a minor role in determining the extent of wrinkles.

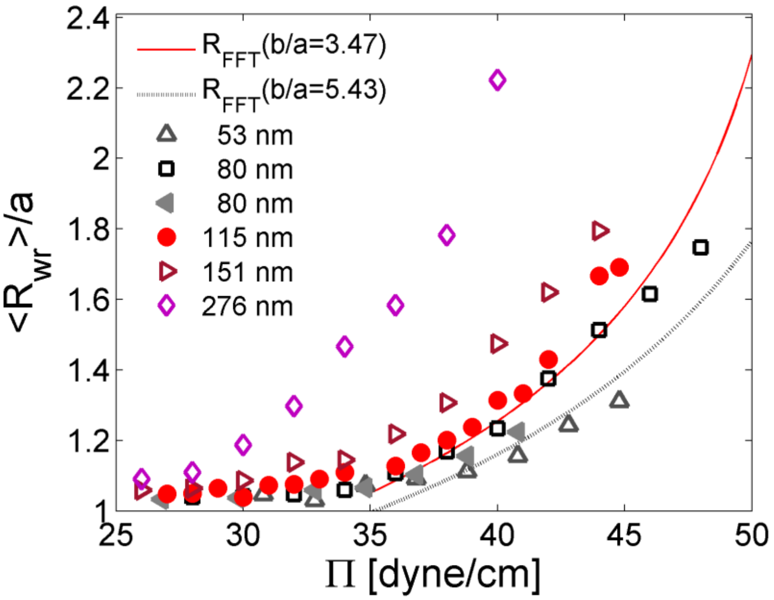

Figure 4. 6: Extents of wrinkles normalized and plotted against the surfactant pressure. The experimental results generally fall above the theoretical predictions that ignore the effect of bending.

An interesting physical phenomenon occurs when the data in Fig. 4.6 is displaced in horizontal, *i.e.* along the pressure axis. We present six sets of data belonging to two different annular aspect ratios and five different thicknesses; yet, each individual set of data can be superimposed on a single theoretical curve (see Fig. 4.7) computed for negligible bendability in the system. We also know that the growth of wrinkles should follow a trend predicted by the FT model; just like identical films forming highly symmetric FT patterns on the curved surface of a tiny droplet. In this preceding study of so-called sheet-on-a-drop experiment[17] wrinkling patterns were discovered to exhibit FT characteristics, while the mechanism of deformation in that study lacked the sensitivity of detecting a thickness dependence on the extent of wrinkles.

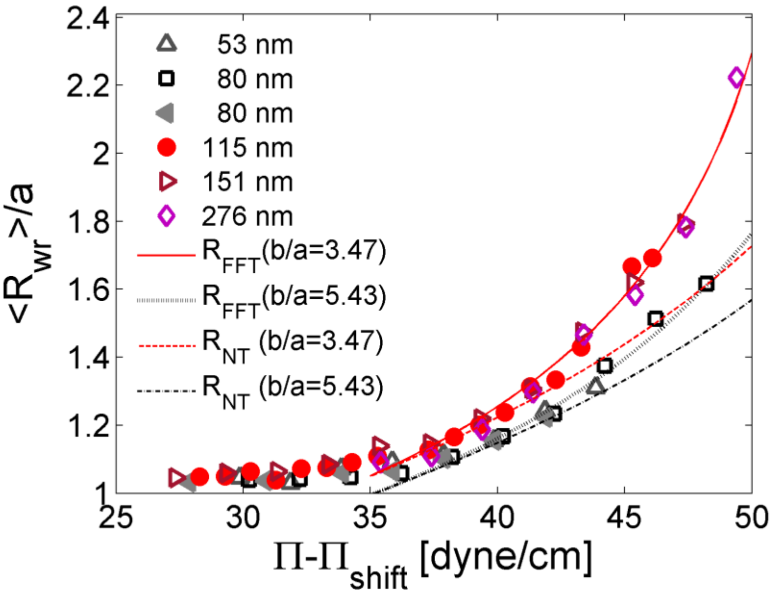

Figure 4. 7: The data presented in Fig.4.6 is shifted along abscissa and collapsed on the curves predicted for FT scaling.

When our experiment is compared with the identical sheets resting on a droplet, the wrinkle length grows rapidly on an annulus with a linear dependence on the boundary forces ($L \sim \tau$). In contrast, in the preceding work, the length of wrinkles scales slower with the analogous parameter ($L \sim \alpha^{1/5}$). This discrepancy might have created a challenge in perceiving a solid conclusion on the thickness dependence. In addition, sheet-on-a-drop experiment probes a regime of higher bendability, where the thickness of sheets might already have a diminished effect on the extent of wrinkles. Therefore, the role of thickness on the threshold was not isolated in the former study and remained as a new discovery to be revealed here.

Our results might include some imperfections associated with sample preparation and measurements. In Fig. 4.7, the data points falling below ($R_{wr}/a <$) 1.10 seem to remain off the general trend traced by the theoretical calculation. The deviation could be related to the micro-burrs generated during the sample preparation. Hereafter, we will merely present the data for values remaining above the $R_{wr} = 1.10a$ confidence level. We also include the error bars in Fig. 4.8 when presenting the variance in the final representation of the data. Despite possible experimental error, the FT trend is characterized again for the extent of wrinkles, even more explicitly in the regime of large compressions.

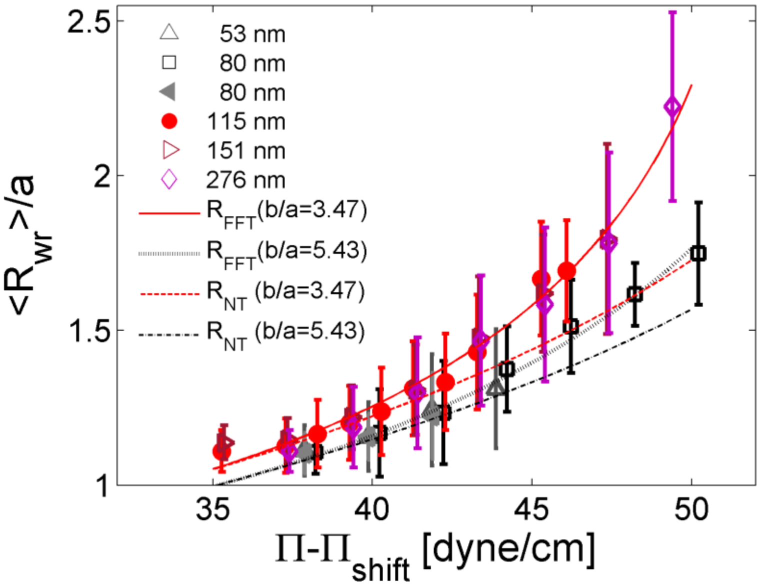

Figure 4. 8: The normalized extent of wrinkles presented with the standard deviation bars. Red-scale data is retrieved from $b/a \sim 3.47$ aspect-ratio sheets, while gray-scale data belongs to the set with $b/a \sim 5.43$ aspect-ratio.

We propose multiple techniques to compute the wrinkling threshold from the experimental data. The accuracy and relevance of each method will remain as an open theoretical discussion. We first start with the most trivial approach studying the raw data (*i.e.* R_{wr} vs. Π) plotted in Fig. 4.6, and quantifying the points at abscissa where wrinkles are initiated. Accurate detection of τ_c depends on an unbiased numerical computation of the Π_c values. Our solution is based on displacing the data along abscissa and minimizing the difference between the experimental and the theoretical ordinate values. Using the least squares fitting algorithm, the proper shift factor, hence the actual Π_c, can be computed for minimized square of the error.

On the other hand, the same algorithm can be applied on the raw data presented in an alternative format (*i.e.* R_{wr} vs. τ), which requires the modification of the reference curve for superposition (Eq. (4.16)). The shift values, again, can be solved using the least square fitting algorithm. The outcome of the both approaches is summarized in Figure 4.9. Overall, a similar dependence of τ_c on bendability is detected, while, the magnitude of computed values slightly differ (Fig. 4.10 and 4.11). We also observe that the data belonging to the thickest film (276 nm) remains off the trend traced by the theoretical $R_{wr}(b/a, \tau)$ curve plotted in Fig. 4.11.

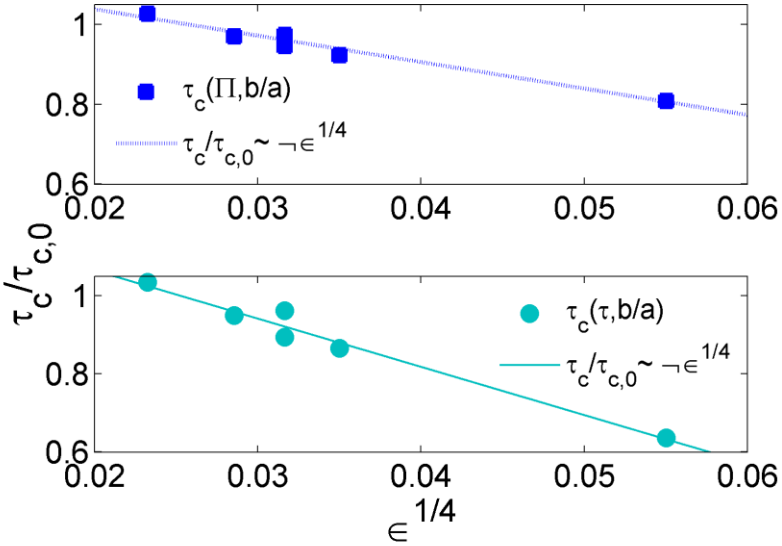

Figure 4. 9: Wrinkling threshold (normalized with theoretical value calculated for ϵ=0) values are computed by superimposing the raw data in (**top**) $R_{wr}(b/a, \tau)$ and (**bottom**) $R_{wr}(b/a, \Pi)$ representations. Both sets scale linearly with $\epsilon^{1/4}$.

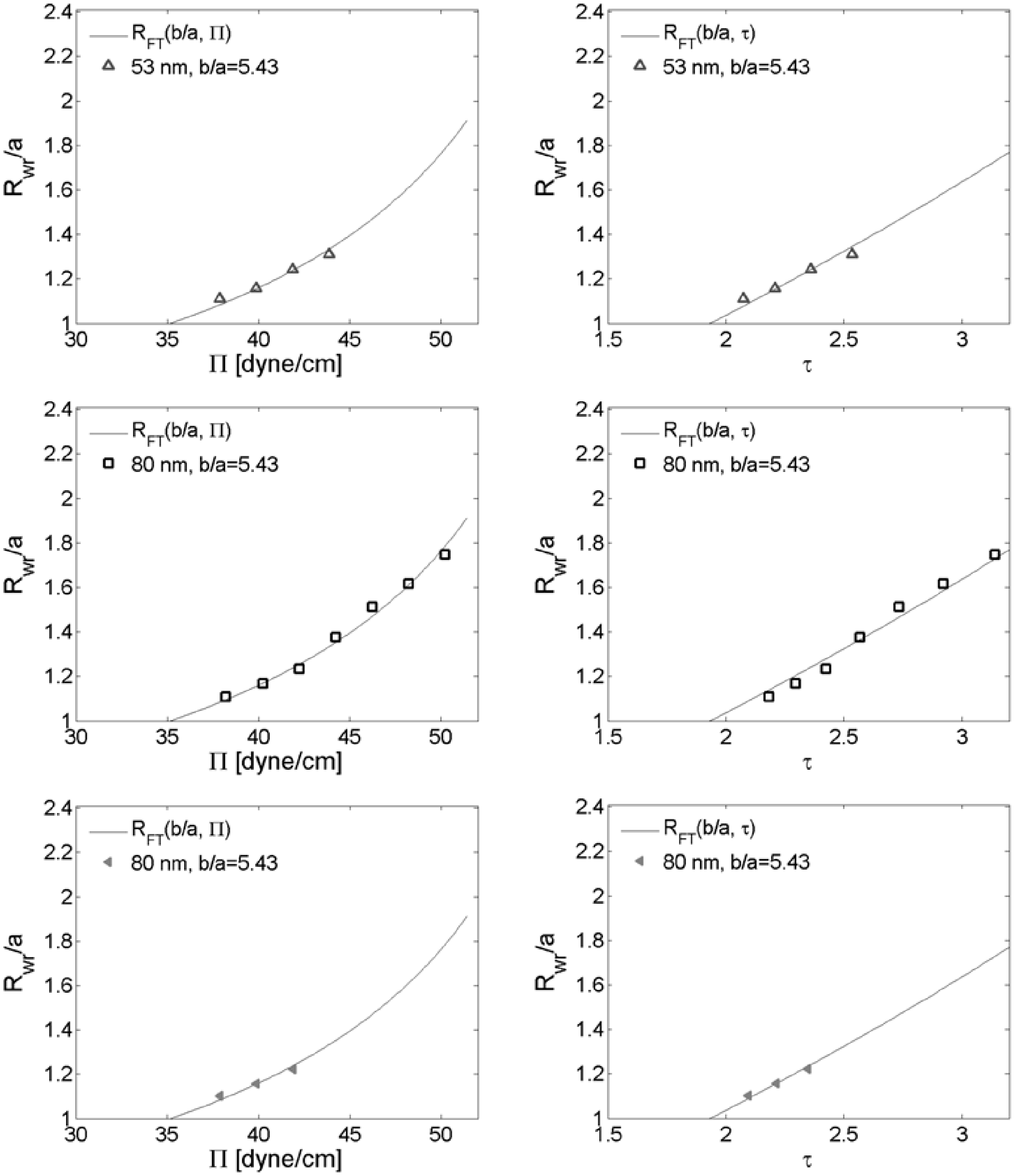

Figure 4. 10: Experimental values (when *b*/*a*=5.43) are superimposed on the theoretical curves using the least squares algorithm. Left hand ($R_{wr}(b/a, \Pi)$) and right hand $R_{wr}(b/a, \tau)$ sides are the distinct representations of the identical raw data.

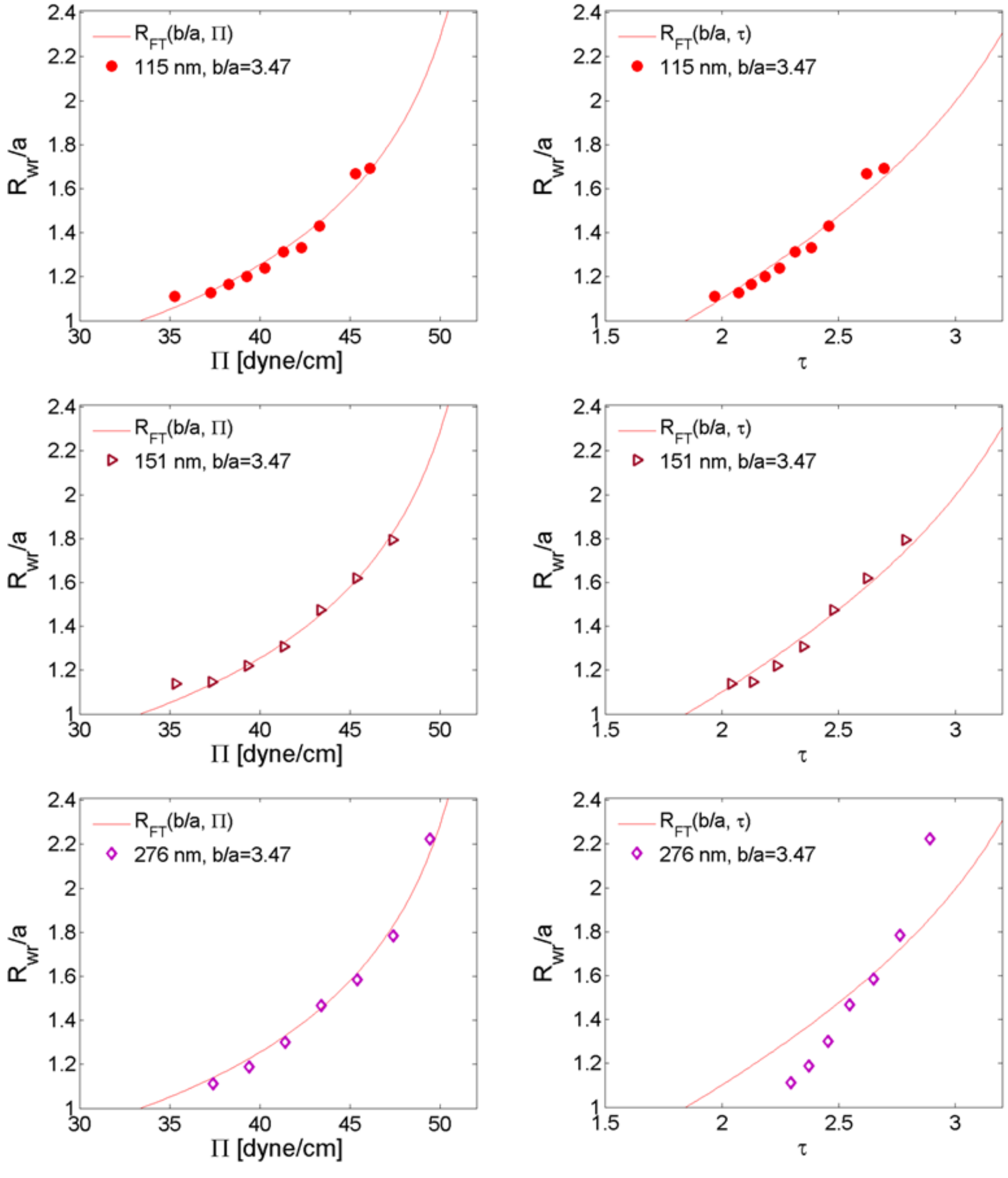

Figure 4. 11: Experimental values (when *b*/*a*=3.47) are superimposed on the theoretical curves using the least squares algorithm. Left hand ($R_{wr}(b/a, \Pi)$) and right hand $R_{wr}(b/a, \tau)$ sides are the distinct representations of the identical raw data.

Lastly, we fit the data to a new functional form that replaces the geometric parameter (*b*/*a*) in the main equation. We substitute the annular aspect-ratio term from Eq. (4.19) with the $\tau_{c,FT}$ representation found in Eq. (4.20). Hence, the extent of wrinkles can be written as a function of load confinement and its critical correspondent:

$$\frac{R_{FT}}{R_i} = \frac{1}{\tau}\left(\frac{\tau_c}{2-\tau_c}\right)\left[1-\sqrt{1-\tau^2\left(\frac{2-\tau_c}{\tau_c}\right)}\right] \tag{4.21}$$

This equation ideally would allow us to compute τ_c using a single fit parameter, and offer an opportunity to evaluate the prior technique without superimposition. However, we have found that the application of this alternative method is limited, as we could only fit the first four sets of the data (53-115 nm; $\tau_c > 1.80$) successfully using a single fit parameter.

When the thicker samples (151 and 276 nm; $\tau_c < 1.70$) are analyzed, a single fit parameter (smaller than 1.74) creates imaginary values at the ordinate. Therefore, in the numerical analysis, we again have to displace the data along, τ-axis, in order to perform a reasonable fit that minimizes the error. In Fig. 4.12, we report the critical values of the τ as the summation of the two independent parameters computed from the least square error procedure. In Table 4.1, we compare the τ_c values computed from the original superposition and the single parameter fitting analyses, where the values from two independent procedures coincidentally agree with each other.

Table 4. 1: τ_c values computed from fitting curves on R_{wr}/a vs. Π and R_{wr}/a vs. τ data.

t [nm]	**53**	**80**	**80**	**115**	**151**	**276**
τ_c from R_{wr}/a vs. Π	1.99	1.83	1.88	1.79	1.70	1.49
τ_c from R_{wr}/a vs. τ	1.96	1.79	1.84	1.80	1.65	1.41

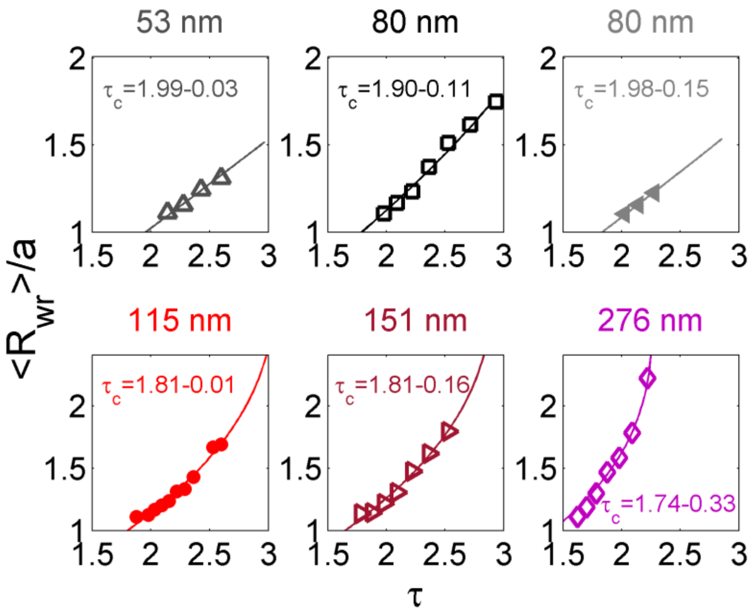

Figure 4. 12: Normalized wrinkle extent plotted against load-confinement allows us to compute τ_c for each set of data presented in Fig. 4.6 and 4.7. Symbols are experimental data points. Solid lines are the numerical fits calculated with Eq. (4.21) and superimposed on to the actual data by the subtracted values.

Overall, regardless of the fitting method, we find the experimental trend rather puzzling. According to Fig. 4.9, thicker films are again demonstrated to be wrinkled more easily, which is in contradiction with the fundamentals of buckling. The empirical scaling $\tau_c \sim \epsilon^{1/4}$ computed from data is in agreement with the exponent proposed by Davidovitch *et.al.*, however, the phase diagram presented in Fig. 1.6 indicates a decay of τ_c with decreasing film thickness. We hope that our findings will initiate an interesting scientific debate in future, as we do not have a clear understanding on this unusual behavior. Now, we would like to investigate the boundary conditions in order to clear any possible doubts on the proposed mechanism of deformation.

4.4.4 Verification of boundary conditions

In wrinkling of an annulus, we have assumed that the boundary conditions are trivial and maintain practical elegance. We have experimentally verified that the surface tension, γ_i at the center of the annulus remains unchanged during routine compressions. We also have assumed that the liquid tension pulling the contact-lines exerts axisymmetric planar forces on the material. Therefore, in our analyses we equate the tension, T_o acting at the outer boundary to the differentiable surface tension, γ_o imposed by the liquid and the surfactant. In order to verify this approach, a new measurement on identical films was performed, merely changing the means of loading at the center.

In order to understand how a floating sheet is kept taut on a liquid, a familiar experiment is revisited. A PS disc is floated on the Langmuir trough and a droplet is placed at its center. The tension exerted by the droplet depends on the thickness of the membrane and surface tension of the cast droplet[32]. The size of the droplet does not alter the centric force exerted on a membrane of particular thickness, as long as droplet volume is kept small as in our experiments. Therefore, casting variable sizes of water droplets causes a constant magnitude of line tension ($\sigma_{rr}^{-} \sim T_i$) in the material.

In this well-studied platform, we compress perfluorododecanoic acid monolayer around the wrinkled sheet and observe the enlargement of the patterns (Fig. 4.14) using the optical set-up presented in Fig. 2.8. We measure the extent of wrinkles when the surfactant pressure equilibrates at a desired value. Each droplet is kept on the film for less than 2 minutes, before they are wiped away and renewed by a fresh droplet.

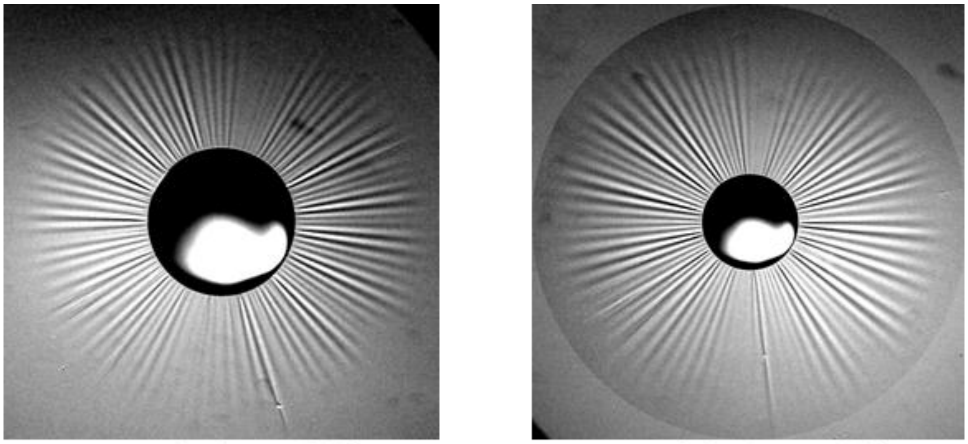

γ_o= 72.8 mN/m γ_o= 48.0 mN/m

Figure 4. 13: A wrinkle pattern around a droplet expands upon depressing the surface tension outside the film. The images belong to a 50 nm PS sheet wrinkled by the identical droplet.

The lengths of wrinkles are measured by inspection (wrinkles longest to the eye on the upper left corner are taken as reference during the image analysis). We plot the results against the reciprocal of the bath surface tension, γ_o^{-1} (Fig. 4.15). The extent of wrinkles increases linearly with decreasing bath surface tension. In FT regime, this observation verifies that T_o is indeed equal to the surface tension of the bath liquid (see eq. 4.14). In addition, the data indicates that the solid surface energies do not play a significant role in keeping the film taut at the interface. This is not a crude assumption if one considers negligible change in the area of a floating solid, in comparison to the large displacements engaged with the fluidity of the bath molecules. Consequently, the Gibbs free energy, G, of spreading ($\partial G = \Sigma\gamma_n\partial A_n$, where subscript n symbolizes each phases) is dominated by the large energy term associated with liquid phase in the system (*i.e.* $\gamma_{liquid}\partial A_{liquid} >> \gamma_{solid}\partial A_{solid}$).

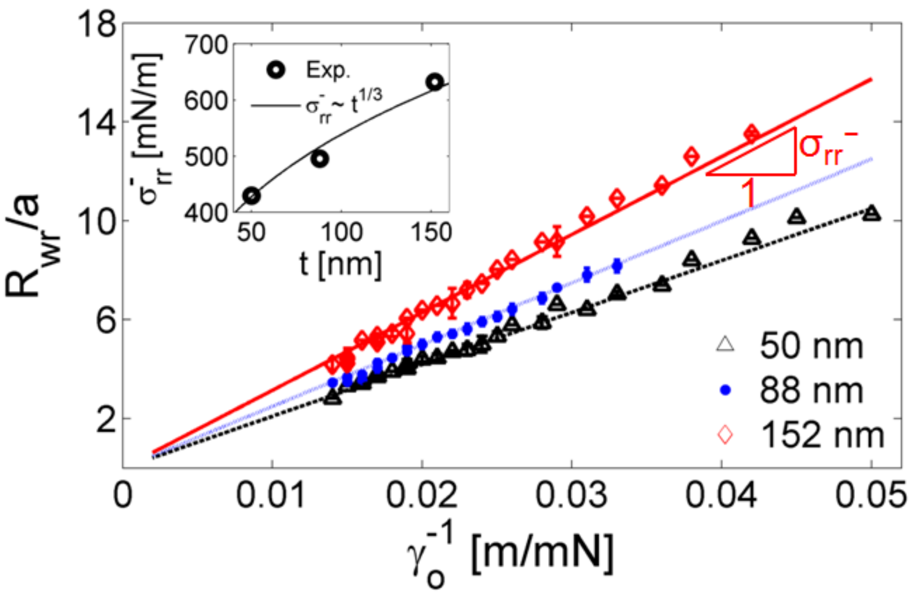

Figure 4. 14: Extent of wrinkles increases as a function of the decreasing bath surface tension γ_o. The trend is linear and indicative of FT regime. (inset) Behavior of σ_{rr}^- calculated from the slopes of the fitted lines also agrees with FT predictions ($\sigma_{rr}^- \sim t^{1/3}$).

4.4.5 Wrinkle wavelength

While length of wrinkles has been extensively studied, the behavior of wrinkle wavelength in FT regime remains relatively unclear. In the first published study on the drop-on-a-sheet experiment some successful empirical arguments on the number of wrinkles were developed. So far, these arguments have remained as the major guideline to predict the wavelength of the patterns forming under an axisymmetric tension gradient. In this section, we show that, in FT regime, the wrinkle wavelength is not only dictated by the properties of the sheet, but also by the boundary conditions.

We characterize the wrinkle wavelength, λ, on an annulus by measuring the average separation angle, $<\lambda>/r$, between neighboring undulations. The details of the measurement methods were discussed in an earlier section. The number of wrinkles, *N*, around a symmetric pattern is related to the angle of separation by the following simple relation, $\lambda / r = 2\pi/N$. In this thesis, we have preferred plotting the data in separation angle format as in Fig. 4.16.

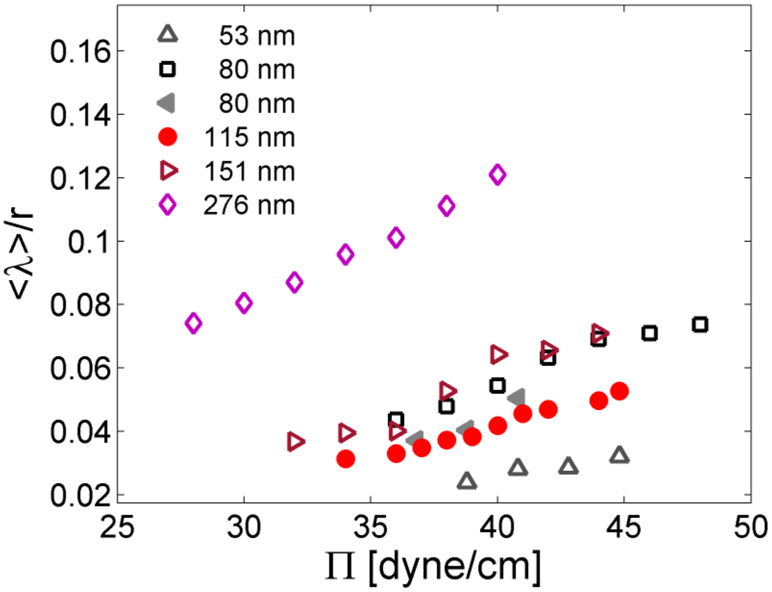

Figure 4. 15: Average angle of separation between wrinkles as a function of surfactant pressure. Red and grey scale data differs in design.

The data initially looks scattered, but can be scaled to reduce the effect of thickness and the size of the inner circle on the wavelength of wrinkles. We would like to implement a scaling relationship presented in Ref. [16] to the annular geometry studied here. First, FvK equation is considered in order to establish the force balance in the normal direction:

$$B\frac{N^4}{r^4}\zeta - \sigma_{\theta\theta}\frac{N^2}{r^2}\zeta + \sigma_{rr}\frac{\partial^2\zeta}{\partial r^2} = 0 \tag{4.22}$$

Since $\sigma_{\theta\theta} << 1$ in the FT regime the second term can be ignored, and the equation can be evaluated for the boundary, where wrinkles are initiated, $r = a$ ($\sigma_{rr}^{-} \rightarrow \gamma_{lv}$). Now we can relate the number of wrinkles to the observable parameters of the problem: $BN^4/a^4 \sim \gamma_{lv}/a^2$. Rearranging this relation, we can capture the combined dependence of λ/r on a and t by the following relation, $\lambda/r \sim a^{-1/2}t^{3/4}$.

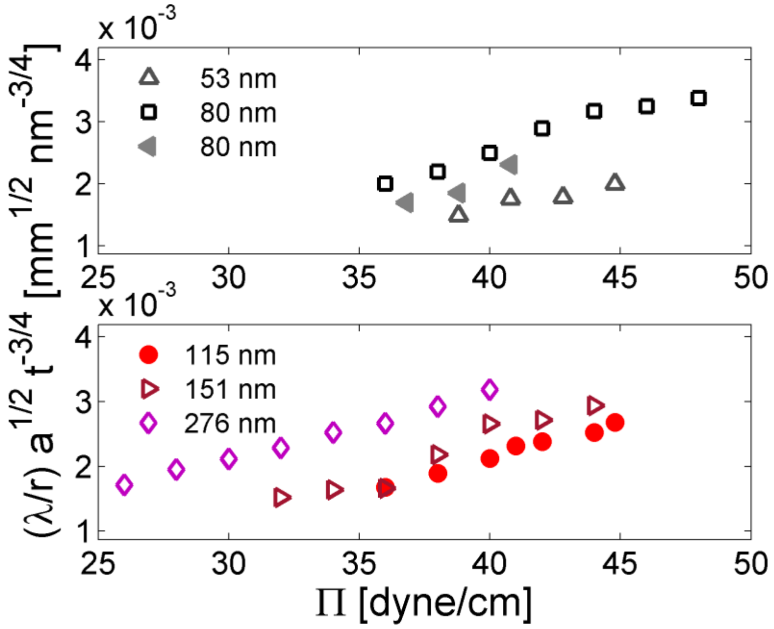

Figure 4. 16: Data presented in Fig. 4.16 is scaled with the arguments developed for the uniaxially stretched rectangle[11]. According to this scaling, the wavelength, λ, of wrinkles is compromised between bending and stretching.

When compared to other possible scenarios (*e.g.* gravity wrinkles, NT scaling etc.), FT scaling provides the best agreement with our data, justifying a general trend up to a certain level.

It is also noticeable that the average wavelength of the pattern has a considerable dependence on the surfactant pressure. One can, again, observe that the data may collapse on a single curve if shifted along the Π-axis. As a matter of fact, an attempt to superimpose the data by applying the original shift factors used for the extents of wrinkles results into a reasonable collapse of the data (Fig. 4.18) on a hypothetically linear function.

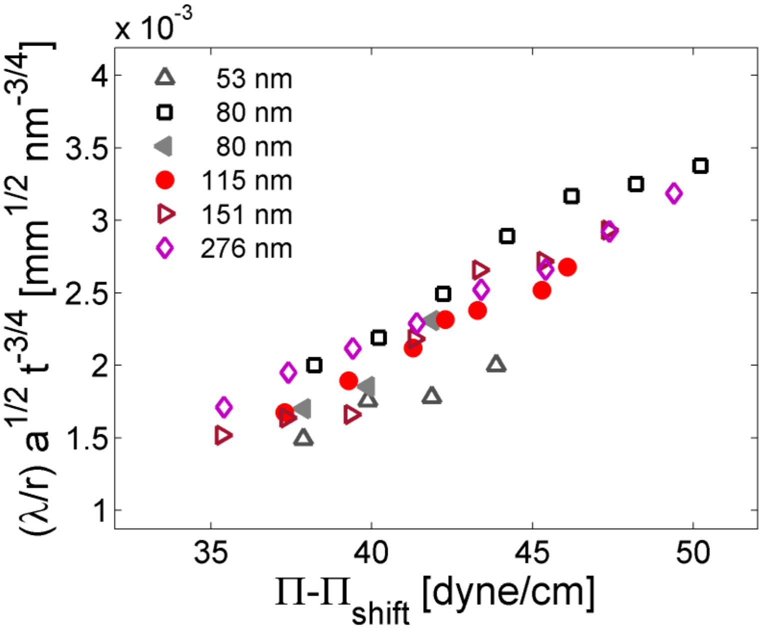

Figure 4. 17: In order to collapse the scaled data presented in Fig. 4.17, a shift is applied along the Π-axis. The shift values are taken from the R_{wr} analysis.

When the wavelength data is rearranged, we choose to be committed to the set of shift values generated from the extent data in R_{wr} vs. Π format; as these scalars provided the smallest R-square value when linearly fitted against $\epsilon^{1/4}$ (see Fig. 4.9).

To sum, the wrinkle wavelength generally depends on the geometry and the properties of the annulus. However, scaling relationships do not solely explain the general behavior. For example, the wrinkle wavelength increases with increasing load-confinement (*i.e.* $N = N(\tau)$); and the state of wrinkles is significantly influenced by the magnitude of the load, τ in reference to the threshold, τ_c of the system. With respect to this observation, we could speculate that two major observables, L and N are related to each other through two dimensionless parameters, *i.e.* bendability and load-confinement; and their scaled values vary in reference to τ_c.

4.4.6 Secondary instability: Fold initiation

Now, we would like to focus on a different phenomenon related to the extent of wrinkles. When all wrinkles in an annulus reach the size of the system, the axial symmetry is attained. Further compression of this highly symmetric state leads to an interesting observation under bright field microscope. First, the contrast of the incident light refracted from the undulations homogenously enhances. This is an indicator of the growth of the wrinkle amplitude over the whole domain of the pattern. When τ reaches a critical value, the deformation starts to be localized at several domains on the surface (*e.g.* $\Pi > 45.2$ mN/m in Fig. 4.19). These domains can be characterized by singularities in the color-contrast that can be easily spotted by naked eye or the two-dimensional micrographs. For illustration, in Fig. 4.19, we present the steps leading to fold initiation on a 151 nm thick PS annulus.

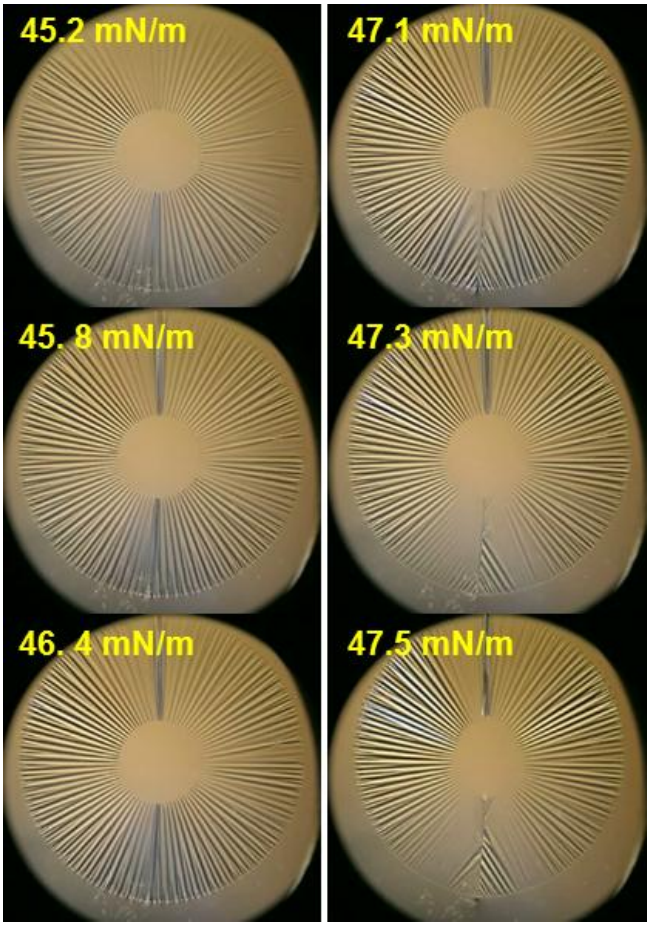

Figure 4. 18: Localization of deformation occurs after wrinkles reach the size of the system. The initiation of a fold on a 151 nm thick PS annulus was detected at $\Pi = 47.5$ mN/m.

The number of localizations per sample varies between 1 and 3. This number does not show any particular dependence on thickness. The stress concentration triggers a new symmetry break in the form of a fold that is initiated in any of these localizations. A fold can be reversed by decompressing the surfactant monolayer around the annulus. We also report on the critical load-confinement values required to initiate folds, measured on the sheets of a range of thickness and aspect-ratios (Fig.4.20).

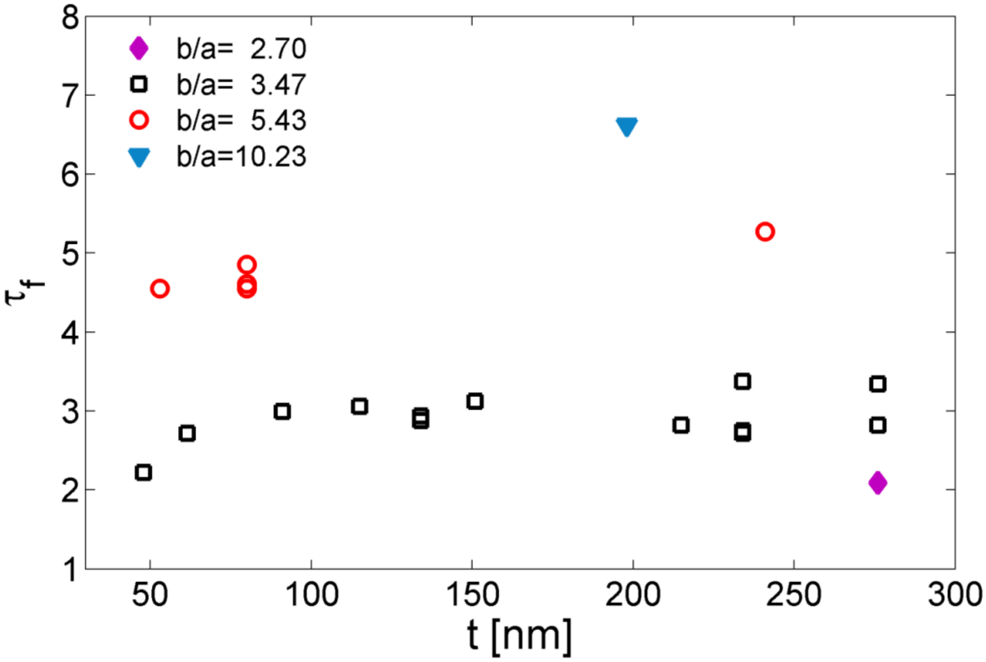

Figure 4. 19: Critical load-confinement detected when the folds are initiated. Folding condition highly depends on the aspect-ratio of the sheets.

The results show that the critical compression required to initiate a fold has a strong dependence on the film geometry, specifically on the annular aspect ratios. The thickness, on the other hand, has a minor effect on the onset of folding. We can confidently conclude that, before it is possible to induce a fold, all wrinkles must extend to the size of the system, and this mechanism is geometrically more difficult for the sheets of higher sizes of the system.

4.5 Conclusion

An annulus offers a purely two-dimensional setting for wrinkle formation. Thin PS annuli floating on water are imposed to axisymmetric tension gradients with the aid of an insoluble surfactant. In this experiment, wrinkling is induced on sheets of varying annular aspect ratios and thicknesses. We study the observable properties like the wavelength and the extent of wrinkles via analyzing two dimensional bright field images. The extent of wrinkles converges to FT predictions for thinner films. On the thicker films, wrinkles are induced earlier and they grow to larger extents during routine compressions. This indicates that, in the studied thickness regime, thicker structures buckle more easily. We have not yet understood the root-cause of this unusual behavior which fundamentally contradicts the general formalism of buckling.

The thickness effect is experimentally isolated from the other geometric constraints, where wrinkle length also depends on the design of the annulus. Empirical arguments successfully cover the individual roles played by geometry, threshold and boundary conditions. The analysis on the wrinkle wavelength also suggests that the properties of wrinkles are governed by the well-studied scaling arguments; and moreover, wrinkles observed on varying thicknesses demonstrate identical states in reference to the boundary conditions they are initiated. This universal equivalence implies that the buckling behavior at one thickness can be related to that at another by a change in the critical load confinement (or surfactant pressure). We also have discovered that the scaled wrinkle lengths (and wavelengths) at two different thicknesses can be superimposed exactly by a horizontal displacement $\Delta\tau$ (or $\Delta\Pi$), which can be defined as a physical shift factor. The shift factor enables us to trivially quantify the threshold conditions.

We have closed this chapter presenting a secondary instability observed on the specimens, which occurs in the form of folding. We have found that the annular aspect-ratio of the film has a strong influence on fold initiation over a broad range of thickness.

CHAPTER 5

RELAXATION OF WRINKLES

In this chapter, we study the relaxation of wrinkling patterns formed around droplets. The viscoelastic character is introduced to the sheets by reducing the glass transition temperature (T_g) of PS compounded with a plasticizer.

Please note that in this chapter we have made a few changes in symbolic abbreviations such that, unlike former chapters t stands for time and δ is thickness; T symbolizes temperature and τ symbolizes the relaxation time.

5.1 Background

Polymeric films are inexpensive and easy to process; hence, they are used in numerous engineering applications such as electronics, packaging, protective coatings, energy harvesting, and optical barriers. There has been many studies in the literature showing that the properties measured[69] on bulk material does not explain the physical behavior observed in polymeric coatings or thin layers[70]. Especially dynamics of polymers become anomalous in the glass transition regime, when the macromolecules are confined[47-49, 51, 71] into thicknesses comparable to their unperturbed radius of gyration (R_g). Since glassy state comprises highly metastable vitrified molecules[39, 44, 72], the relaxation of observables does not necessarily imitate the bulk behavior either. This may cause challenges in predicting the physical state and the longevity of the substance.

The anomaly in film dynamics have also been attributed to the energetic interactions between the polymer and neighboring layers[52, 53, 73]. On a typical coating, the free surface has been thought to be the major contributor of the enhanced mobility of the chains closer to the surface, which might lead to faster dynamics (reduced T_g) observed in the material. This hypothesis has been evaluated on different material systems via modification of the polymers or the surfaces[74-80]. Overall, strength of the interaction between the surface and the polymer determines the deviated nature of the trend observed in glass transition as a function of the varying thickness[81, 82].

A range of techniques provide useful information on dynamics of thin polymeric layers. The most common one is the measurement of thickness δ as a function of the film temperature (T)[51, 73, 77]. In this method, T_g is defined as the point where the slope of the δ-T curve alters. Thickness measurement ideally reflects the density change in the material provided that the lateral dimensions remain constant, or change similarly as the thickness. There have been alternative volumetric measurements analyzing the areal shrinkage of a film freely floating on an annealed bath liquid[78-80]. In this approach, slow rate extensional viscosity is calculated in reference to the constant spreading coefficient contracting the material. (Revisiting Section 4.4.4: On a softened polymeric layer floating on a liquid, spreading coefficient can be written as $S = \gamma_{lv} - (\gamma_{sv} + \gamma_{sl})$, since all the areal terms in Gibbs free energy of the system are equal to each other, $A_{lv} \approx A_{sv} = A_{sl}$).

Characterization of the film dynamics is not limited with the volumetric measurements. Irradiative methods like X-ray reflectivity[74, 75, 77], fluorescent dye detection[76], Brillouin light scattering[52, 53] also investigate the motion and dynamic state of the film and the interfaces. Moreover, the slow rate extensional viscosity of a dewetting layer can be quantified with respect to the rate of a defect (*a.k.a*. hole) expansion [72, 83, 84]. This method is relatively time consuming since the nucleation and propagation of the microscopic holes are usually inspected by atomic force microscope. Another alternative method that can probe the same property, known as bubble inflation technique[81, 82, 85, 86], also requires elaborate sample preparation and instrumentation.

In this chapter we introduce a simple and robust technique to measure the slow strain rate viscoelastic characteristics of thin polymeric layers. The measurement relies on *in-situ* inspection of dynamic wrinkling patterns generated on floating ultrathin (δ< 300 nm) polymeric specimens. Formation and characterization of wrinkles are practically simple. The films are solvent cast on smooth substrates, floated on water, transferred to a liquid bath of preference, and wrinkled by placing a ~1 µL droplet (bubble) at the center. The dynamic behavior of the pattern can be monitored and recorded by a stereomicroscope-camera system. The relaxation of wrinkle length is related to the stress and strain relaxation that occurs under the droplet. Overall, this technique is capable of studying the slow rheological response of a variety of polymers at a variety of interfaces and under controllable physical conditions.

5.2 Experimental details

5.2.1 Thin film protocols

In order to understand the basics of the problem, we focus our initial efforts on the materials that were previously used in the original droplet experiment [16, 31]. We prepare blends of atactic polystyrene (Polymer Source, M_n=99kg/mol, PDI=1.06; M_n=885kg/mol, PDI=1.08; M_n=6,000kg/mol, PDI=1.22) with a common plasticizer (Dioctyl Phthalate from Sigma Aldrich ≥99.5%). We name each sample by the molecular weight of PS and the mass ratio of the plasticizer (DOP) per every 100 grams of the polymer. A variety of plasticizer compositions are prepared (30:100, 32:100 and 34:100) in order to depress the glass transition of the film close to the room temperature.

DOP and PS are mixed in Toluene for preparing the film-casting solution. We label the solvent content of a sample in reference to the total mass of PS added into the vial. If a solution is labeled as “30:100 DOP:PS with 1.6% PS/solution”, then the following mass ratios of the ingredients must be expected: 100 unit solvent, 1.60 unit PS and 0.48 (1.60x30/100) unit DOP. We specify this information in order to clarify some details for the future experimentalist who plans to repeat our measurements.

Pertaining the details of the mixing protocol, we recommend pouring an aimed amount of plasticizer into a vial that already contains a known quantity of the polymer. Due to its high intrinsic viscosity, it is more precise to transfer desirable amounts of DOP after blending with a Toluene/THF co-solvent (80/20 mass ratios). We also recommend using DOP solution only when it is still fresh, as THF and toluene may evaporate during long intervals of storage in the vial. Deviations in the known concentration of DOP solution can create an uncertainty on the quantity transferred into the polymer-plasticizer mixture. This could be a significant source of error if not practiced suggestively.

We avoid filtering the solutions prior to spin-casting on clean microscope slides. The freshly coated glass slide is scribed by a sharp tip utensil; and a disc is floated on water. The freely floating disc is easily caught with a small (2” wide) petri dish (made out of PS) where experiments are carried out at room temperature. In our measurements, the bath (supplied from in-house RO water system) temperature is consistently measured as

20^{o}C by a thermometer. This value is close to the T measured for air conditioned ambient lab environment, 19–21 ^{o}C. We also check that the low-power halogen microscope lamp (a potential source of heat) is isolated from the stage and the sample, and does not create thermal noise during the measurements. The humidity of air in the lab demonstrates a large variation day by day, probably depending on the outside conditions. The relative humidity values are reported within 30–60% range during the experiments.

The aging of specimens immediately starts after coating and continues until the floating and the wrinkling experiment, which approximately takes 10 minutes in total. When the sample is kept aging (on glass substrate) in lab conditions for an additional hour after coating, the measured viscoelastic response of the specimens does not change within error. We also have not observed a significant (rapid) change in the film thickness on water, unless the sample is left to relax freely for multiple hours. Free relaxation at room temperature (for the set of samples presented here) is slow enough to be neglected. The dynamic response of the material is generally scattered, which requires an experimenter to run several trials (3–7 unique runs) on each category of samples.

5.2.2 Bulk protocols

In order to understand the plasticizing effect of DOP on PS, we run several tests on solvent-cast bulk samples. Due to the limited amount of lab grade low-dispersity PS, we use commercial grade PS pellets. GPC analysis on pellets dissolved in THF shows that both number and weight averaged molecular weights are above the critical entanglement molecular weight of the polymer[46] (M_n=95kg/mol, M_w=240kg/mol, PDI=2.53). Since majority of the bulk properties (except viscosity) remain constant beyond the critical entanglement, we can cast thick films from this material that can demonstrate typical bulk behavior.

Before casting thicker films, we blend the material with a protocol identical to the one described in the previous section. This time we scale up the volume and switch to a larger container that can fit 20 gram PS and ~100 gram solvent. The solutions are mixed with a magnetic stirrer overnight. No filtering is applied. We place ¼ inch thick, 6 cm tall and 4 cm wide Teflon pieces on a flat metal container to cover all the area on the metal. After ensuring that the surface is flat, we pour the solution up to the brim of the container (Fig. 5.1 (2)). The cast solution is kept in the hood for two or three days until the solvent dries out from the sample. Dried film can be easily peeled off from the Teflon surface (Fig. 5.1 (3-4)). We use this film to cut small rectangular samples for Dynamic Mechanical Analysis (DMA) characterization (Fig. 5.1 (5-6)).

We perform bulk stress relaxation experiments with a DMA Q800 model Dynamic Mechanic Analyzer from TA Instruments. Typical specimens are 3 cm tall and 0.6 cm wide rectangles; their thicknesses vary between 85 and 170 µm. Cutting a perfect rectangle is crucial because the sample stands on its short edge during the alignment. After clamping the film, we get rid of any slack in the material by releasing the free end of the mount holding the sample (Fig. 5.1 (7)). One can monitor from the DMA software that sample starts to creep slowly over the weight of the freed component. We stop the creep by locking the position of the mount, which is followed by immediate inception of the experiment. The temperature controlled chamber quickly closes and a step strain of 0.3% is uniaxially applied on the sample. The temperature of the chamber is maintained at 20^{o}C while the relaxation of the stress is monitored and recorded.

We also measure the bulk T_g using a DSC 2910 Dynamic Scanning Calorimeter from TA Instruments. Samples are cast from identical solutions into aluminum pans purchased from TA Instruments (T 120430 Hermetic Lid). Upon drying the cast solution, ~5 milligrams of PS:DOP composite is coated on the walls of the pan. Several independent measurements are performed at 10 ^{o}C/min rate. The glass transition is searched on the heating trace, as the set-up has better control on heating than cooling.

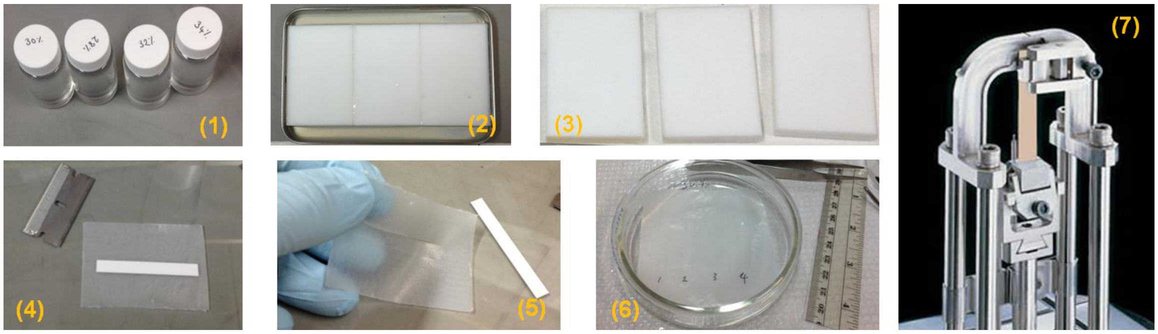

Figure 5. 1: Steps taken in DMA Characterization: From (1) solution preparation to (7) the actual testing of the rectangular samples.

5.3 Results and Discussion

5.3.1 Bulk rheology

In Fig. 5.2 we summarize the results of the DSC analysis. Since T_g is a colligative property, we do not expect the outcome of this analysis to vary for samples of another degree of polymerization (as long as the polymers remain in the entanglement regime). Hence, the results can be considered as a general recipe to understand the plasticizing effect of DOP on bulk (linear atactic) material. The measured values do not necessarily represent the actual values for the film, but we may anticipate that our routine experiments at room temperature investigate the material behavior in the interesting glass transition regime.

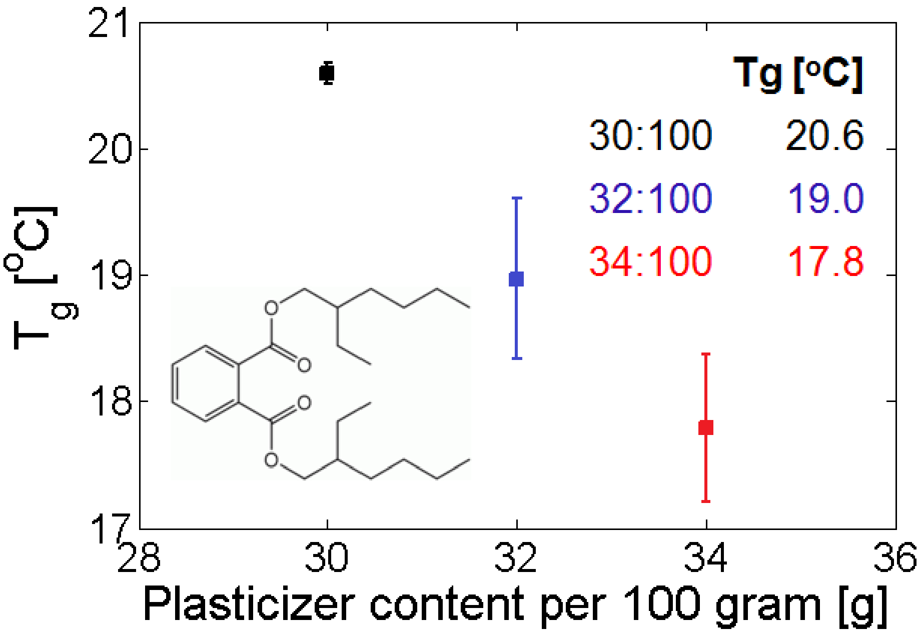

Figure 5. 2: Bulk T_g measured for variable content of DOP blended with 100 gram of PS. The results are averages from the DSC traces measured at 10 °C/min rate of heating. Inset shows the chemical structure of the plasticizer.

The DMA results presented in Fig. 5.3 are coherent with the DSC analysis; such that, as molecules experience the glass transition, a slight change in temperature causes large variations in physical properties. The rheology of the bulk samples, here, demonstrates that 1 or 2 °C change in T_g creates significant difference in the room T dynamics. This effect is pronounced more clearly when the data is fit to a KWW type[87, 88] stretch exponential function, *i.e.* $\sigma/\sigma_0 = \exp(-(t/\tau)^{\beta})$, where β is defined as the stretch exponent. We observe a systematic (two to four folds) increment in the relaxation times as plasticizer content decreases. More specifically, small reduction in T_g prominently (by several folds) accelerates the stress relaxation.

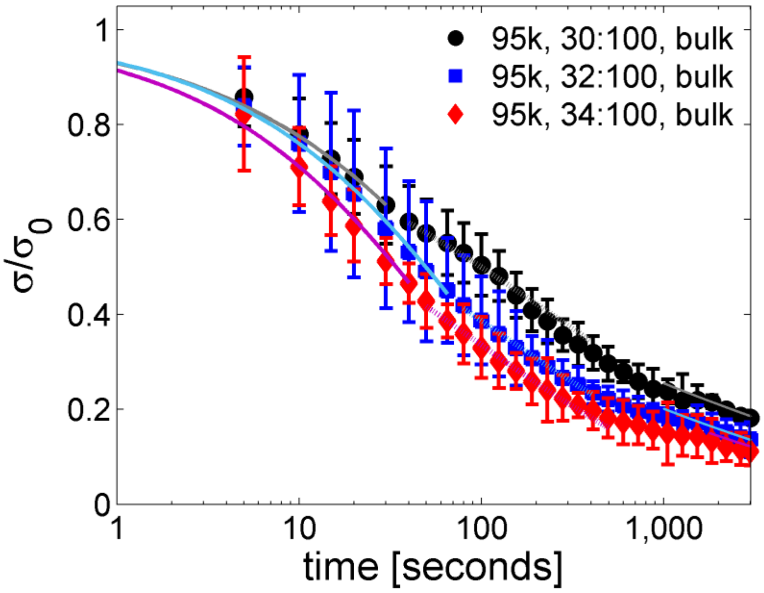

Figure 5. 3: Stress relaxation curves of the solvent cast samples in bulk. A small change in DOP content results into an evident change in the relaxation behavior. In this graph, three general intervals of relaxation are observed which can be labeled as *inception* (1<t<40 sec), *intermediate* (~50<t<400 sec) and *final* (t>1000 sec) periods.

5.3.2 Wrinkle relaxation

In this section, we provide some experimental evidences that ascertain interesting correlations between the wrinkle relaxation and the film rheology. In this study, we merely focus on the wrinkle length as it provides an indirect measure of the stress and strain generated under the droplet[32, 60]. There are two major excuses that justify our reluctance on an elaborate *in-situ* number (wavelength) analysis. First, wrinkle wavelength experiences discrete changes in time, while the length relaxes continuously in the experiment (L might only slow down very briefly when wavelength of the pattern is rearranged during relaxations). Second, we do not have a simple expression that establishes an analytical relationship between the wavelength of wrinkles and the kinematics of the material.

In our systematic studies, we first pay attention to the relaxation of wrinkles as a function of the plasticizer content. In order to address this effect, we study the pattern dynamics on 116 nm thick PS99k ($2R_g$~12 nm) films with DOP compositions identical to the bulk specimens. Fig.5.4 demonstrates that dynamics of wrinkles are quite sensitive to the small changes in the amount of plasticizer present in the film. However, we still observe large error bars that may indicate a large variance in the data due to the fast dependence of parameters on T in the glass transition regime probed by the experiment.

We also find that the stretch exponents retrieved from wrinkle relaxation agrees decently with the fit parameters measured for the bulk relaxation (See Table 5.1 at the end of this chapter for a complete list of measured parameters). We make a comprehensive comparison studying the three relaxation modes observed in the bulk and the thin film. We classify each interval as *inception*, *intermediate* and *final*, with respect to the order of occurrence. Only first two of the three modes are fully captured by the wrinkling experiments. Unfortunately, we cease measuring the wrinkle length after 400 seconds due to the fact that, in several occasions, the water droplets start to shrink rapidly beyond the *intermediate* interval. Those data are not included in this thesis.

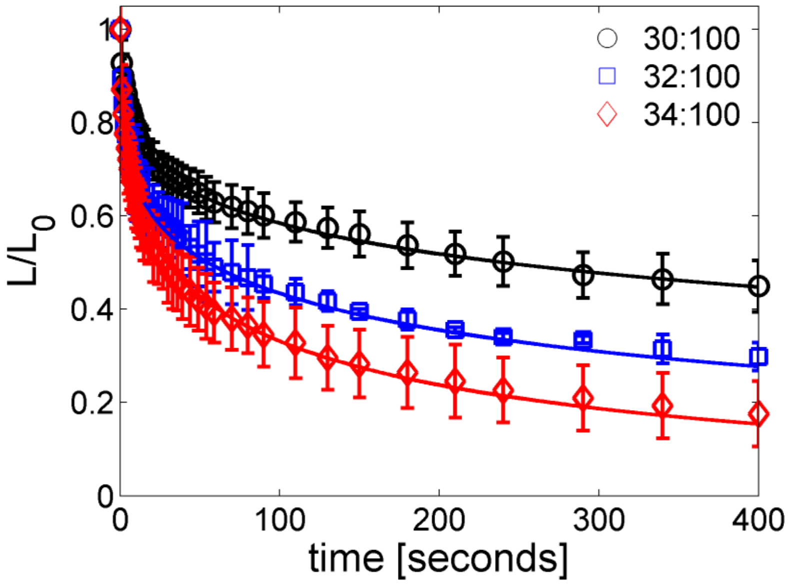

Figure 5. 4: Relaxation of wrinkles on identical samples (PS99k, 116 nm) with varying DOP content. Decay in the length is observed faster with increasing plasticizer. The solid lines are the best fit to the portion of the data in the *intermediate* interval.

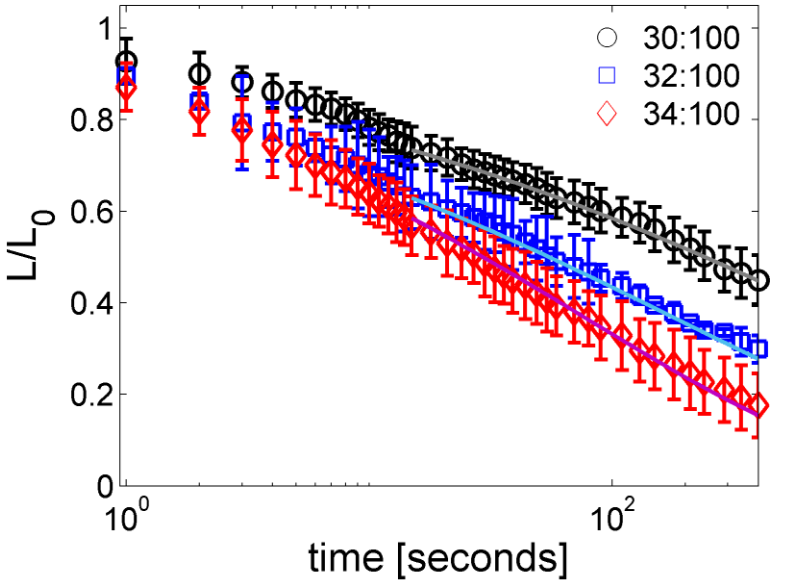

Figure 5. 5: Data from Fig. 5.4. is re-plotted in log-scale. This version enables us to distinguish the relaxation modes during the *inception* (0<t<15 sec) and the *intermediate* (18<t<400 sec) intervals.

Please check the figure above providing the log-scale version of the data presented in Fig.5.4. The so-called *inception* and *intermediate* intervals can be more clearly distinguished in log-scale.

In order to understand the role of thickness on wrinkle relaxation, we have studied 30:100 PS99k samples spun to a range of thicknesses. As we try to evaluate the sole influence of thickness on the relaxation, we need to primarily capture the confinement ($\delta/2R_g$) effect on the dynamics. The data presented in Fig. 5.6. belongs to a regime of moderate molecular confinement, as $\delta/2R_g$ varies between mediocre values, 5.8 and 25. We cannot provide a solid conclusion whether the variation in dynamics is related to the factors such as a deviation in free volume, a possibly emphasized role of interfacial interactions, or macromolecular confinement. Nevertheless, Fig. 5.6 demonstrates a slight dependence of the dynamics on the thickness.

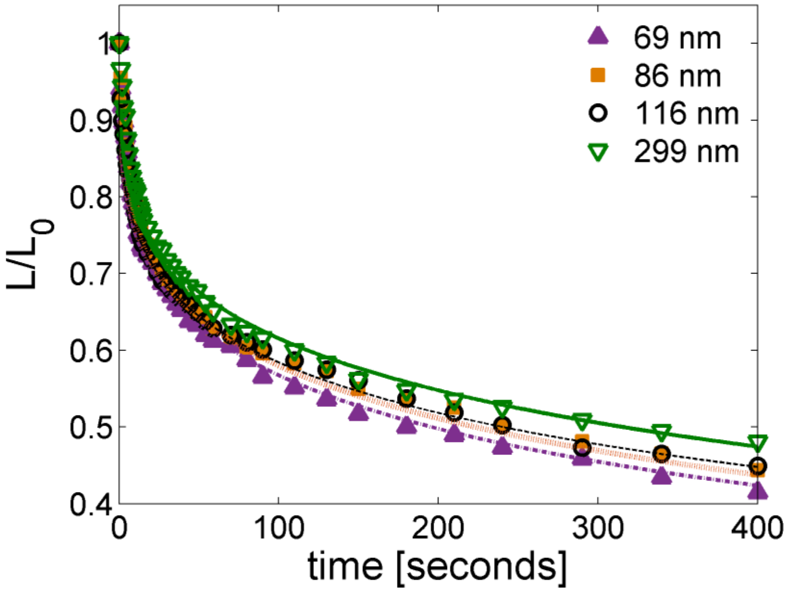

Figure 5. 6: The role of thickness on 30:100 PS99k films. We observe a slight change in relaxation dynamics due to a large change in thickness.

Molecular weight is a useful control parameter that can arrest the role of molecular confinement on relaxation. To address this hypothesis, we perform the relaxation experiments on 116 nm films (30:100 blends) spun from different molecular weight polymers. The materials used in this experiment, PS99k, PS885k and PS6000k, offer a broad range of melt radius of gyrations, 6, 18 and 47 nm respectively. Such variation at R_g corresponds to a broad spectrum of confinement, quantified by respective $\delta/2R_g$ values, 10, 3, and ~1. The Fig. 5.7 below presents the relaxation of wrinkles observed on these samples of varying molecular weights. We observe a reasonably strong influence of confinement on the relaxation.

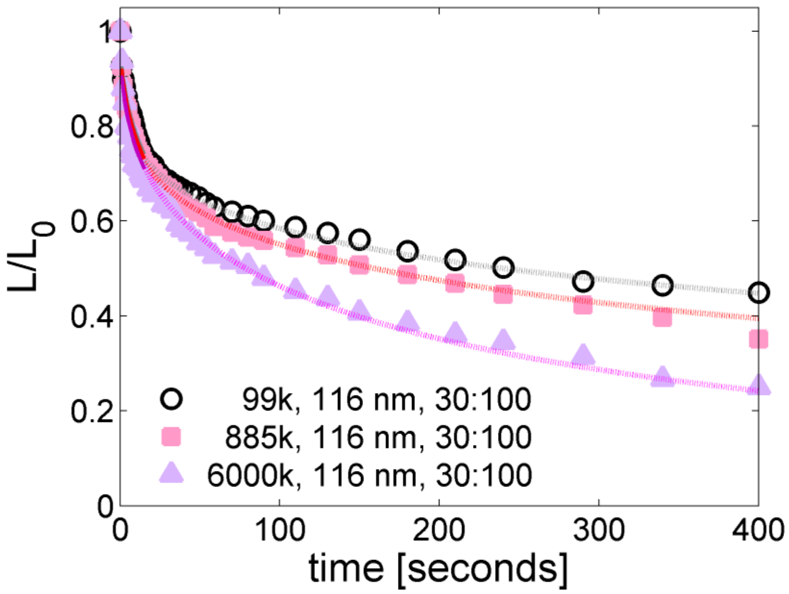

Figure 5. 7: Relaxation on 116 nm 30:100 plasticized film is faster when molecular weight of PS is increased. Solid lines are again best fit to the *intermediate* relaxation interval.

Data presented in Fig. 5.7 demonstrates a significant contradiction with some well-established empirical arguments. Here, we observe a faster relaxation on a significantly higher molecular weight PS film, which contradicts with the Mark-Houwink exponents universally formalized for the polymer flow. More specifically, bulk viscosity, η, without any exceptions, must scale strongly with the size of the entangled polymers of linear architecture, $\eta \sim M_n^{3.4}$. Our data shows an opposite trend where relaxation is observed faster at higher molecular weight polymers. To summarize the results discussed so far, we have prepared a matrix of the stretch exponents and relaxation times extracted from individual measurements:

Table 5. 1: Fit values are tabulated for all experiments. Subscript 1, 2 and 3 represent *inception*, *intermediate* and *final* relaxation intervals respectively. The stretch exponent is approximately 0.5 during *inception*, 0.3 in the *intermediate* and, 0.2 in the *final* phase. *Inception* in the bulk takes at least twice as long time as in the thin film samples.

M_n [kg/mol]	PDI	DOP:PS	δ [nm]	β_1	τ_1 [sec]	β_2	τ_2 [sec]	β_3	τ_3 [sec]
99	1.06	30:100	69	0.58	109	0.30	664	N/A	
99	1.06	30:100	86	0.65	120	0.30	757		
99	1.06	30:100	116	0.50	167	0.29	851		
99	1.06	30:100	299	0.60	188	0.31	1029		
99	1.06	30:100	116	0.50	167	0.29	851	N/A	
99	1.06	32:100	116	0.55	58	0.31	179		
99	1.06	34:100	116	0.53	45	0.38	77		
99	1.06	30:100	116	0.50	167	0.29	851	N/A	
885	1.08	30:100	116	0.49	161	0.32	502		
6000	1.22	30:100	116	0.46	156	0.44	181		
95	2.54	30:100	bulk	0.54	126	0.31	324	0.19	194
95	2.54	32:100	bulk	0.58	93	0.31	118	0.20	95
95	2.54	34:100	bulk	0.58	64	0.32	76	0.20	73

5.3.3 Relaxation under the droplet

In this section, we would like to present an in-situ topographical measurement of a blister bulging above an air bubble, which is in static contact with a lightly plasticized PS film floating on glycerol. Optical profilometry is preferred in this task due to its high resolution and short (~1-2 sec) scan intervals. In Fig. 5.8, a mutual trend is traced by the scaled bulge height and length of wrinkles as a function of the time of relaxation. This behavior has been expected since the studies on elastic PS films[31, 32] have shown that the wrinkle length linearly scales with the height of the bulge forming under the droplets ($L \sim h$). In another experiment, we have verified this topographical change when the water droplets are wiped off after the relaxation. One finds that the blister remains slacked and permanently deformed where the droplet is located. Overall, the relaxation of wrinkles turns out to be a fundamental result of the kinematic change under the droplet.

In the lightly plasticized film, we also investigate the consequences of wrinkle relaxation in the close vicinity of the droplet (bubbles), where the radial stress is expected to be the highest. After the wrinkle relaxes to approximately 60% of its original length, we collect the specimen with a smooth glass slide, and re-float it on water. We ensure that the residual glycerol is cleaned off from the underlying surface by re-transferring the film to several other clean baths of water. Eventually, we catch the film with a clean Silicon wafer and dry it under Nitrogen. We measure the thickness around the footprint of the bubble (droplet) with the interferometer and find a minor reduction (~1%) from the initial thickness within error. In this measurement, we demonstrate that the change in film thickness is insignificant in comparison to the dramatic change in the blister height and the length of wrinkles.

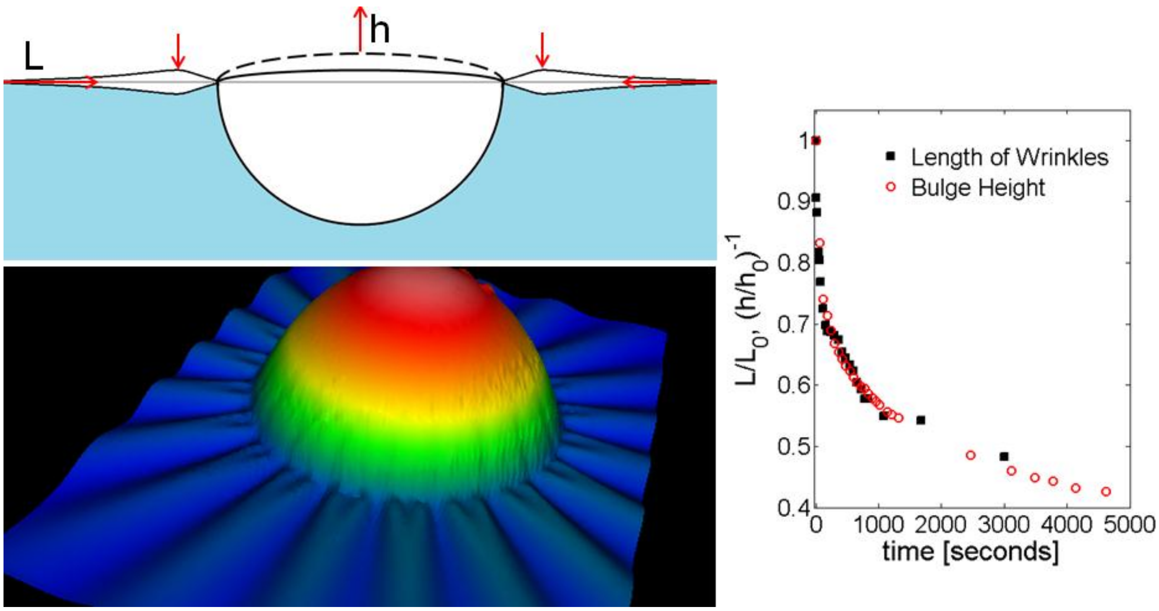

Figure 5. 8: 228 nm lightly plasticized PS film on a glycerol bath. Scaled wrinkle length traces the same trend as the scaled bulge height, h/h_0 under the bubble (droplet). This evidence proves that the wrinkle relaxation is related to the capillary mechanics under the droplet.

5.4 Conclusion and future work

Our new platform can measure the small rate viscoelastic response of ultrathin polymeric sheets freed from the constraints of a pinning substrate layer. This simple method offers a tremendous potential to probe the dynamics of very thin sheets as a function of surface interactions and confinement. In future, this platform can be used in viscoelastic testing of polymers of different structure and architecture, while imposing the films to different chemistries and surface tensions at the interfaces.

So far, in order to simplify our analysis, we have kept working with water as the probe liquid (both using as the bath and the droplet), which, disadvantageously, offer a relatively low boiling point and high vapor pressure. However, water has an almost neutral affinity between air and PS, and vast amount of our knowledge accumulated on elastocapillary wrinkling has been on our work with water. For future studies, we recommend ionic liquids[89] being useful candidates to facilitate free annealing of the polymeric materials[77] and wrinkle relaxation. Despite being hygroscopic, the properties of an ionic liquid can be kept unchanged after quenching the liquid with sufficient uptake of water. Using this simple approach, one can standardize a simple protocol for relaxation measurements in the ambient or controlled environments.

We would also like to add a list of duties that can support some of the ideas and questions raised in this chapter. First, in order to understand the role of confinement, one should study how wrinkle dynamics change after viscoelastic films freely relax (age) on water. This experiment should address questions regarding the orientation of the film. One could also study other non-linear phenomenon such as aging of polymers using identical films controllably stored (*e.g.* at $T<T_g$) on solid substrates prior to relaxation. Our effort on aging is limited to some studies (Fig. 5.9 and 5.10) on non-plasticized glassy PS aged in ambient conditions for a year.

In order to understand and quantify the chain orientation in solvent processed films, a waveguide[90-94] could facilitate in-plane and out-of-plane birefringence measurements. One could relate the relaxed and unrelaxed chain orientation in the film to a variety of viscoelastic measurements available, including the wrinkle relaxations and free relaxation on a liquid.

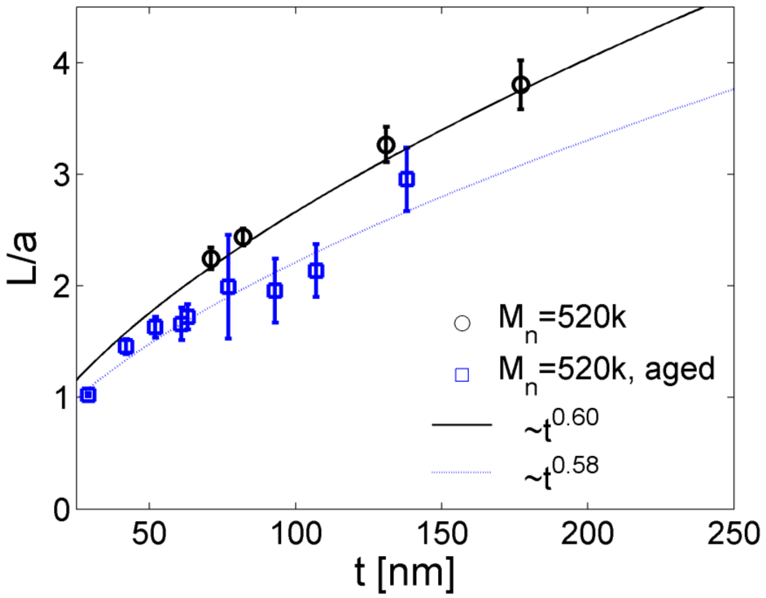

Figure 5. 9: Comparing the wrinkle lengths measured on aged (1 year in ambient T) and fresh PS520k.

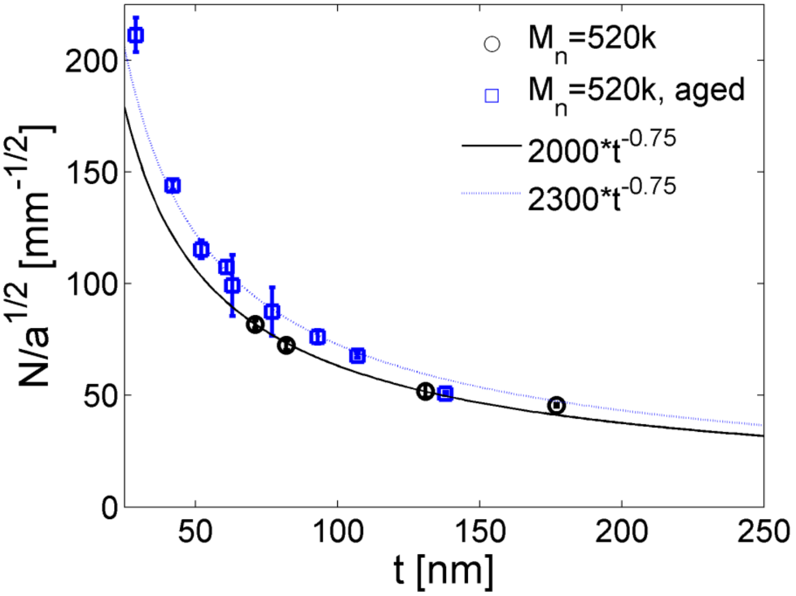

Figure 5. 10: Comparing the wrinkle number measured on aged (1 year in ambient T) and fresh PS520k.

Finally, a comprehensive bubble inflation model[55, 81, 82, 85, 86, 95-99] should be implemented to this new platform, so that one can use simple formalisms to interpret and translate the extent of wrinkles as the strain and stress under the droplet. The current models used in the literature assume a biaxial stress in every point around the droplet, which is merely valid for the very center of the blister.

CHAPTER 6

CONCLUSIONS

In this dissertation, we study the axisymmetric wrinkling of ultrathin polymer sheets floating on water. Supported by a liquid bath, the films are kept flat and taut on the surface by capillary forces. The wrinkles are generally induced by imposing a tension gradient from the center. In the first experiment, we place a droplet (or bubble) at the center of the film and characterize the wrinkle pattern around the droplet. We use three dimensional imaging techniques to study the topography of the problem. Overall, the elasto-capillary effect of a liquid droplet on a highly deformable floating layer is understood better. With our results, the droplet experiment is closer to being a wrinkling based mechanical and interfacial characterization technique applicable to soft materials.

In another experiment, we facilitate wrinkling by inducing a tension gradient between the two peripheral boundaries of an annulus. This is achieved by compressing a surfactant monolayer outside the floating material. In this relatively simpler geometry, we study the role of bendability on the extent of wrinkles. We measure the wrinkling threshold, which is found to demonstrate unusual thickness dependence. We confirm that the wrinkling patterns obey the scaling laws that accurately predict the character of the deformation; however, the scaled properties of wrinkling are highly influenced by the relative differences between the conditions dictated by the boundaries and the buckling threshold of the system. This conclusion is supported by our analyses performed on both the wavelength and the length of wrinkles. Our set-up also shows that fold initiation on axisymmetric wrinkles is mostly dictated by the geometric constraints in studied regime.

BIBLIOGRAPHY

1. Whitesides, G.M., et al., *Spontaneous formation of ordered structures in thin films of metals supported on an elastomeric polymer.* Nature, 1998. **393**(6681): p. 146-149.
2. Pocivavsek, L., et al., *Stress and fold localization in thin elastic membranes.* Science, 2008. **320**(5878): p. 912-6.
3. Gompper, G., *Patterns of stress in crumpled sheets.* Nature, 1997. **386**(6624): p. 439-441.
4. Kramer, E.M. and T.A. Witten, *Stress condensation in crushed elastic manifolds.* Physical Review Letters, 1997. **78**(7): p. 1303-1306.
5. Harrison, C., et al., *Sinusoidal phase grating created by a tunably buckled surface.* Applied Physics Letters, 2004. **85**(18): p. 4016.
6. Chan, E.P., et al., *Surface Wrinkles for Smart Adhesion.* Advanced Materials, 2008. **20**(4): p. 711-716.
7. Singamaneni, S. and V.V. Tsukruk, *Buckling instabilities in periodic composite polymeric materials.* Soft Matter, 2010. **6**(22): p. 5681.
8. Schweikart, A., et al., *Controlling inter-nanoparticle coupling by wrinkle-assisted assembly.* Soft Matter, 2011. **7**(9): p. 4093.
9. Harris, A., P. Wild, and D. Stopak, *Silicone rubber substrata: a new wrinkle in the study of cell locomotion.* Science, 1980. **208**(4440): p. 177-179.
10. Burton, K. and D.L. Taylor, *Traction forces of cytokinesis measured with optically modified elastic substrata.* Nature, 1997. **385**(6615): p. 450-4.
11. Cerda, E. and L. Mahadevan, *Geometry and Physics of Wrinkling.* Physical Review Letters, 2003. **90**(7).
12. Cross, M. and P. Hohenberg, *Pattern formation outside of equilibrium.* Reviews of Modern Physics, 1993. **65**(3): p. 851-1112.
13. Huang, J., et al., *Smooth Cascade of Wrinkles at the Edge of a Floating Elastic Film.* Physical Review Letters, 2010. **105**(3).
14. Rogers, J.A., T. Someya, and Y. Huang, *Materials and mechanics for stretchable electronics.* Science, 2010. **327**(5973): p. 1603-1607.

15. Cavallo, F. and M.G. Lagally, *Semiconductors turn soft: inorganic nanomembranes.* Soft Matter, 2010. **6**(3): p. 439.

16. Huang, J., et al., *Capillary wrinkling of floating thin polymer films.* Science, 2007. **317**(5838): p. 650-3.

17. King, H., et al., *Elastic sheet on a liquid drop reveals wrinkling and crumpling as distinct symmetry-breaking instabilities.* Proc Natl Acad Sci U S A, 2012. **109**(25): p. 9716-20.

18. Steigmann, D.J., *Tension-Field Theory.* Proceedings of the Royal Society of London. Series A, Mathematical and Physical Sciences 1990. **429**(1876): p. 141-173.

19. Chung, J.Y., A.J. Nolte, and C.M. Stafford, *Diffusion-Controlled, Self-Organized Growth of Symmetric Wrinkling Patterns.* Advanced Materials, 2009. **21**(13): p. 1358-1362.

20. Breid, D. and A.J. Crosby, *Effect of stress state on wrinkle morphology.* Soft Matter, 2011. **7**(9): p. 4490.

21. Srinivasan, K., et al., *Thermally induced wrinkling in thin-film stacks on patterned substrates.* IBM Journal of Research and Development, 2009. **53**(3): p. 12:1-12:10.

22. Moon, M.-W., et al., *Controlled formation of nanoscale wrinkling patterns on polymers using focused ion beam.* Scripta Materialia, 2007. **57**(8): p. 747-750.

23. Dufresne, E.R., et al., *Dynamics of fracture in drying suspensions.* Langmuir, 2006. **22**(17): p. 7144-7.

24. Toga, K. and B. Alaca, *Junction formation during desiccation cracking.* Physical Review E, 2006. **74**(2).

25. Xu, Y., et al., *Imaging stress and strain in the fracture of drying colloidal films.* Soft Matter, 2013. **9**(14): p. 3735.

26. Vermorel, R., N. Vandenberghe, and E. Villermaux, *Impacts on thin elastic sheets.* Proceedings of the Royal Society A: Mathematical, Physical and Engineering Sciences, 2009. **465**(2103): p. 823-842.

27. Chopin, J., D. Vella, and A. Boudaoud, *The liquid blister test.* Proceedings of the Royal Society A: Mathematical, Physical and Engineering Sciences, 2008. **464**(2099): p. 2887-2906.

28. Holmes, D.P. and A.J. Crosby, *Draping Films: A Wrinkle to Fold Transition.* Physical Review Letters, 2010. **105**(3).

29. Vella, D., et al., *Wrinkling of Pressurized Elastic Shells.* Physical Review Letters, 2011. **107**(17).

30. Davidovitch, B., et al., *Prototypical model for tensional wrinkling in thin sheets.* Proc Natl Acad Sci U S A, 2011. **108**(45): p. 18227-32.

31. Toga, K.B., et al., *A drop on a floating sheet: boundary conditions, topography and formation of wrinkles.* Soft Matter, 2013.

32. Schroll, R.D., et al., *Capillary Deformations of Bendable Films.* Physical Review Letters, 2013. **111**(1).

33. Timoshenko, S.P. and J.N. Goodier, *Theory of Elasticity*. Vol. 1. 1961, New York: McGraw Hill.

34. Geminard, J.C., R. Bernal, and F. Melo, *Wrinkle formations in axi-symmetrically stretched membranes.* Eur Phys J E Soft Matter, 2004. **15**(2): p. 117-26.

35. Cerda, E., *Mechanics of scars.* J Biomech, 2005. **38**(8): p. 1598-603.

36. Timoshenko, S.P. and J.M. Gere, *Theory of Elastic Stability*. Vol. 2. 1989, New York: Dover.

37. Sukanek, P.C., *Dependence of Film Thickness on Speed in Spin Coating.* Journal of The Electrochemical Society, 1991. **138**(6): p. 1712.

38. Hall, D.B., P. Underhill, and J.M. Torkelson, *Spin coating of thin and ultrathin polymer films.* Polymer Engineering & Science, 1998. **38**(12): p. 2039-2045.

39. Reiter, G. and P.G. de Gennes, *Spin-cast, thin, glassy polymer films: Highly metastable forms of matter.* Eur. Phys. J. E, 2001. **6**: p. 25–28.

40. Damman, P., et al., *Relaxation of Residual Stress and Reentanglement of Polymers in Spin-Coated Films.* Physical Review Letters, 2007. **99**(3).

41. Chung, J.Y., et al., *Quantifying residual stress in nanoscale thin polymer films via surface wrinkling.* ACS Nano, 2009. **3**(4): p. 844-52.

42. Ree, M., C.-W. Chu, and M.J. Goldberg, *Influences of chain rigidity, in-plane orientation, and thickness on residual stress of polymer films.* Journal of Applied Physics, 1994. **75**(3): p. 1410.

43. Ree, M., et al., *Effect of film formation process on residual stress of poly(p-phenylene biphenyltetracarboximide) in thin films.* Polymer, 1997. **38**(26): p. 6333-6345.

44. Ree, M., et al., *Residual stress and optical properties of fully rod-like poly(p-phenylene pyromellitimide) in thin films: Effects of soft-bake and thermal*

imidization history. Journal of Polymer Science Part B: Polymer Physics, 1998. **36**(8): p. 1261-1273.

45. Bates, F.S. and G.H. Fredrickson, *Block copolymer thermodynamics: theory and experiment.* Annu Rev Phys Chem, 1990. **41**: p. 525-57.

46. Dobkowski, Z., *Determination of critical molecular weight for entangled macromolecules using the tensile strength data.* Rheologica Acta, 1995. **34**(6): p. 578-585.

47. Campoy-Quiles, M., et al., *Thickness-Dependent Thermal Transition Temperatures in Thin Conjugated Polymer Films.* Macromolecules, 2006. **39**(22): p. 7673-7680.

48. Reiter, G. and S. Napolitano, *Possible origin of thickness-dependent deviations from bulk properties of thin polymer films.* Journal of Polymer Science Part B: Polymer Physics, 2010. **48**(24): p. 2544-2547.

49. Ao, Z. and S. Li, *Temperature- and thickness-dependent elastic moduli of polymer thin films.* Nanoscale Res Lett, 2011. **6**(1): p. 243.

50. Reiter, G., *Mobility of Polymers in Films Thinner than Their Unperturbed Size.* Europhysics Letters (EPL), 1993. **23**(8): p. 579-584.

51. Keddie, J.L., R.A.L. Jones, and R.A. Cory, *Size-Dependent Depression of the Glass Transition Temperature in Polymer Films.* Europhysics Letters (EPL), 1994. **27**(1): p. 59-64.

52. Forrest, J., et al., *Effect of Free Surfaces on the Glass Transition Temperature of Thin Polymer Films.* Physical Review Letters, 1996. **77**(10): p. 2002-2005.

53. Forrest, J., K. Dalnoki-Veress, and J. Dutcher, *Interface and chain confinement effects on the glass transition temperature of thin polymer films.* Physical Review E, 1997. **56**(5): p. 5705-5716.

54. Timoshenko, S.P. and W.-K. S., *Theory of Plates and Shells*, 1959, McGraw-Hill: New York.

55. Alaca, B.E., et al., *Biaxial testing of nanoscale films on compliant substrates: Fatigue and fracture.* Review of Scientific Instruments, 2002. **73**(8): p. 2963.

56. Russell, T.P., *Neutron reflection*, in *Encyclopedia of Materials Characterization*, L.E. Fitzpatrick, Editor. 1992, Manning Publication Company: Greenwich, CT. p. 660-670.

57. Gaines, G.L., *Insoluble monolayers at liquid-gas interfaces*. 1966: Interscience Publishers.

58. de Groot, P. and L. Deck, *Three-dimensional imaging by sub-Nyquist sampling of white-light interferograms.* Optics Letters, 1993. **18**(17): p. 1462.

59. de Groot, P. and L. Deck, *Surface Profiling by Analysis of White-light Interferograms in the Spatial Frequency Domain.* Journal of Modern Optics, 1995. **42**(2): p. 389-401.

60. Vella, D., M. Adda-Bedia, and E. Cerda, *Capillary wrinkling of elastic membranes.* Soft Matter, 2010. **6**(22): p. 5778.

61. Mansfield, E.H., *The bending and stretching of plates*. 1964: Pergamon Press.

62. Davidovitch, B., R.D. Schroll, and E. Cerda, *Nonperturbative model for wrinkling in highly bendable sheets*. Physical Review E, 2012. **85**(6).

63. Jerison, E.R., et al., *Deformation of an Elastic Substrate by a Three-Phase Contact Line.* Physical Review Letters, 2011. **106**(18).

64. Style, R.W. and E.R. Dufresne, *Static wetting on deformable substrates, from liquids to soft solids.* Soft Matter, 2012. **8**(27): p. 7177.

65. Style, R.W., et al., *Universal Deformation of Soft Substrates Near a Contact Line and the Direct Measurement of Solid Surface Stresses.* Physical Review Letters, 2013. **110**(6).

66. Nadermann, N., C.Y. Hui, and A. Jagota, *Solid surface tension measured by a liquid drop under a solid film.* Proc Natl Acad Sci U S A, 2013. **110**(26): p. 10541-5.

67. Vandeparre, H., et al., *Wrinkling Hierarchy in Constrained Thin Sheets from Suspended Graphene to Curtains.* Physical Review Letters, 2011. **106**(22).

68. Davidovitch, B., *Period fissioning and other instabilities of stressed elastic membranes.* Physical Review E, 2009. **80**(2).

69. A., A.C., et al., *Relaxation in glassforming liquids and amorphous solids.* Journal of Applied Physics, 2000. **88**: p. 3113–3157.

70. Alcoutlabi, M. and G.B. McKenna, *Effects of confinement on material behaviour at the nanometre size scale.* Journal of Physics-Condensed Matter, 2005. **17**(15): p. R461-R524.

71. Jackson, C.L. and G.B. McKenna, *THE GLASS-TRANSITION OF ORGANIC LIQUIDS CONFINED TO SMALL PORES.* Journal of Non-Crystalline Solids, 1991. **131**: p. 221-224.

72. Damman, P., et al., *Relaxation of residual stress and reentanglement of polymers in spin-coated films.* Physical Review Letters, 2007. **99**(3).

73. Sharp, J.S. and J.A. Forrest, *Free surfaces cause reductions in the glass transition temperature of thin polystyrene films.* Physical Review Letters, 2003. **91**(23).

74. Liu, Y., et al., *Surface relaxations in polymers.* Macromolecules, 1997. **30**(25): p. 7768-7771.

75. Tsui, O.K.C., T.P. Russell, and C.J. Hawker, *Effect of interfacial interactions on the glass transition of polymer thin films.* Macromolecules, 2001. **34**(16): p. 5535-5539.

76. Priestley, R.D., et al., *Structural relaxation of polymer glasses at surfaces, interfaces and in between.* Science, 2005. **309**(5733): p. 456-459.

77. Lu, H.Y., W. Chen, and T.P. Russell, *Relaxation of Thin Films of Polystyrene Floating on Ionic Liquid Surface.* Macromolecules, 2009. **42**(22): p. 9111-9117.

78. Bodiguel, H. and C. Fretigny, *Viscoelastic dewetting of a polymer film on a liquid substrate.* European Physical Journal E, 2006. **19**(2): p. 185-193.

79. Bodiguel, H. and C. Fretigny, *Reduced viscosity in thin polymer films.* Physical Review Letters, 2006. **97**(26).

80. Wang, J.H. and G.B. McKenna, *Viscoelastic and Glass Transition Properties of Ultrathin Polystyrene Films by Dewetting from Liquid Glycerol.* Macromolecules, 2013. **46**(6): p. 2485-2495.

81. O'Connell, P.A. and G.B. McKenna, *Rheological measurements of the thermoviscoelastic response of ultrathin polymer films.* Science, 2005. **307**(5716): p. 1760-1763.

82. O'Connell, P.A., S.A. Hutcheson, and G.B. McKenna, *Creep behavior of ultra-thin polymer films.* Journal of Polymer Science Part B-Polymer Physics, 2008. **46**(18): p. 1952-1965.

83. Reiter, G., *DEWETTING AS A PROBE OF POLYMER MOBILITY IN THIN-FILMS.* Macromolecules, 1994. **27**(11): p. 3046-3052.

84. Masson, J.L. and P.F. Green, *Viscosity of entangled polystyrene thin film melts: Film thickness dependence.* Physical Review E, 2002. **65**(3).

85. A., O.C.P. and M.G. B., *Novel nanobubble inflation method for determining the viscoelastic properties of ultrathin polymer films.* Review of Scientific Instruments, 2007. **78**: p. 013901.

86. A., O.C.P. and M.G. B., *A novel nano-bubble inflation method for determining the viscoelastic properties of ultrathin polymer films.* The Journal of Scanning Microscopies, 2008. **30**(2): p. 184–196.

87. Cardona, M., R.V. Chamberlin, and W. Marx, *The history of the stretched exponential function.* Annalen Der Physik, 2007. **16**(12): p. 842-845.

88. Berberan-Santos, M., E.N. Bodunov, and B. Valeur, *History of the Kohlrausch (stretched exponential) function: Pioneering work in luminescence.* Annalen Der Physik, 2008. **17**(7): p. 460-461.

89. Gao, L.C. and T.J. McCarthy, *Ionic liquids are useful contact angle probe fluids.* Journal of the American Chemical Society, 2007. **129**(13): p. 3804-+.

90. Tien, P.K., R. Ulrich, and R.J. Martin, *MODES OF PROPAGATING LIGHT WAVES IN THIN DEPOSITED SEMICONDUCTOR FILMS.* Applied Physics Letters, 1969. **14**(9): p. 291-&.

91. Prest, W.M. and D.J. Luca, *ORIGIN OF THE OPTICAL ANISOTROPY OF SOLVENT CAST POLYMERIC FILMS.* Journal of Applied Physics, 1979. **50**(10): p. 6067-6071.

92. Prest, W.M. and D.J. Luca, *ALIGNMENT OF POLYMERS DURING THE SOLVENT COATING PROCESS.* Abstracts of Papers of the American Chemical Society, 1980. **179**(MAR): p. 45-ORPL.

93. Prest, W.M., *MOLECULAR-ORIENTATION IN SOLVENT-CAST POLYMERIC FILMS.* Journal of Coatings Technology, 1981. **53**(680): p. 30-30.

94. Chow, T.S. and W.M. Prest, *STRUCTURAL RECOVERY OF QUENCHED AND ANNEALED GLASSES.* Journal of Applied Physics, 1982. **53**(10): p. 6568-6573.

95. Hill, R., *A theory of the plastic bulging of a metal diaphragm by lateral pressure* Philosophical Magazine, 1950. **41**: p. 1133-1142.

96. Beams, J.W., ed. *Mechanical Properties of Thin Films of Gold and Silver*. Structure and Properties of Thin Films Proceedings, ed. C.A. Neugebauer. 1959, Wiley: New York. 183-192.

97. D., J.D., P.G. W., and D.C. D., *A Bubble Inflation Technique for the Measurement of Viscoelastic Properties in Equal Biaxial Extensional Flow.* Transactions of The Society of Rheology, 1972. **16**(3): p. 421–445.

98. Tsakalakos, T., *THE BULGE TEST - A COMPARISON OF THEORY AND EXPERIMENT FOR ISOTROPIC AND ANISOTROPIC FILMS.* Thin Solid Films, 1981. **75**(3): p. 293-305.

99. Small, M.K. and W.D. Nix, *ANALYSIS OF THE ACCURACY OF THE BULGE TEST IN DETERMINING THE MECHANICAL-PROPERTIES OF THIN-FILMS.* Journal of Materials Research, 1992. **7**(6): p. 1553-1563.